UNIVERSITÀ DEGLI STUDI DI PAVIA

DIPARTIMENTO DI FISICA

Master in Physical Sciences

Experimental and computational optical-fiber based dosimetry for neutron and photon non-conventional radiotherapy

MSc thesis by:
Letizia Breccia

Supervisor:
Prof. Silva Bortolussi
Co-supervisors:
Prof. Matteo Ferrari
Dr. Ian Postuma

A.Y. 2024-2025

Abstract

Una dosimetria accurata è un requisito fondamentale nelle tecniche di radioterapia non convenzionali, come la Boron Neutron Capture Therapy (BNCT) e la FLASH radiotherapy, in cui la presenza di campi misti neutroni–fotoni o le dosi ultra-elevate mettono alla prova le prestazioni dei rivelatori convenzionali. In questo contesto, le fibre ottiche a base di silice sono emerse come candidati promettenti per una dosimetria in tempo reale e minimamente invasiva.

La presente tesi combina approcci computazionali e sperimentali per valutare la fattibilità delle fibre ottiche come dosimetri in tali condizioni. Sono state utilizzate simulazioni Monte Carlo con il codice PHITS per riprodurre le condizioni di irraggiamento della colonna termica del reattore TRIGA Mark II, fornendo una caratterizzazione dettagliata delle componenti di dose da neutroni e fotoni e prevedendo la risposta della fibra alla scala micrometrica. Ciò ha permesso una caratterizzazione dettagliata delle componenti di dose neutroniche e fotoniche attese in silice.

Nell'impianto PETRA del Laboratorio Hubert Curien a Saint-Étienne, sono stati effettuati esperimenti in condizioni controllate. Qui, sono state performate misure di Radiation-Induced Luminescence (RIL) con fibre ottiche dopate con cerio (Ce-doped) e su fibre con una media concentrazione di gruppi ossidrilici (M-OH). Le prime hanno mostrato un'elevata sensibilità intrinseca, mentre le seconde una risposta lineare caratterizzata da un afterglow trascurabile e una sensibilità modulabile con la lunghezza della fibra. Invece, lo studio della Radiation Induced Attenuation (RIA) è stato investigato con fibre dopate con il fosforo (P-doped) usando tecniche OTDR, dimostrando l'attesa risposta lineare della dose fino a parecchi Gy, con buona ripetibilità e risoluzione spaziale adatta per dosimetria distribuita. Questi risultati confermano l'idoneità di entrambe le tecniche per l'applicazione nel campo misto della colonna termica del reattore TRIGA.

Inoltre, lo studio è stato esteso alla FLASH radiotherapy. Effettuando test pulsati dedicati, è stato possibile mostrare che fibre M-OH combinano una dinamica di recupero rapida con una risposta lineare del segnale, permettendo un monitoraggio impulso per impulso senza sovrapposizioni, mentre le fibre Ce-doped sono limitate da un persistente afterglow. Questi risultati identificano le fibre M-OH come solidi candidati per dosimetria in tempo reale e in condizioni di ultra-high dose-rate.

Nel complesso, questa tesi evidenzia il potenziale delle fibre ottiche a base di silice come dosimetri versatili, a partire da applicazioni di BNCT fino alla FLASH. I risultati delle simulazioni, gli esperimenti e i calcoli confermano la fattibilità dell'implementazione di dosimetri a fibre ottiche nella colonna termica del reattore TRIGA.

Parte dei risultati sperimentali sono stati presentati alla *conferenza SiO_2 2025* (Saint-Étienne) e sono inclusi in un articolo in pubblicazione, a conferma dell'originalità e della rilevanza del lavoro svolto.

Abstract

Accurate dosimetry represents a fundamental prerequisite for non-conventional radiotherapy modalities such as Boron Neutron Capture Therapy (BNCT) and FLASH radiotherapy, where the presence of mixed neutron–photon fields or ultra-high dose rates challenges the performance of conventional detectors. In this framework, silica-based optical fibers have emerged as promising candidates for real-time and non-invasive dosimetry.

This thesis combines computational and experimental approaches to evaluate the feasibility of employing optical fibers as dosimeters in the aforementioned contexts. Monte Carlo simulations were performed using the PHITS code to reproduce the radiation field conditions inside the thermal column of the TRIGA Mark II reactor in Pavia. This allowed a detailed characterization of the neutron and photon dose components expected in silica.

Experiments under controlled irradiation conditions were carried out at the PETRA facility of the Hubert Curien Laboratory in Saint-Étienne. Here, Radiation-Induced Luminescence (RIL) measurements were performed on optical fibers doped with cerium (Ce-doped) and on fibers with a medium hydroxyl concentration (M–OH). The former exhibited high intrinsic sensitivity, whereas the latter showed a linear response with negligible afterglow and a sensitivity tunable with fiber length. Radiation-Induced Attenuation (RIA) was investigated in phosphorus doped (P-doped) fibers using OTDR techniques, demonstrating the expected linear dose–response up to several hundred Gy, with good repeatability and spatial resolution suitable for distributed dosimetry. These results confirm the suitability of both techniques for application within the mixed field of the TRIGA reactor thermal column.

Furthermore, the study was extended to FLASH radiotherapy. Dedicated pulsed tests showed that M–OH fibers combine fast recovery dynamics with linear signal response, allowing pulse-by-pulse monitoring without overlap, whereas Ce-doped fibers are limited by persistent afterglow. These findings identify M–OH fibers as solid candidates for real-time dosimetry under ultra-high dose-rate conditions.

Overall, this thesis highlights the potential of silica optical fibers as versatile dosimeters, from BNCT to FLASH applications. The results derived from the simulations, the experiments and calculations confirm the feasibility of implementing fiber-based dosimetry in the thermal column of the TRIGA reactor.

Part of the experimental results were presented at the *SiO_2 Conference 2025* in Saint-Étienne and are included in a forthcoming publication, underscoring the originality and impact of this work.

Contents

Introduction

Radiotherapy plays a central role in the treatment of many cancers, but its effectiveness is often limited by the need to preserve surrounding healthy tissues. Among the alternative strategies under investigation, Boron Neutron Capture Therapy (BNCT) exploits the nuclear reaction $^{10}\mathrm{B}(n,\alpha)^{7}\mathrm{Li}$ to achieve a highly localized energy deposition at the cellular scale. The products of this reaction have a short range (5-9 μm) and a high Linear Energy Transfer (LET), enabling the selective destruction of boron-loaded tumor cells while largely sparing adjacent healthy ones. The selectivity of BNCT therefore relies both on the physics of the reaction and on the ability of boron compounds to preferentially accumulate in malignant tissues. Over the last decades, BNCT has been investigated in several clinical trials, initially with neutron beams extracted from research reactors and, more recently, with accelerator-based neutron sources that are fostering a renewed worldwide interest in this therapy.

As in all radiotherapy modalities, accurate dosimetry is essential to ensure both the safety and the effectiveness of BNCT. In this case, however, the mixed neutron-photon field generated makes the calculation of absorbed dose particularly complex, since it combines radiation components with different LET and biological effectiveness. This motivates the continuous development of new computational tools and experimental detectors.

Within this framework, the TRIGA Mark II reactor of the University of Pavia provides a unique experimental facility to conduct BNCT tests and radiobiological studies. This facility represents the reference environment for the work presented in this thesis.

In recent years, silica-based optical fibers have emerged as promising candidates for real-time dosimetry in such mixed radiation fields. Their response relies on two different mechanisms: Radiation-Induced Luminescence (RIL), which can be correlated to dose rate, and Radiation-Induced Attenuation (RIA), which provides information on the accumulated dose.

A highly specialized research group in the investigation of optical fiber is the Materials for Optics and Photonics in Extreme Radiation Environments (MOPERE) of Hubert Curien Laboratory. From a collaboration established between this group and the Physics Department of the University of Pavia, a project was developed to investigate the feasibility of employment of optical fibers for dosimetric purposes in the BNCT framework.

This master thesis has been conceived in this context. The ERASMUS+ Traineeship Exchange

Program allowed me to complete an internship of three months at MOPERE group in Saint-Etienne, France. The experiments described in this work were carried out at the PETRA irradiation facility, using radiaiton testing equipment.

The present thesis combines both computational and experimental approaches. Monte Carlo simulations were performed with the PHITS code to reproduce the irradiation conditions of the TRIGA thermal column in Pavia, providing reference spectra and dose distributions to guide the detector development. Complementary to these studies, experimental campaigns (RIL and RIA) were carried out to characterize the response of different fiber types under controlled irradiations at the mentioned facility. Together, these investigations provide the basis for assessing the feasibility of optical fibers as dosimeters in the TRIGA reactor thermal column for BNCT applications.

In parallel with BNCT, another field of growing interest in radiation oncology is ultra-high dose rate irradiation, known as FLASH radiotherapy. This approach is based on the observation that when ionizing radiation is delivered at dose rates above $\sim$40 Gy/s, normal tissues exhibit a reduced level of toxicity while the anti-tumor effectiveness is preserved. This so-called *FLASH effect* has been reported in several pre-clinical studies and is currently the subject of intense investigation, with the aim of extending its applicability to clinical treatments. However, the translation of FLASH radiotherapy into routine practice is strongly limited by the lack of dosimetric systems capable of providing accurate, real-time measurements under such extreme conditions of dose rate.

Optical fibers represent a promising solution also in this context. Their fast response, small size and radiation hardness make them suitable candidates for monitoring pulsed and continuous high-intensity irradiations. In particular, time-resolved RIL measurements allow capturing the transient light emission induced by the radiation pulse, while RIA can be used to monitor cumulative effects at high doses. The possibility of employing the same sensing technology both in mixed neutron–photon fields (as in BNCT) and in ultra-high dose rate photon or electron beams (as in FLASH) highlights the versatility of optical fiber dosimetry and motivates its investigation across these different but complementary research domains.

The manuscript is organized as follows. Chapter 1 introduces the fundamental concepts of radiation interactions, dosimetric quantities, and optical fiber dosimetry, together with an overview of BNCT. Chapter 2 focuses on the TRIGA Mark II reactor and its thermal column, presenting previous characterization studies, feasibility considerations and dedicated Monte Carlo simulations with the PHITS code. Chapter 3 is devoted to photon irradiation experiments at the PETRA facility, where both RIL- and RIA-based techniques were investigated under continuous conditions to benchmark fiber performance, and then extended to FLASH radiotherapy with dedicated pulsed tests. Chapter 4 analyses from a quantitative point of view the feasibility of using optical fiber as dosimeters in the thermal column of the TRIGA reactor. Finally, the Conclusions summarize the main results and outline perspectives for future developments.

Chapter 1

Background Knowledge

1.1 Radiation Interaction and Dosimetric Quantities

Particles interact primarily through four fundamental forces: the strong interaction, the electromagnetic interaction, the weak interaction and the gravitational interaction. The strong interaction is responsible for binding protons and neutrons within the atomic nucleus. The electromagnetic interaction governs the forces between electrically charged particles. The weak interaction enables the transformation of one type of subatomic particle into another, playing a central role in many processes, such as radioactive decay. Gravitation, although negligible at the subatomic scale, acts on all particles with mass.

In the context of radiation, electromagnetic interaction is particularly relevant, as it mediates the exchange of photons. Radiation can be defined as the emission or transmission of energy through space or a medium, occurring either in the form of electromagnetic or particle radiation. Electromagnetic radiation consists of propagating waves, in which the electric and magnetic field vectors oscillate perpendicularly to each other and to the direction of propagation. An electromagnetic wave is characterized by its wavelength λ and frequency ν, related to the propagation speed v of light in the medium by the general relation:

$$\nu = \frac{v}{\lambda} \tag{1.1}$$

Since the velocity is given by $v = c/n$, with c the light speed and n the refractive index of the medium, we obtain:

$$\nu = \frac{c}{n\lambda}. \tag{1.2}$$

In the special case of vacuum ($n = 1$), this reduces to the simpler expression $\nu = c/\lambda$.

Electromagnetic radiation is classified as ionizing when its energy is sufficient to remove electrons from atoms and molecules, thus producing ions. In such cases, its interaction with matter is

more accurately described by considering the wave as a stream of discrete particles, the photons. Each of them carries an energy equal to $E = h\nu$, where h is the Planck constant. For hydrogen, the energy necessary for the ionization is around 14 eV. Electromagnetic radiation is conventionally considered ionizing when the photon energy exceeds the ionization potential of atoms and molecules. Since typical ionization energies for biological matter are on the order of 10 to 15 eV, radiation with photon energies above about 10 eV is generally classified as ionizing [1][2]. In practice, this corresponds to the high-energy part of the electromagnetic spectrum, namely X-rays and γ-rays.

It is possible to classify ionizing radiation into directly ionizing and indirectly ionizing. The first one consists in charged particles, such as electrons, protons, positrons, α particles, etc., which deliver their energy to matter directly, through many small Coulomb interactions between the ionizing particles and the orbital electrons of the crossed medium along the particle track. Indirectly ionizing radiation consists in neutral particles such as photons (X-rays or γ-rays) or neutrons, which first transfer their energy to charged particles in the matter. Neutrons interact with nuclei producing charged particles, which in turn deliver the energy to matter as described above. Photons interacting with matter predominantly transfer their energy to electrons, through processes such as the photoelectric effect, Compton scattering, and pair production. The resulting secondary electrons then lose energy via Coulomb interactions with atomic electrons in the medium. At higher photon energies, however, additional processes such as photonuclear reactions may also occur, leading to the emission of nucleons or other nuclear fragments.

When a beam of particles, directly or indirectly ionizing, traverses a layer of matter, it interacts with the material, via processes such as scattering, diffusion, absorption, etc. This leads to an output flux whose attenuation depends on the specific occurring physical processes. These phenomena are characterized by a stochastic nature so their occurrence can be described by probability distribution functions and average or expectation values. One of the most important parameters used in this way is the cross section, defined as:

$$\sigma = \frac{AttenuatedFlux}{IncidentFluxperUnitArea} \tag{1.3}$$

It represents the effective area of the target projected perpendicularly to the direction of the incident flux that can interact with the incoming particles. It is usually expressed in barns, where 1 barn corresponds to 10^{-28} m^2.

These considerations naturally lead to the concept of dosimetry. Although so far the discussion has focused on the physical description of radiation and its interaction with matter, dosimetry deals with quantifying the interactions in terms of the energy deposited in a medium. In essence, it provides the link between the microscopic and stochastic scattering, absorption and ionization mechanisms, and the macroscopic non-stochastic quantities that can be estimated and in many cases correlated to the radiation effects. For this reason, dosimetry plays a fundamental role in areas such as medical diagnostics and therapy, radiation protection, monitoring of radiation environments, and the study radiation effects in electronics and materials. In the next sections, the interaction of ionizing radiation with matter is briefly described. In Section 1.1.4, the main dosimetric quantities and their definitions are introduced.

1.1.1 Interaction of Photons with Matter

Photoelectric Effect

The photoelectric effect is the result of the absorption of an incoming photon, with energy equal to or higher than the binding energy of an electron, which is later released. Part of the energy of the incoming photon is used to release the electron and it corresponds to the electron binding energy, that depends on the specific atomic shell. The remaining energy is converted into kinetic energy carried away by the emitted electron. Figure 1.1 shows a sketch of the photoelectric emission. Here E_b denotes the electron binding energy, T is the kinetic energy of the emitted photoelectron, and T_A is the recoil kinetic energy of the atom, which is usually negligible compared to the other terms.

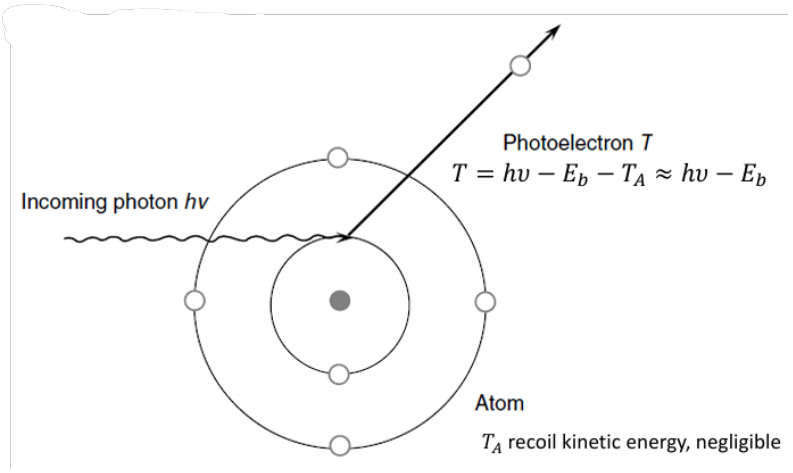

Figure 1.1: Scheme illustrating the photoelectric effect mechanism [3].

The cross section for the photoelectric effect can be calculated as:

$$\sigma_{PE_a} = \frac{kZ^n}{(h\nu)^m} \tag{1.4}$$

where k is a constant, n is equal to 4 and m to 3 for $h\nu$ = 0.1 MeV, n gradually increases up to 4.6 for $h\nu$ = 3 MeV, whereas m drops to 5 at 5 MeV. Accordingly, this phenomenon is more relevant at low photon energies, and for high atomic numbers. In addition, the cross section shows discontinuities at energies corresponding to the binding energies of the electrons in the atomic shells, known as absorption edges (levels). At energies just above the edge, the photon has enough energy to eject the electron, so the cross section abruptly increases due to the larger number of electrons that can take part in the absorption process.

After the electron emission, the vacancy left in the atomic shell can be filled by another electron coming from an outer shell. The exceeding energy is carried away through the emission of a photon or an electron. The former is called characteristic X-ray, because it is characterized by an energy equal to the energy gap between levels, and so it represents a specific signature of

the atomic species. The latter is referred to as Auger electron. Characteristic X-rays and Auger electrons are isotropically emitted.

Compton Scattering

If the energy of the incident wave is high enough and is larger than the binding energy of a weakly bound electron, an inelastic scattering, called *Compton effect*, can occur. In this case, only part of the photon energy is transferred to the recoil electron, that escapes leaving the atom ionized and keeping a certain kinetic energy. The photon is scattered with lower energy and a different direction (Figure 1.2). The kinematics of the reaction is obtained by conservation of energy and momentum as in a two-particle scattering.

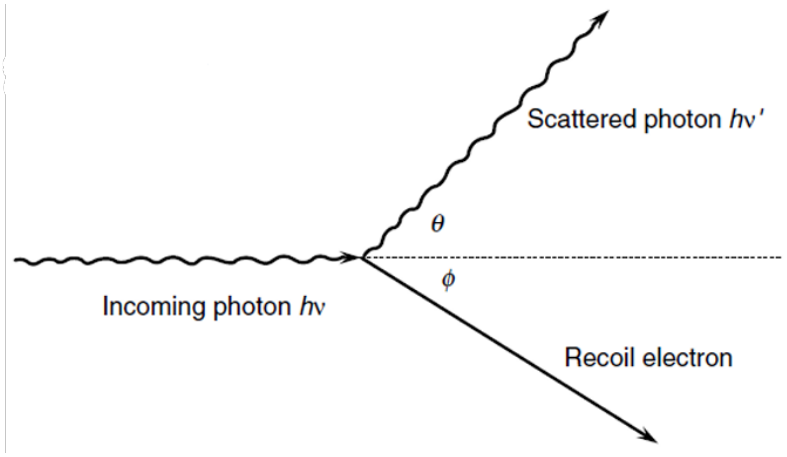

Figure 1.2: Scheme illustrating the Compton scattering mechanism [3].

The cross section of this process is obtained from Klein-Nishina differential formula integration over a solid angle $d\Omega$:

$$\sigma_{KN_e} = 2\pi {r_e}^2 \left[\frac{1+\alpha}{\alpha^2} \left(\frac{2(1+\alpha)}{1+2\alpha} - \frac{ln(1+2\alpha)}{\alpha} \right) + \frac{ln(1+2\alpha)}{2\alpha} - \frac{1+3\alpha}{(1+2\alpha)^2} \right] \tag{1.5}$$

Where r_e is the electron radius and α is defined as:

$$\alpha = \frac{h\nu}{m_e c^2} \tag{1.6}$$

Being m_e the electron mass.

Pair Production

The pair production phenomenon can happen when an incident photon interacts with the Coulomb field of an atom nucleus. It is totally absorbed with the production of an electron-positron pair;

the sum of their kinetic energies is determined by energy conservation (Figure 1.3). This process has an energy threshold E = 1.022 MeV (= $2m_ec^2$). The pair production cross section rises rapidly above the threshold energy of 1.022 MeV and, in first approximation, is proportional to Z^2 and increases logarithmically with the photon energy:

$$\sigma_{pp} \propto Z^2 \ln(E_\gamma). \tag{1.7}$$

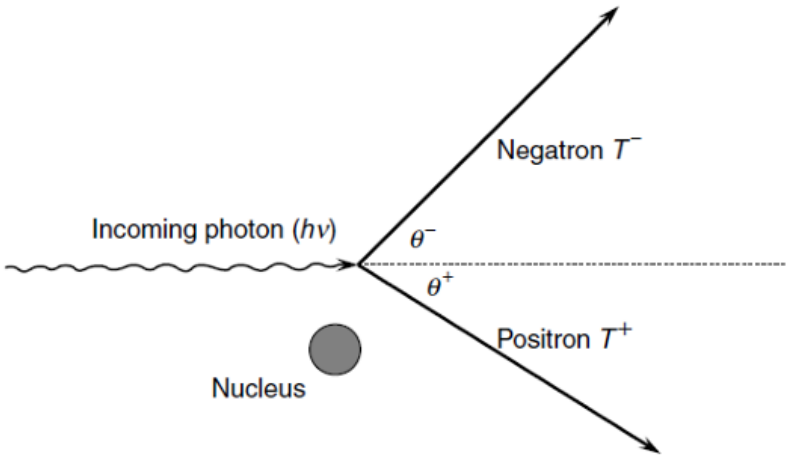

Figure 1.3: Schematic representation of pair production in the field of a nucleus. The incident photon produces an electron-positron pair with kinetic energies T^- and T^+ and emission angles θ^- and θ^+, respectively. Here the electron is labeled as "*negatron*" (e^-) to explicitly distinguish it from the positron (e^+) [3].

Figure 1.4 summarizes the relative importance of the main photon–matter interaction processes as a function of photon energy and atomic number Z. At low photon energies and for high-Z materials, the photoelectric effect dominates, reflecting the strong Z dependence of its cross section. At intermediate energies, the Compton effect becomes the prevails, with a weaker dependence on Z. Finally, at photon energies above a few MeV and for sufficiently high Z, pair production becomes the dominant process, as its cross section grows approximately proportionally to Z^2 and increases with photon energy.

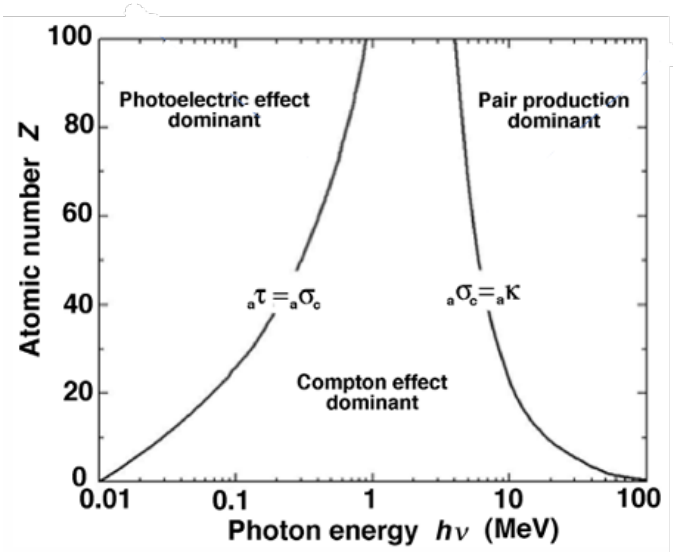

Figure 1.4: Probability of the three main photon-matter interaction processes in the phase-space of the atomic number Z and the incident photon energy $h\nu$ [1].

Coherent Rayleigh Scattering

Rayleigh scattering is an interaction between a photon and the whole atom. It is called coherent because the photon is scattered by the constructive action of the tightly bound electrons of the whole atom. The photon maintains its initial energy, but is redirected through a small scattering angle. Being that there is no energy transfer to charged particles, this process does not play a significant role in radiation dosimetry.

Photonuclear Interaction

Photonuclear interaction is a direct interaction between an energetic photon and an absorber nucleus. The latter absorbs the former, most likely resulting in the emission of a single neutron (referred to as *photoneutron*) through a (γ, n) reaction. This process does not play a major role in photon attenuation due to its low cross section, however it is important in shielding calculations when photon energies exceed the photonuclear reaction threshold. In fact, the daughter nuclei from the reaction may be radioactive and the produced neutron may undergo subsequent neutron capture, producing radioactivity in the irradiation facility. Moreover, the neutrons thus produced are ionizing radiation themselves, and may be a source of dose absorbed in biological tissues of individuals in the proximity of the photon source. For all the interaction processes described, the secondary particles produced represent ionizing radiation themselves and therefore require proper consideration in terms of dosimetry and radiation protection. This aspect is particularly critical in the case of neutrons, which pose specific challenges due to their high penetration and indirect ionization mechanisms. Such issues become especially relevant in applications such as clinical high-energy linear accelerators for radiotherapy.

1.1.2 Interaction of Charged Particles with Matter

Heavy charged particles, such as protons and high Z ions, are capable of ionizing matter. This process is predominantly governed by the Coulomb interaction, as it involves interaction between charged particles. In a collision between a heavy particle and a light particle at rest, for example an electron, the fraction of kinetic energy transferred is negligible. Consequently, heavy particles tend to maintain their trajectories with minimal deflection after individual collisions. Although the energy loss per interaction is small, the cumulative effect over many collisions (that can be of the order of 10^4 for particles of MeV energy range) can become substantial. Figure 1.5 illustrates a simplified comparison between two types of particles traversing matter. The key difference lies in their mass: α particles, being much heavier than the target electrons, undergo only small trajectory deviations and lose only a small fraction of their energy in each individual collision. However, the cumulative energy loss over many interactions is substantial and ultimately limits their penetration range in matter.

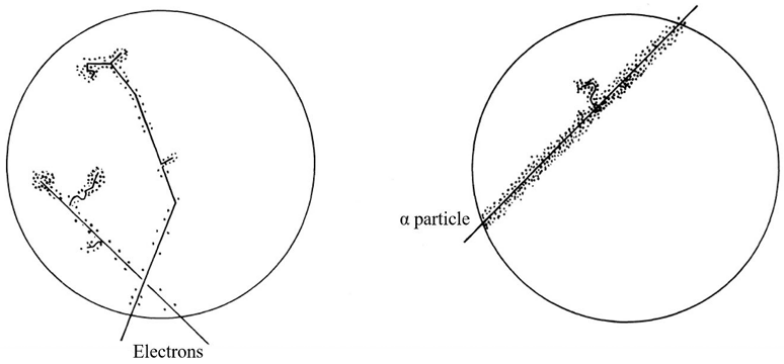

Figure 1.5: Trajectory of two electrons on the left and of an α particle on the right in a medium. The dots represent the ionizations caused by the particles [4].

The mean energy loss per unit path length for a charged particle traversing a medium can be derived from the Bethe–Bloch equation. Considering quantum and relativistic effects, the stopping power for a particle of charge ze and velocity v passing through a medium of atomic number Z and electron density N is given by:

$$\left\langle -\frac{dE}{dx} \right\rangle = \frac{z^2 e^4 N}{4\pi\varepsilon_0^2 m_e v^2} \left[\ln\left(\frac{2\gamma^2 m_e v^2}{\langle I \rangle} \right) - \frac{v^2}{c^2} \right] \tag{1.8}$$

where γ is the Lorentz factor and $\langle I \rangle$ is the average excitation potential of the target material. The linear stopping power depends on particle charge and velocity, as well as on the atomic number, electron density, and ionization potential of the medium, but not on the particle mass. Dividing by the material density ρ yields the mass stopping power $-\frac{1}{\rho}\frac{dE}{dx}$, which allows comparison across different materials independent of their density. Since it scales with the ratio Z/A (number of electrons per unit mass), the mass stopping power is larger for materials composed of lighter elements, such as hydrogen rich substances, than for high Z materials.

For protons and in general for charged particles heavier than electrons, the energy loss profile changes with penetration depth, reaching a maximum at a specific range, described by the Bragg curve. This property is particularly relevant in medical applications, enabling precise tumor irradiation, while sparing surrounding healthy tissues [5].

An important related quantity is the Linear Energy Transfer (LET), which represents the energy deposited per unit path length, as derived from the Bethe–Bloch equation previously mentioned. LET describes the energy transferred by the incident particle to the material through interactions between the incident particle and the electrons of the medium. The term *linear* refers to the approximately straight track of heavy charged particles in the medium. The maximum LET value corresponds to the Bragg peak, which is associated to the depth at which the highest energy deposition occur.

Electrons and positrons, being significantly lighter than protons, can reach relativistic speeds at much lower energies, where relativistic effects become dominant. For electrons and positrons, the Bethe–Bloch equation requires specific corrections, as their mass equals that of the target electrons. This symmetry enhances large-angle scattering and modifies the stopping power with additional terms compared to heavy charged particles.

Charged-particle slowing down is more pronounced in materials with higher proton density. At sub-MeV energies, electrons lose energy mainly through collisional processes such as ionization and excitation, gradually slowing down until they are absorbed. In general, the energy loss of electrons can be divided into two contributions: collisional losses, due to interactions with atomic electrons, and radiative losses, due to photon emission. While collisional losses dominate at low energies, above about 1 MeV radiative losses become increasingly important, particularly in high Z materials. Two main mechanisms are distinguished:

- Bremsstrahlung: a charged particle is decelerated in the electric field of a nucleus, resulting in photon emission. The probability of this process increases with the energy of the charged particle and with the atomic number of the medium, making it particularly relevant in high Z materials. Bremsstrahlung is therefore significant in accelerator physics and high-energy astrophysics, and it is also deliberately exploited for the generation of X-rays in diagnostic radiology.

- Synchrotron radiation: emitted by relativistic electrons when their trajectory is bent by a magnetic field. This continuous deflection causes the emission of intense photon pulses tangential to the electron path.

For electrons with energies below about 1 MeV, collisional losses by ionization dominate, leading to a gradual reduction of energy during penetration in the target material. At higher energies, Bremsstrahlung losses become increasingly relevant, particularly in high Z materials, and progressively reduce the particle energy. Moreover, due to multiple scattering and significant lateral deflections along their path, electrons do not exhibit a pronounced Bragg peak as it is observed for heavier charged particles. As a result, their dose distribution within matter tends to be more spread out, and does not show any localized maximum at a specific depth.

1.1.3 Interaction of Neutrons with Matter

Neutrons are electrically neutral particles, and therefore do not undergo Coulomb interactions with electrons. They interact only through nuclear forces, which occur less frequently, allowing neutrons to travel relatively long distances in matter before colliding with a nucleus. When such interactions take place, neutrons can be scattered or absorbed, often producing secondary charged particles that subsequently deposit energy in the medium. Neutrons are conventionally classified based on their energy:

- High energy neutrons (E_n > 100 MeV)
- Fast neutrons (100 keV < E_n < 10 MeV)
- Epithermal neutrons (0.1 eV < E_n < 100 keV)
- Thermal neutrons (E_n = 0.025 eV)
- Ultracold neutrons (E_n < meV-μeV)

Neutrons interact by nuclear force. Being neutral, they travel unaffected by electromagnetic fields, this leading to straight a path. Deviations are associated with interaction with a nucleus, followed by scattering into a new direction or absorption. To describe the neutrons interaction through matter, the mean free path length λ is used, which is the average distance a neutron travels in a specific material between interactions:

$$\lambda = \frac{1}{\Sigma} \tag{1.9}$$

where Σ is the macroscopic cross section, defined as $\Sigma = n\sigma$, with n the atomic density of the material and σ the microscopic cross section.

Neutrons reaction can be classified into two categories: scattering and absorption reactions. Figure 1.6 shows a schematic synthesis of the different mechanisms.

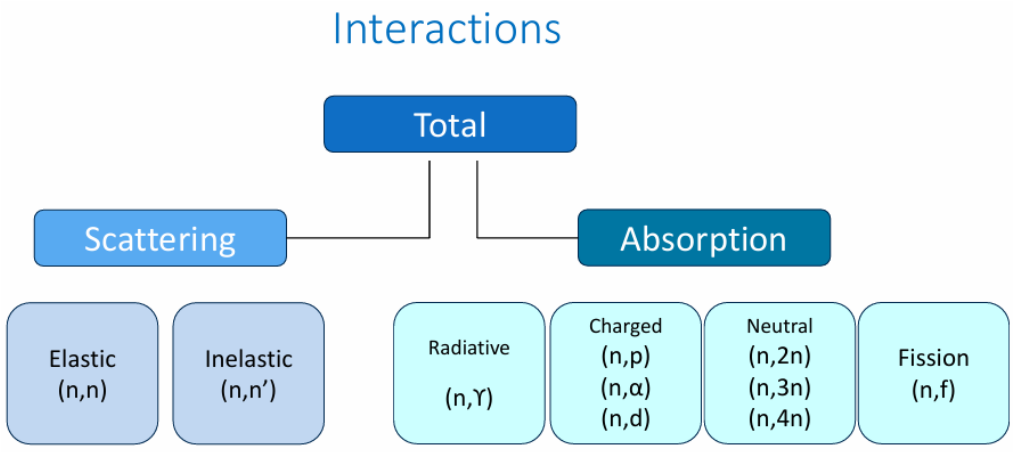

Figure 1.6: Reactions of neutrons with matter. From the left: elastic and inelastic scattering, radiative capture, interaction with charged and neutral products, fission.

It should be noted that neutron interactions with matter can be classified in several different ways, depending on whether the focus is on the final reaction products or on the underlying reaction mechanism. The overview given here does not aim to be exhaustive, but rather to introduce the essential aspects needed to understand the dosimetric context of this thesis.

From a phenomenological point of view (Figure 1.6), neutron interactions are commonly grouped into two broad categories: scattering and absorption. Scattering processes may be elastic (n, n), where the neutron only changes its direction and kinetic energy is conserved, or inelastic (n, n'), where part of the incident energy is transferred to the nucleus, leaving it in an excited state. Absorption processes, on the other hand, include radiative capture (n, γ), charged-particle emission (n, p), (n, α), or (n, d), multiple-neutron emission $(n,2n)$, $(n,3n)$, $(n,4n)$, and fission (n, f).

At a more microscopic level, the same processes can be interpreted in terms of three underlying mechanisms: potential scattering, direct interaction, and compound nucleus formation. Potential scattering is essentially elastic scattering and can occur for neutrons of any energy, being determined by the potential landscape experienced by the neutron near the nucleus. Direct interactions correspond to cases where the neutron, typically at relatively high energy, collides directly with a nucleon in the target nucleus, which can lead to inelastic scattering or particle emission. Finally, compound nucleus formation describes the situation where the incident neutron is absorbed by the nucleus, producing a highly excited intermediate system that subsequently decays by emitting one or more particles or photons. In the center-of-mass frame, the incident neutron and nucleus merge at rest, and the system's kinetic energy is converted into nuclear excitation energy.

1.1.4 Quantities to Describe the Radiation Field

The radiation field is the region of space through which radiation propagates [1]. Radiation interactions are intrinsically stochastic: the occurrence and type of a single interaction cannot be deterministically predicted, but are described in terms of probability distributions and cross sections. Accordingly, the physical variables associated with these processes, such as the number of collisions or the energy imparted in a single event, are stochastic quantities. They can assume different random values within a certain range, discontinuously varying in space and time. In practice, however, it is difficult to work directly with stochastic quantities. For this reason, non-stochastic quantities are introduced, defined as the expectation values of the corresponding stochastic variables. These represent average values that can be predicted by calculation, are continuous in space and time, and provide a practical basis for the description of radiation fields.

For a monoenergetic ionizing radiation beam, valid for photons, electrons, and heavy charged particles, the most commonly used non-stochastic quantities are:

- **Particle Fluence Φ:** is the expectation value of the number of particles dN that enter a small sphere, divided by the cross-sectional area dA of that sphere. Equivalently it can be expressed as the total particle track length dL per unit volume dV.

$$\Phi = \frac{dN}{dA} = \frac{dL}{dV}[m^{-2}] \tag{1.10}$$

- **Fluence Rate ϕ:** is the number of particles crossing the surface per unit time and unit of

area.

$$\phi = \frac{d\Phi}{dt} = \frac{d}{dt}\frac{dN}{dA}[m^{-2}s^{-1}] \tag{1.11}$$

- **Energy Fluence Ψ:** is defined from the expectation value of the total energy transported by N particles R, excluded the energy of the mass at rest.

$$\Psi = \frac{dR}{dA}[Jm^{-2}] \tag{1.12}$$

For monoenergetic beams with energy E, it can be expressed as a function of the particle fluence:

$$\Psi = E \cdot \Phi \tag{1.13}$$

- **Energy Fluence Rate ψ:** is the energy fluence variation over the time interval dt.

$$\psi = \frac{d\Psi}{dt} = \frac{d}{dt}\frac{dR}{dA}[Jm^{-2}s^{-1}] \tag{1.14}$$

In addition to these quantities, to characterize the process of energy release and absorption in matter, dosimetric quantities are defined. These are referred, when possible, to field quantities defined above. For a comprehensive description of dosimetry, it is first necessary to describe the mechanism through which particles deposit their energy inside a material. This is especially true for neutral radiation since it does not ionize matter directly. In this situation, ionization occurs in two steps: the neutral particles first transfer their energy to secondary charged particles, which subsequently deposit their energy in the medium through ionization and excitation processes.

Given a volume V, let us consider:

- $(R_{in})_n$: the energy associated to the particles entering V;
- $(R_{out})_n^{nonrad}$: the energy associated to the neutral particles leaving V, excluding the energy of the photons produced by radiative emission of the charged particles generated in V;
- $(R_{out})_n^{rad}$: the energy associated to the photons produced by radiative emission of the charged particles generated in V.

The machinism concerning this quantities is represented in Figure 1.7. The total energy output can be defined as:

$$(R_{out})_n = (R_{out})_n^{nonrad} + (R_{out})_n^{rad} \tag{1.15}$$

This allows the definition of fundamental quantities for the energy deposition mechanism description: the transferred energy (ϵ_{tr}), the net energy transfer (ϵ_{tr}^n) and the imparted energy (ϵ). The

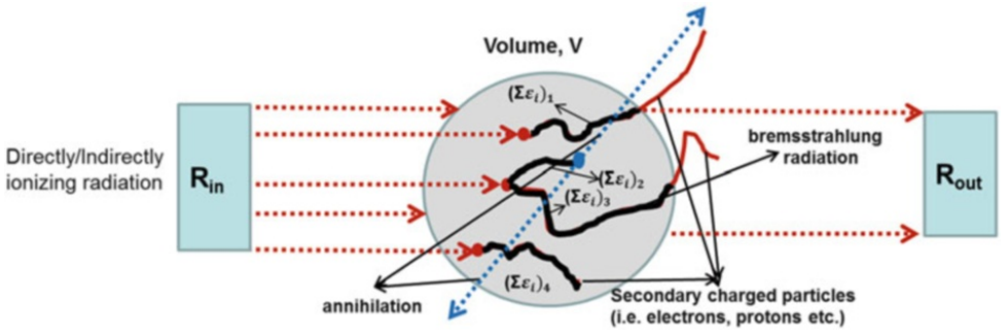

Figure 1.7: Schematic representation of the input and output energies inside an irradiated volume. Acknowledgments to [6].

first one, is the kinetic energy transferred from neutral radiation to the charged particles inside V. It is obtained with:

$$\epsilon_{tr} = (R_{in})_n - (R_{out})_n^{nonrad} + \Sigma Q \tag{1.16}$$

where ΣQ is the energy due to the transformation, occurring in V, of the mass at rest into energy and vice versa, with Q being positive in the first case and negative otherwise.

The net energy transfer is the energy transferred to charged particles minus the energy loss by radiation:

$$\epsilon_{tr}^n = \epsilon_{tr} - (R_{out})_n^{rad} \tag{1.17}$$

The imparted energy is a macroscopic quantity that represents the difference between the energy deposited within V and the energy that escapes V as radiation or particles:

$$\epsilon = (R_{in})_n - (R_{out})_n + (R_{in})_c - (R_{out})_c + \Sigma Q \tag{1.18}$$

where $(R_{in})_n$ and $(R_{in})_c$ are the energies of neutral and charged particles entering in V, $(R_{out})_n$ and $(R_{out})_c$ are the energies leaving V. Fig.1.8 reports the mechanisms through which these quantities interact with the volume of interest.

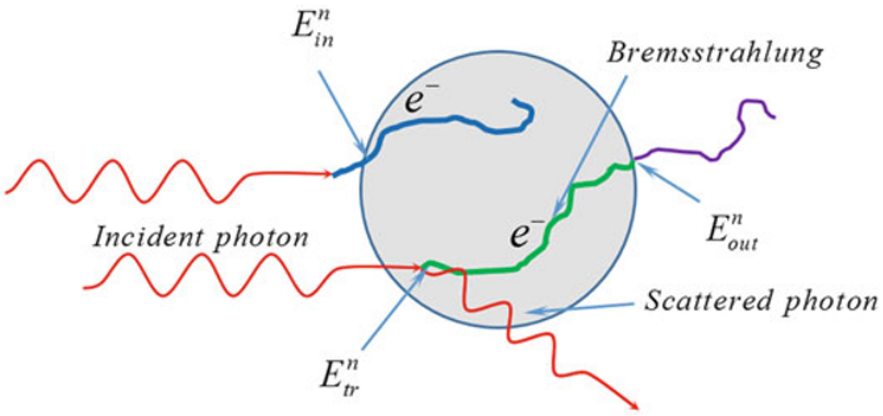

Figure 1.8: Schematic representation of the quantities concurring to the imparted energy. Acknowledgments to [6].

It is now possible to introduce the dosimetric quantities. The ones of interest for the objectives of this thesis are:

- *Kinetic Energy Release per unit Mass (KERMA)*: quantifies the average amount of energy transferred from indirectly ionizing radiation to charged particles, including the energy that could be dissipated in radiative losses by charged particles emitted in V, per unit mass:

$$K = \frac{d(\epsilon_{tr})_{exp}}{dm} \tag{1.19}$$

  where $(\epsilon_{tr})_{exp}$ represents the expectation value of the transferred energy. Because the kinetic energy transferred to secondary charged particles can be dissipated through collision and radiation losses, KERMA can be written as the sum of two components, the collisional and the radiative ones:

$$K = K_c + K_r \tag{1.20}$$

  The dissipation of energy by collisions is predominantly local only when the ranges of the resulting secondary charged particles are small compared to the characteristic dimensions of the scoring volume; otherwise, a fraction of the collisional energy may escape the volume. By contrast, energy dissipated through radiative processes (for example Bremsstrahlung) is transported by photons that can deposit their energy at distances comparable to their mean free path, often much larger than the microscopic interaction region, unless reabsorbed nearby in high Z or sufficiently thick media. This is why, in the absence of charged particle equilibrium (CPE), K and D differ (with K generally overestimating D), whereas under CPE one has $D = K_c$.

- *Absorbed Dose*: is the expectation value of the energy imparted to matter, from directly and indirectly ionizing radiation per unit mass:

$$D = \frac{d(\epsilon)_{exp}}{dm} \tag{1.21}$$

- *Dose Rate*: is the amount of dose deposited over a time interval dt.

$$\dot{D} = \frac{dD}{dt} \tag{1.22}$$

It is important to outline the difference between KERMA, schematically represented in Figure 1.9, and Absorbed Dose. In fact, the first quantity can be expressed as the product of a radiometric quantity, describing the characteristics of a radiation field, and an interaction coefficient, which depends on the properties of the radiation and the medium in which the interaction occurs.

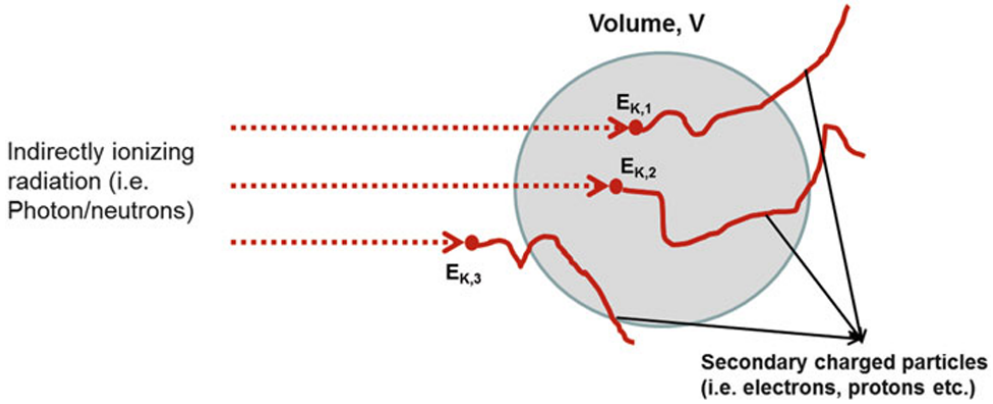

Figure 1.9: The figures represents the transferred energy in the case of KERMA in a volume V. Here, E_{K1} and E_{K2} represent kinetic energies transferred by radiations inside V, while E_{K3} outside. Acknowledgments to [6].

In a photon field, the KERMA at a point P, for an infinitesimal mass element dm surrounding P, is linked to the energy fluence Ψ through the Energy Transfer Coefficient $(\mu_{tr}/\rho)_{E,Z}$, which depends on the energy of the photons and the atomic number of the absorbing medium.

$$K = \Psi \cdot \left(\frac{\mu_{tr}}{\rho}\right)_{E,Z} \tag{1.23}$$

In a neutron field, the KERMA is expressed as the product between the particle fluence Φ, the energy and the Energy Transfer Coefficient:

$$K = \Phi \cdot E \cdot \left(\frac{\mu_{tr}}{\rho}\right)_{E,Z} \tag{1.24}$$

On the other hand, it is not possible to write similar relations for the absorbed dose, as dose estimation requires the follow-up of secondary charged particles, which may randomly escape

the volume and deposit energy outside. While KERMA depends on the physical interaction processes that transfer energy from uncharged to charged particles, the absorbed dose D depends on how this transferred energy is subsequently distributed and deposited within the medium. In other words, K quantifies the energy transferred to secondary charged particles, whereas D accounts for the energy actually deposited inside the volume of interest, after considering that some secondary electrons may leave it and that a fraction of their energy can be lost through radiative processes.

Under Charged Particle Equilibrium (CPE) condition the equation $D = K_c$ is valid, otherwise $D \neq K$ and secondary charged particles must be followed explicitly. CPE conditions are satisfied when the energy carried by charged particles into the volume is equal to the energy carried by charged particles out of the volume.

$$\overline{(R_{in})_c} = \overline{(R_{out})_c} \tag{1.25}$$

This condition can only be fulfilled when the number and the energy of secondary charged particles entering a given volume are equal to those leaving it. A necessary requirement is that the range of the produced secondary electrons is small compared to the dimensions of the scoring volume, so that the charged particles generated outside the volume are replaced by those escaping from it. Homogeneity of material composition and density, together with a uniform radiation field and the absence of strong inhomogeneous electric or magnetic fields, are additional favourable factors, but they are not sufficient on their own. In practice, CPE is typically established at depths beyond the build-up region of photon or electron beams, where charged particles production and loss reach equilibrium.

From a practical and computational point of view, it is very useful, because, when verified, the following equation is valid:

$$D = K_c \tag{1.26}$$

CPE allows to replace a quantity that depends on secondary charged-particle transport, the absorbed dose D, with a quantity determined by primary-field descriptors and interaction coefficients, the collisional KERMA K_c. Indeed, while D typically requires explicit transport (or specialized calorimetry), K_c can be evaluated from the energy fluence Ψ and the mass energy–transfer coefficient (μ_{tr}/ρ). Hence, under CPE the dose can be obtained directly as $D = K_c$.

However, the CPE condition is not always fulfilled. It may be lost, for example, near material interfaces, at beam edges, or in very small or highly heterogeneous volumes. The key point is not only that secondary charged particles can leave the volume, but that they are not replaced by an equivalent number of incoming particles. In such cases, the balance between particles entering and exiting the volume is broken, and the absorbed dose and KERMA no longer coincide. For this reason, detailed radiation transport information are required whenever CPE cannot be assumed.

1.1.5 Dosimeters

To measure the effects of radiation and the dose deposited in a given irradiated material, devices called dosimeters are employed. An important characteristic of dosimeters is that they possess at least one physical property that changes in a well-defined way as a function of the measured dosimetric quantities. The properties required for a dosimeter are [7]:

- Accuracy, repeatability and reliability of measurement.
- A response (possibly linear) that can be calibrated without showing saturation.
- A good spatial resolution.
- Sufficient temporal resolution to accurately follow the time structure of the radiation field, including variations in dose rate or pulsed delivery.
- Energy, angle, temperature and dose rate independence.

It is very difficult to build a dosimeter able to satisfy all these conditions simultaneously and for every radiation field, so the choice of the sensor to be used for dosimetry often depends on the specific application.

Dosimeters can be classified as active and passive. The formers can provide real-time information, the latter give an integrated information that is normally accessible only after irradiation conclusion.

Another possible classification is on the different physical principles of operation, distinguishing among optical, charged-based and chemical dosimeters [8].

Optical Dosimeters

Dosimeters in this class rely on the luminescent response of specific materials, which emit light in the UV, visible, or infrared range when exposed to ionizing radiation. The emission may occur spontaneously (radioluminescence, RL or RIL), or it can be induced by heating (thermoluminescence, TL) or by optical stimulation (optically stimulated luminescence, OSL). The resulting light signal can be quantitatively correlated to radiation dose or dose rate once proper calibration is performed. Due to dose deposition, free electrons and holes are created. These can either recombine directly or become trapped at defect sites within the crystal lattice, acting as storage or recombination centers. Upon external stimulation, the trapped carriers can be released, producing luminescence. This is the case, for example, of TL or OSL. By contrast, in RIL the emission occurs spontaneously during irradiation without the need for stimulation, while in RIA-based dosimetry no luminescence is involved, and the radiation response is quantified as an attenuation of the transmitted signal along the fiber. Such detectors, often referred to as scintillators, cover a broad spectrum of materials, including crystals, optical ceramics, nanostructures, and glasses.

Charge Based Dosimeters

This group of detectors relies on charge production and collection mechanisms to link the generated signal with dose and dose rate. Ionization chambers operate by applying an external electric field that sweeps ion pairs toward the electrodes. However, at high dose-per-pulse conditions,

recombination effects may reduce sensitivity. They are mainly employed for beam calibration and reference dosimetry. Semiconductor devices, such as silicon diodes, provide higher sensitivity and faster time response, making them suitable for pulsed radiation fields. Their working principle is based on charge separation in the depletion region of a p–n junction, but their response is affected by factors such as temperature, accumulated dose, and beam geometry, which limits their use as absolute dosimeters. Dosimeters called MOSFETs, on the other hand, exploit threshold voltage shifts induced by charge trapping in the gate oxide. They offer good spatial resolution and allow real-time measurements, although their sensitivity changes with dose history and temperature. Diamond detectors work in a way similar to diodes or ionization chambers, with high spatial resolution and tissue-equivalent response, but require pre-irradiation to minimize polarization effects. Finally, Radio-Photoluminescence (RPL) dosimeters, typically based on silver-doped phosphate glasses, belong to the family of luminescence-based techniques and are therefore classified as optical dosimeters. In this case, radiation creates stable luminescent centers that can be stimulated by ultraviolet light. The resulting signal is linear with dose at relatively low levels, while at higher exposures additional optical absorption effects arise, which is why ongoing studies are aimed at extending their applicability [9].

Chemical Dosimeters

Film dosimeters, including radiochromic films and polymer gels, are widely used for monitoring cumulative doses of X-rays, γ-rays, neutrons, and electrons, typically in the range of tens of μGy up to several Gy. Their near water-equivalence makes them suitable for applications in personal dosimetry and in mapping dose distributions in radiotherapy. They consist of a silver halide emulsion embedded in a gelatin matrix. Radiation exposure induces redox reactions that modify the optical absorption spectrum, with the intensity of the change directly linked to the absorbed dose. Owing to their micrometer-scale thickness, films offer high spatial resolution and enable detailed analysis of dose uniformity. Nevertheless, they are single-use devices and their response may be affected by environmental factors such as temperature and chemical exposure.

Another very general and widely adopted distinction, introduced for example by [1], separates dosimeters into passive and active devices.

Passive dosimeters accumulate the effect of radiation during the exposure and require a post-irradiation process to extract the information. Their signal is therefore accessible only after the irradiation has ended, and it typically corresponds to a quantity integrated over time. Common examples include photographic films, TLDs, RPL glasses, and chemical dosimeters. They are widely used for personal monitoring, quality assurance, and situations where cumulative dose is of interest. However, their main limitation is the lack of real-time information, which makes them unsuitable for applications where the temporal evolution of the dose or the instantaneous dose rate is critical.

Active dosimeters, by contrast, provide an output signal in real time during irradiation. This signal can be electrical or optical, and is usually proportional to the absorbed dose or to the dose rate. Examples include ionization chambers, semiconductor detectors, and scintillators. Their key advantage is the ability to follow the time structure of the radiation field, allowing online monitoring and immediate feedback. For this reason, active dosimeters are essential whenever

dynamic conditions are present, such as pulsed beams, varying dose rates, or when beam stability needs to be verified continuously.

Within this framework, optical fiber–based dosimeters belong to the category of active detectors but also occupy a unique position among them. While they share similarities with luminescence dosimeters in their ability to convert radiation-induced processes into measurable light signals, their geometry, material flexibility, and capability for remote readout make them fundamentally different from traditional systems. These features enable their use in environments where conventional detectors would be impractical, offering real-time, high-resolution, and minimally invasive dosimetry. In particular, the extremely small space required by optical fibers and their negligible perturbation of the surrounding field make them especially advantageous in constrained experimental configurations. For these reasons, optical fiber dosimetry has become a rapidly developing field, and in the context of this thesis it will be investigated for feasibility studies within the thermal column of the TRIGA reactor in Pavia.

1.2 Optical Fibers Dosimetry

Optical fibers are dielectric waveguides that operate on the principle of total internal reflection. They typically have a cylindrical geometry and are composed of three concentric layers, from the innermost to the outermost: core, cladding, and coating (Figure 1.10). The basic material of both the core and the cladding is amorphous silica (SiO_2), chosen for its excellent transparency, mechanical stability, and radiation hardness. To tailor their optical properties, controlled amounts of selected dopants can be introduced into the silica matrix. For example, germanium or phosphorus can be added to increase the refractive index of the core, while fluorine can be used to reduce that of the cladding. In this way, custom fibers can be realized with specific guiding or radioluminescent characteristics. The coating, instead, has the sole function of providing mechanical protection and is typically made of polymers such as acrylate or polyimide [7].

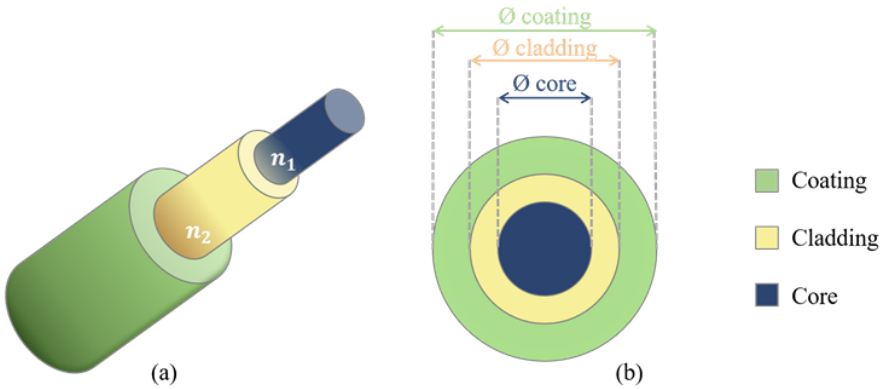

Figure 1.10: Structure of an optical fiber. Acknowledgments to [7].

Reflection is a phenomenon that occurs at the interface between two materials characterized by different refractive indexes, which are defined as the ratio between the speed of light in vacuum and the speed of light in the specific material. In the case of optical fibers, the refractive index

of the core n_1 is larger than that of the cladding n_2, to confine the light in the core and allow its propagation. The necessary condition for the total reflection of the light traveling inside the fiber are obtained by Snell's law [10] and it is expressed as:

$$\theta > \theta_c = arcsin\left(\frac{n_2}{n_1}\right) \tag{1.27}$$

Here, θ is the *reflection angle* and θ_c is the *critical angle* that we need to overcome to have total reflection. If the incidence angle exceeds the critical angle defined by Snell's law, the condition of total internal reflection (TIR) is satisfied. Under TIR, light is fully reflected at the core–cladding interface and no refraction occurs in the cladding. This mechanism is responsible for guiding the signal along the fiber core. It should be noted, however, that TIR does not imply perfect transmission through the core: intrinsic attenuation mechanisms such as Rayleigh scattering, absorption from residual defects, and, in radiation environments, RIA still contribute to the overall signal loss. Optical fibers are engineered to minimize such effects, but their presence ultimately determines the fiber transmission performance.

When light is coupled from air into the fiber core, the *incidence angle* ϕ in air and the *transmission angle* ϕ' in silica determine the *propagation angle* θ inside the core with respect to the core–cladding interface. For total internal reflection to occur, θ must be larger than the critical angle θ_c, defined by Eq. 1.27. This imposes a maximum acceptance angle for ϕ, which is commonly expressed in terms of the fiber numerical aperture (NA). In practice, dedicated coupling systems ensure that injected light satisfies these conditions, so the exact angular dependence is not a limiting factor for the applications discussed in this work.

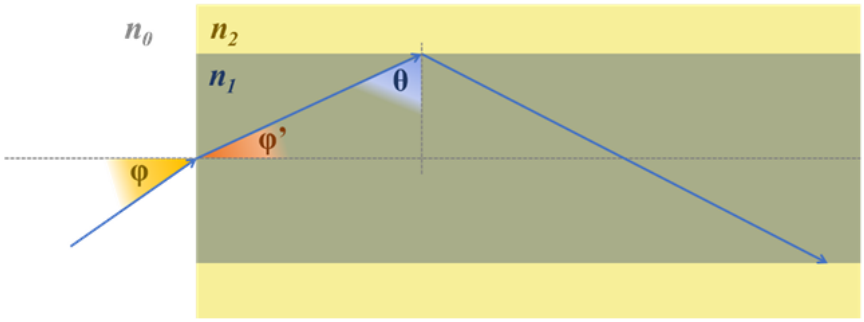

Figure 1.11: Schematic representation of the internal reflection mechanism in an optical fiber. Here, n_0 is the air refractive index and ϕ and ϕ' are respectively the incidence and transmission angle. Acknowledgments to [7].

When optical fibers are exposed to ionizing radiation, the deposited energy produces electron–hole pairs within the amorphous silica matrix. Some of these carriers recombine immediately, while others are trapped at pre-existing imperfections or at newly created sites, leading to the formation of point defects. The generation, migration, and transformation of these defects constitute the microscopic basis of radiation damage in silica-based fibers.

The presence of such defects modifies the optical properties of the material, giving rise to observable macroscopic phenomena. In particular, changes in absorption, spontaneous light emission during irradiation, or modifications of the refractive index are direct consequences of the defect population and its dynamics under irradiation. Measurements of these phenomena provide practical observables that can be correlated with dose deposition, although they only offer indirect insight into the microscopic nature of the defects.

Among these manifestations, three effects are generally considered as the most relevant for optical fibre dosimetry: **Radiation Induced Attenuation (RIA)**, **Radiation Induced Emission (RIE)** and **Radiation Induced Refractive Index Change (RIRIC)** [11][12]. For the purpose of this manuscript we will focus only on the first two mentioned.

1.2.1 Radiation Induced Attenuation

The working principle of optical fiber dosimetry relies on the presence of defects in the silica matrix, which act as optically active centers. Even though a limited number of such defects already exists in the pristine fiber, exposure to ionizing radiation generates additional ones. These radiation-induced defect structures can interact with photons from the ultraviolet to infrared range traveling through the fiber, leading to their absorption and, consequently, to a measurable attenuation of the transmitted light intensity. Since the concentration of defects increases with absorbed dose, the resulting optical signal can be correlated to the radiation dose.

Radiation Induced Attenuation (RIA) is the excess of optical loss caused by irradiation, which adds to the intrinsic attenuation of the fiber. The latter is mainly due to Rayleigh scattering and to absorption from residual defects inevitably introduced during the manufacturing process. Optical fibers are designed for telecommunication purposes to be as transparent as possible, so that light can propagate over long distances with minimal losses. Under irradiation, however, this transparency is compromised: radiation generates additional point defects that absorb or scatter light, thereby increasing the overall attenuation compared to the pristine condition.

The magnitude of RIA depends on the concentration of radiation-induced defects and therefore increases as a function of the absorbed dose, for example with irradiation time, and also scales with the fiber length considered. This increase in optical losses can be quantified using the following relation:

$$\mathrm{RIA}(\lambda, t)\ \left[\frac{\mathrm{dB}}{\mathrm{km}}\right] = \frac{10}{L\ (\mathrm{km})} \log_{10}\left(\frac{I_0(\lambda) - I_{\mathrm{noise}}(\lambda)}{I(t,\lambda) - I_{\mathrm{noise}}(\lambda)}\right) \tag{1.28}$$

Here, L is the fiber length (in km). The measurement is performed in transmission, for example by comparing the light collected at the fiber output before and after irradiation. $I_0(\lambda)$ represents the transmitted intensity at wavelength λ before irradiation, while $I(t, \lambda)$ is the transmitted intensity after an irradiation time t. Both quantities are expressed as photon counts per unit time recorded by the spectrometer, and the instrumental noise contribution $I_{\mathrm{noise}}(\lambda)$ is subtracted to obtain the net signal. This formulation explicitly accounts for the spectral dependence of RIA and reflects the practical procedure used in the experiments.

For dosimetric purposes, only specific types of optical fibers can be employed, namely those in which the RIA exhibits a dose dependence fulfilling the requirements of a measurable dosimetric quantity. This includes a response that is linear, or at least monotonic, with absorbed dose, independent of the dose rate, and not affected by significant recovery during irradiation. Such behaviour is typically observed only within certain ranges, as saturation effects may occur at high doses and the usable spectral window is limited to specific wavelengths. The sensitivity of the fiber can be tuned by modifying the dopant type and concentration, thus enabling the design of fibers with enhanced radiation response. Under these conditions, a calibration procedure can be established to relate the measured RIA to the absorbed dose. Among the various compositions, phosphorus-doped (P-doped) fibres are well known for their high sensitivity to ionizing radiation and are therefore commonly employed in RIA-based dosimetry [12]. In this work, P-doped fibres have been selected as the reference material for this type of experimental investigations.

It is important to consider that part of absorbed signal can be recovered after irradiation conclusion, resulting from the reorganization of the silica matrix due to the presence of metastable defects. This can lead to RIA decrease after irradiation end. For most dosimetric applications, null or very limited recovery effects are desirable [12].

1.2.2 Radiation Induced Emission

Ionizing radiation leads to dose deposition within the fiber, causing electronic transitions in the materials composing the core and the cladding. The electron–hole pairs produced in this process can acquire mobility within the silica matrix and recombine at specific centers, a mechanism that may be accompanied by photon emission. This phenomenon is referred to as Radiation Induced Emission (RIE) and it is represented schematically in Figure 1.12.

The contribution to RIE of interest for this thesis is Radiation Induced Luminescence (RIL), also referred to as radioluminescence (RL). In contrast to RIA, which is typically exploited to build dosimeters capable of measuring the total integrated dose, RIL provides a signal that is emitted during irradiation and is therefore directly proportional to the instantaneous dose rate. This distinction is crucial for applications where real-time monitoring is required.

RIL can originate from radiation-induced point defects, but its efficiency can be strongly influenced by the presence of dopants introduced during fibre manufacturing. In particular, fibers doped with rare-earth ions such as Ce^{3+} or Gd^{3+} contain scintillating centres that enhance radioluminescence and have therefore been traditionally used for dosimetric applications [12].

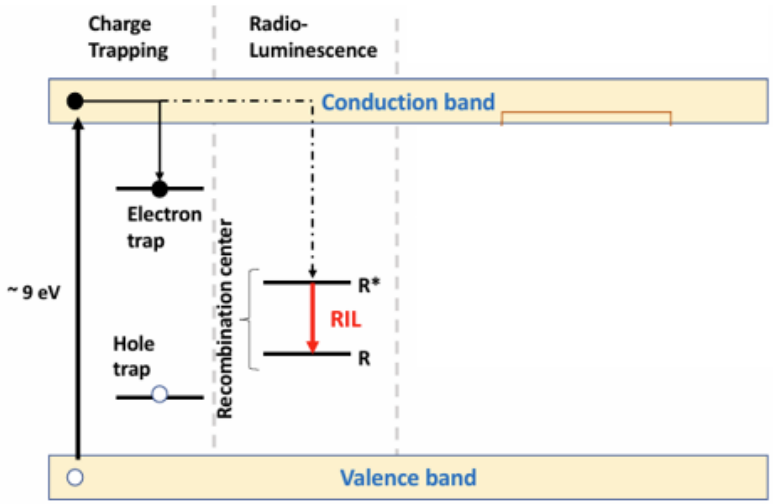

Figure 1.12: Schematic representation of radiation-induced electronic transitions in silica fibers. The process of interest for this work is the recombination of electron–hole pairs at specific centers, which can be accompanied by photon emission (RIL). Adapted from [12].

1.2.3 Optical Fibers Advantages and Applications

Optical fibers present several significant advantages for operation in radiation environments. A first key benefit lies in their immunity to electromagnetic interference, which arises from the dielectric nature of silica and the transmission of information through light pulses. A second advantage is their high bandwidth and multiplexing capability: optical fibers can transfer large volumes of data per second, exploiting techniques such as spectral, spatial, polarization, or modal multiplexing. Another notable characteristic is their low weight and volume, which also ensures minimal intrusiveness. This property is particularly valuable in fields such as space applications and nuclear technology, as it contributes to reducing the overall volume of radioactive waste. Finally, optical fibers with dedicated coatings can reliably operate over an exceptionally wide temperature range, from a few kelvin up to 1000 K. Taken together, these advantages explain the widespread use of optical fibers across many domains.

For medical applications, optical fibers offer several potential uses. In this work, we are particularly interested in their role as dosimeters for the characterization of radiation beams employed in therapeutic treatments. This research area is rapidly evolving: optical fibers have already been employed for real-time beam monitoring during radioisotope production [13], as well as in proton therapy [14], where they can act as multi-point sensors to increase patient safety and improve treatment precision. Building on these advantages, in this thesis we will explore the feasibility of applying optical fiber dosimetry to Boron Neutron Capture Therapy (BNCT), which will be introduced in the next paragraph, and to FLASH radiotherapy.

1.3 Boron Neutron Capture Therapy

Boron Neutron Capture Therapy is a binary form of radiotherapy. It is based on the combined effect of neutron irradiation and the administration of an isotope (in this case ^{10}B) that has a high cross section for neutron capture reaction. Specifically, the reaction of interest is ^{10}B (n, α) ^{7}Li (Figure 1.13). This forms an unstable state that produces high LET secondaries: a 7-lithium nucleus and an α particle. The therapy principle is that boron can be concentrated into the tumor via specific carriers, allowing a boron tumor-to-normal tissue concentration ratio of at least 3 [15]. Low energy neutrons interact with elements in biological tissues, depositing energy via different mechanism, however, the cross section of neutron capture in ^{10}B is higher than all the others in tissues, with a value of 3840 barn at 0.025 eV. Table 1.1 lists the energy ranges and penetration depths, referred to tissue equivalent material, which characterize the reaction products.

Particle	Energy (MeV)	Range (μm)
α	1.47 - 1.78	9 - 10
^{7}Li	0.84 - 1.01	4 - 5
γ	0.48	-

Table 1.1: Energy and ranges of the products of the neutron capture reaction of ^{10}B.

The ranges of the secondaries are comparable with the average cell diameter. This is one of the main advantages of BNCT: the particles produced into tumor cells do not affect surrounding tissues, potentially healthy. The γ is included in the table because, in 93% of cases, ^{7}Li is produced in an excited state and it returns to its ground state with the emission of a 478 keV photon. However, the contribution of this photon to tumor dose is minimal, as its high penetration allows it to escape the patient's body without depositing significant local energy.

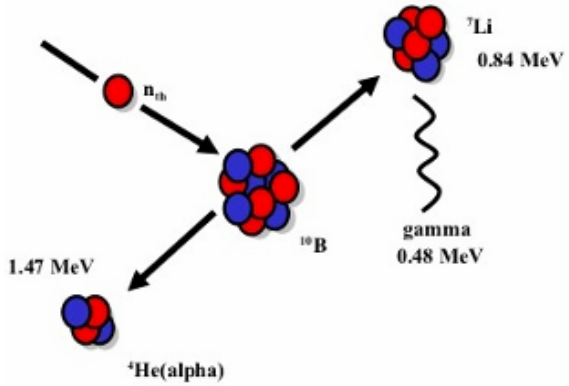

Figure 1.13: Schematic representation of the Boron Neutron Capture Reaction with the production of ^{7}Li in its excited state [16].

The therapeutic effect of BNCT arises from these high LET secondary particles, which create dense ionization tracks and induce complex, irreparable double-strand DNA breaks, eventually leading to tumor cell death.

For optimal treatment, it is essential to use carrier molecules that can selectively accumulate in tumor cells while avoiding healthy tissue. Achieving the correct microscopic distribution of ^{10}B is therefore crucial. This selectivity can be expressed as the ratio between the ^{10}B concentration in tumour cells (C_T) and in normal cells (C_S):

$$T_C = \frac{C_T}{C_S} \tag{1.29}$$

Values in the range of 3–5 are typically reported in the literature and allow successful treatment [17].

Because the reaction products are highly ionizing particles with high LET, even a single track crossing the cell nucleus can deposit sufficient energy to cause clustered DNA damage that may lead to cell death. This is in contrast to low-LET radiation, where multiple tracks or repeated hits are often required to achieve a similar biological effect. The likelihood of significant energy escaping from the cell where the reaction occurs is low, meaning that surrounding healthy cells are largely spared. This represents a fundamental difference from conventional external beam radiotherapy, where selectivity relies on shaping and conforming the photon or proton beam to the tumor volume. In BNCT, by contrast, selectivity arises from the boron distribution within the tissue and is independent of the geometrical shape of the neutron beam. As a result, the neutron field can be kept broad enough to encompass not only the whole tumor volume but also neighbouring regions that may host isolated malignant cells undetectable with standard diagnostic techniques, which could lead to the development of metastases or recurrence if untreated [18].

Another notable advantage is that dose delivery occurs only during neutron irradiation, as the reaction products are non-radioactive. The rest of the patient's body is therefore spared from unnecessary exposure. Although sodium and chlorine in the body can be activated by neutron irradiation, the resulting dose is negligible [19]. This differs from traditional radiotherapy using radioisotopes, where the absorbed dose can also be delivered to tissues far from the tumor site.

This intrinsic selectivity makes BNCT a potential option for the treatment of tumors that are surgically inaccessible or unsuitable for other radiotherapy techniques, for example when the tumor margins are not well defined, located in proximity to radiosensitive structures, or infiltrating surrounding healthy tissues [20].

Given that both selectivity and localized dose release are key features of BNCT, accurate dosimetry of neutron beams is of primary importance. This is true not only in the clinical context, where beam quality assurance is mandatory for treating patients, but also in research, particularly in radiobiology. In fact, preclinical *in vitro* and *in vivo* experiments require precise knowledge of the absorbed dose to correlate biological effects with radiation exposure. However, dose assessment in BNCT is particularly challenging, as it results from multiple components associated to different radiation contributions, that are difficult to disentangle. For this reason, biological experiments often rely on simulations of the deposited dose [21]. Such simulation models, once validated by experiments, can be used to estimate dose components in a specific set of irradiation conditions and on a defined target geometry. However, they do not provide real-time information on the ongoing experiments or treatment planning as, for example, they cannot account for possible fluctuations of the actual beam. The availability of an experimental dosimeter capable

of validating simulations and directly measuring the delivered dose would therefore represent a significant improvement. In this framework, optical fibers offer a promising approach.

1.3.1 Mixed Field Dosimetry

For all the radiotherapy techniques, the safety and effectiveness of the treatment are determined by the ability to calculate the dose deposited in tissue with high accuracy. In the specific case of BNCT, dose estimation is complex, due to the nature of neutron energy deposition, which leads to a mixed radiation field in the biological tissue. Each radiation component has distinct physical properties and, consequently, different interaction with matter and dose deposition, and a different effectiveness in producing biological damage at equal dose.

Energy deposition from epithermal and fast neutrons in biological tissue is primarily due to recoil protons generated through elastic scattering with hydrogen nuclei: $^1H(n,n')^1H'$. As neutrons scatter, they lose energy, progressively thermalizing with depth. When an epithermal neutron beam is used, the spectrum is harder in superficial tissue layers and becomes predominantly thermal at greater depths. This energy moderation is strategically designed so that the neutrons are thermalized at the tumor location, maximizing neutron capture by boron. This is why BNCT neutron fields are epithermal when tumors to be treated are deep seated.

At thermal energies, neutron interactions are dominated by capture reactions. Among them, the most relevant in terms of contribution to local energy deposition are the one of ^{16}O and ^{12}C. Hydrogen capture $^1H(n,\gamma)^2H$ produces a 2.2 MeV photon, whose energy is mostly carried away and deposited far from the interaction site. Nitrogen capture, instead, produces a 583 keV proton and a ^{14}C recoil nucleus, which deposit their energy locally. These last two reactions, along with the scattering reaction with hydrogen, lead to an unavoidable, non-selective dose to both tumor and healthy tissues, differently from the selective component coming from the products of the boron neutron capture reaction. Another unavoidable background dose is due to the prompt γ component intrinsically present in any neutron beam. In reactor-based facilities this originates mainly from fission processes, while in accelerator-driven or generator-based sources it arises from nuclear reactions in the target and surrounding structures. Although this component can be reduced with appropriate shielding, it cannot usually be suppressed to negligible levels.

The total absorbed dose in both tumor and normal tissues is the sum of the above-mentioned components, characterized by different LET values and, therefore, different radiobiological effectiveness. They can be summarized as:

- D_B : boron dose, from the neutron capture reaction $^{10}B(n,\alpha)^7Li$;
- D_N : nitrogen dose, from the reaction $^{14}N(n,p)^{14}C$, mainly due to protons and ^{14}C recoiling nucleus;
- D_γ : gamma dose, it is due to the incident gamma dose (background photons) and induced prompt gamma dose (hydrogen capture reaction $^1H(n,\gamma)^2H$ with the emission of 2.2 MeV);
- D_H : hydrogen dose, it is the induced proton-recoil dose from $^1H(n,n')^1H'$ scattering reaction, energy released by the recoiling protons produced in the interactions with H of

fast and epithermal neutrons.

The coexistence of these components is at the core of one of the main challenges in BNCT dosimetry. Conventional detectors generally lack the ability to distinguish between them, so their signals represent a convolution of neutron and photon induced effects. This limits the determination of the individual dose contributions and their biological relevance. In clinical applications, this limitation might affect beam quality assurance and, in the most critical scenarios, possibly compromise patient safety. In preclinical research, the lack of detailed dosimetry makes the correlation of biological effects with radiation exposure difficult to establish. Although Monte Carlo simulations are commonly employed to estimate dose distributions, they cannot capture beam instabilities or experimental uncertainties, or intrinsic differences between the real case and the simulated model.

These limitations underscore the need for innovative dosimetric tools. Optical fiber-based detectors offer several advantages in this context. Their small size enables minimally invasive in-phantom or *in-vivo* use, their flexible geometry and remote readout capabilities make them well suited for reactor environments and their light-based response can, in principle, be directly correlated with radiation-induced processes. Furthermore, their composition and doping can be controlled with high precision, enabling the fabrication of custom-made fibers tailored to enhance sensitivity to specific radiation fields. These properties suggest that optical fibers could represent a valuable solution to some of the unresolved challenges in mixed-field dosimetry for BNCT.

For these reasons, this thesis explores the feasibility of using optical fibers as dosimeters in the thermal column of the TRIGA reactor in Pavia, where a thermal neutron field is exploited for BNCT experiments in cell cultures and small animals, and also for other medical applications, such as FLASH therapy. The following chapter describes in detail the experimental facility and the setup employed for the measurements.

1.4 Research Aim and Objectives

Conventional dosimeters often face limitations in serving the BNCT dosimetry requirements, either because of their size, their sensitivity to environmental factors, or their inability to provide real-time, spatially resolved measurements. Optical fibers, due to their small dimensions, flexibility, and capability for remote readout, represent a promising alternative that could overcome many of these limitations.

The specific objectives of this research are the following:

- to identify the challenges of dose measurement in mixed neutron-photon fields, with a focus on BNCT applications;
- to assess, through Monte Carlo simulations realized with the PHITS code, the expected behavior of optical fibers when placed in the thermal column of the TRIGA reactor, including energy deposition and dose component separation;
- to evaluate the potential advantages of optical fibers for experimental dosimetry in terms of spatial resolution, minimal perturbation of the radiation field, and capability of providing experimental validation of simulation-based dose estimates;

- To establish the groundwork for subsequent experimental tests, identifying optimal conditions and limitations for the integration of optical fibers in BNCT-related research.

Through the combination of simulation and methodological analysis, this work aims to demonstrate whether optical fiber dosimetry can provide a reliable, practical, and innovative tool for dose measurement in BNCT and other applications involving complex mixed radiation fields.

In addition to addressing BNCT dosimetry challenges, this thesis introduces pulse-resolved RIL tests of medium-OH and Ce-doped fibers, thereby extending the scope of optical-fiber dosimetry to FLASH therapy.

The following chapter will focus on the TRIGA reactor, which provides a representative neutron–photon mixed field for BNCT dosimetry. Afterwards, attention will be shifted to photon irradiation experiments carried out at the PETRA facility, used both as a benchmark environment for fiber characterization and as a platform to explore FLASH radiotherapy conditions.

Chapter 2

Dosimetry in the Neutron and Gamma Mixed Fields of the TRIGA Mark II reactor

The TRIGA Mark II reactor is located at the laboratory LENA (Laboratorio di Energia Nucleare Applicata) of the University of Pavia, Italy. The reactor, shown in Figure 2.1, is a pool-type light-water moderated facility with a nominal steady-state power of 250 kW and a maximum total neutron flux in the central thimble of about 2×10^{13} cm^{-2} s^{-1} [22] [23].

The reactor core is immersed in a cylindrical tank filled with demineralized light water, which acts as coolant, moderator, and biological shield, while a thick graphite reflector surrounds the core to reduce neutron leakage [24].

The reactor is equipped with several irradiation facilities both in-core and out-core. In-core positions include the central thimble, mainly used for neutron activation analysis, isotope production [23] and radiation damage studies on polymeric materials [25] [26] and the pneumatic transfer channel, connected to the radiochemistry laboratory to allow short-lived radioisotope experiments. Out-core facilities include the rotating channel (called *Lazy Susan*), horizontal channels, the Thermal Column (TC), and the Thermalizing Column. In particular, the TC [27][28] is designed to have neutron flux and energy spectra serving the scopes of BNCT experiments and treatments [29][30]. The Thermalizing Column is not used at the moment, and leads to a pool of water designed to irradiate large samples in a fully-thermalized neutron field. The Lazy Susan, located in the graphite reflector surrounding the core, accommodates up to 80 samples for uniform irradiation. The horizontal channels extend radially or tangentially through the reflector, and are used for both basic and applied nuclear physics studies.

Of particular relevance to this thesis is the TC, consisting of an air cavity inside a graphite structure, where an isotropic, and predominantly thermal neutron flux sufficiently intense to perform BNCT radiobiological experiments is present [28]. The irradiation cavity (20.5 cm $\times$ 40 cm $\times$ 103.5 cm) with reduced gamma background has been created inside the column, by shielding the irradiation position with bismuth walls. The irradiation chamber can be accessed from the reactor

Figure 2.1: Picture of the TRIGA Mark II reactor of the University of Pavia, Italy. The yellow part of the reactor is the core, while the Thermal Column is visible in blue. The gray block is the thermalized channel.

hall. Figure 2.2 shows a vertical section of the TC, where the irradiation cavity, part of the reactor core and the access area are visible. Two sliding shutters made of borated concrete are located at the end of the column, allowing flexible shielding of the facility for radiation protection purposes. The TC has been extensively used for BNCT research, as well as for radiobiological experiments in cell cultures and small animals [32][33]. Notably, the Pavia TRIGA reactor is the only facility where BNCT treatment was realized with an organ autotransplant protocol. In this advanced clinical treatment, the liver of two patients affected by multiple metastases were explanted, irradiated in the TC following boron administration, and finally re-implanted in the patients after neutron irradiation [30][29]. This pioneering clinical research inspired several international groups to investigate the same BNCT protocol for liver and other organs [34][35][36][37].

As detailed knowledge of the irradiation conditions is pivotal for the realization of BNCT treatments and radiobiological experiments, several studies have been carried out at the Pavia TRIGA TC to characterize its mixed neutron and photon field.

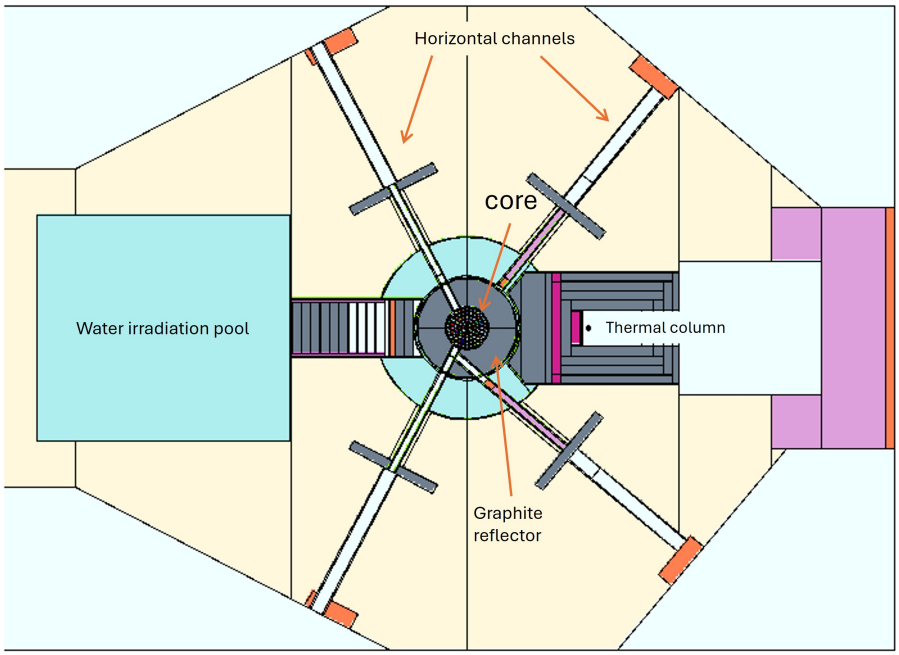

Figure 2.2: Schematic top view of the TRIGA Mark II reactor at LENA. The core is surrounded by a graphite reflector (in gray) and is connected to several horizontal irradiation channels. The TC (in pale blue) is an air cavity visible on the right side, surrounded by graphite. On the left the water irradiation pool (in blue) is visible. Geometrical model obtained with the Monte Carlo code MCNP6.3 [31].

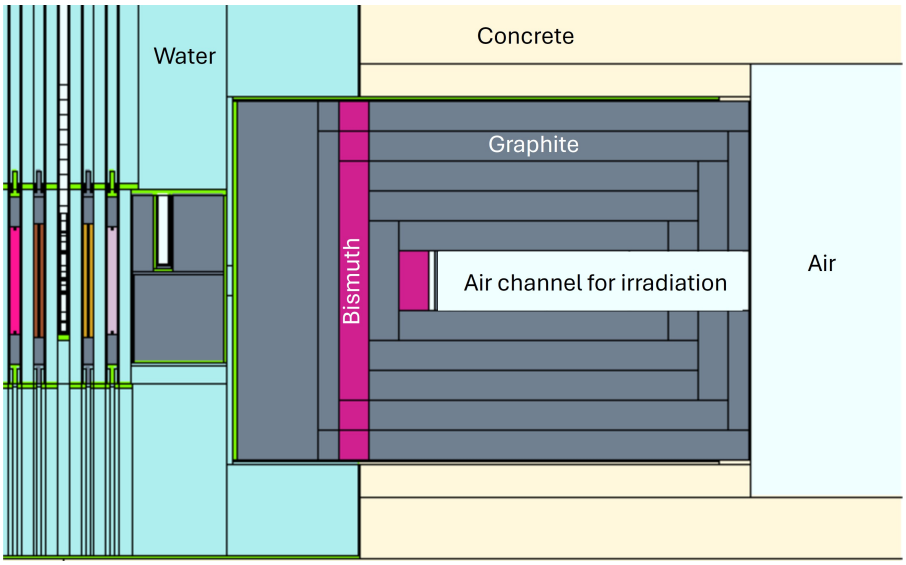

Figure 2.3: Schematic vertical view of the TC of the TRIGA Mark II reactor at LENA (University of Pavia). Different colors represent different materials as reported in the picture. Geometrical model obtained with the Monte Carlo code MCNP6.3 [31]

In these experiments, the accurate determination of absorbed dose has been a central and challenging issue. To date, most studies have largely relied on Monte Carlo simulations, validated from indirect measurements, to integrate and support the design and realization of experimental activities.

A comprehensive characterization of the irradiation positions available at the TRIGA reactor has been achieved through a multi-step effort combining experimental measurements and Monte Carlo modeling. The first stage consisted in neutron spectrum determinations in air by means of multi-foil activation and unfolding techniques [38][27]. In parallel, alanine dosimeters were employed to quantify the photon dose contribution, providing complementary information on the mixed radiation field. These experimental datasets served as reference benchmarks to validate the MCNP transport models used for the reactor. This characterization is described in [28], where the neutron spectrum in one irradiation position and the photon dose in three irradiation positions along the TC are reported.

A robust knowledge of the radiation components in the TC is very relevant because the facility is extensively used for radiobiological experiments in BNCT. Cells cultivated in flasks or tissue samples are irradiated in order to study the biological response as a function of the absorbed dose. An illustrative example is provided by the comprehensive dosimetric evaluation of *in-vitro* BNCT cell survival experiments reported in [32], where KERMA-based estimates were compared with detailed absorbed-dose simulations in cell monolayers. In that study, the absorbed dose to cells was assessed by means of Monte Carlo simulations with the previously validated reactor model, explicitly transporting the secondary charged particles generated by neutron and photon interactions. The resulting dose values were then correlated with measured biological endpoints, enabling a quantitative link between the physical radiation field and its biological effectiveness [39].

However, currently the TC is not equipped with any experimental neutron or photon monitor to measure the dose during the experiments, thus accounting for possible variations or fluctuations. BNCT dosimetry for radiobiology is thus affected by the lack of real-time (or online) dose verification. As a result, BNCT radiobiology at TRIGA still predominantly relies on computational dosimetry only providing average time values. Further experimental benchmarks are accordingly necessary to complement and validate Monte Carlo predictions.

In this framework, the present thesis aims to explore the use of optical fiber dosimeters as a novel tool for real-time, spatially resolved experimental dosimetry in BNCT-related applications. Carrying out measurements in the TRIGA TC is particularly demanding. The irradiation cavity is located within a controlled reactor area with strict access restrictions, and residual activity may persist after operations. In addition, the confined geometry leaves little room for the installation of complex setups. These factors significantly limit the use of conventional dosimeters, which often require manual handling, electrical feedthroughs or post-irradiation readout.

Optical fibers, by contrast, offer the possibility of remote, on-line monitoring with minimal intrusion into the irradiation volume and following impact on the existing radiation fields. This approach has already been demonstrated in other high-radiation facilities, for example at CERN, where distributed optical fiber systems are employed for the online characterization of mixed fields along the particle accelerator complex [40], for in-core reactor irradiation for nuclear waste

monitoring applications [41], for medicine, in-core instrumentation and space applications [12]. Building on these advances, this work investigates whether similar strategies can be applied to the TRIGA TC, where the complexity of the mixed neutron-photon environment and the constraints of reactor operation demand innovative dosimetric solutions.

2.1 Feasibility study for the use of optical fiber-based dosimeters in the Thermal Column

Before optical fibers can be employed as dosimeters in a mixed field, such as the one in the TC of the TRIGA reactor in Pavia, it is necessary to test optical fiber dosimeters under laboratory controlled irradiation conditions that, at least in terms of dose and dose rate, are as close as possible to those expected during operation in the TC. The present study largely builds upon previous investigations already carried out on fiber-based dosimeters, which provide the methodological background for their use in mixed radiation fields [12][42][43].

The experimental work of the present study was carried out at the PETRA X-ray platform [44] of the Hubert Curien Laboratory of the Jean Monnet University, Saint-Etienne, France. This facility offers a well-characterized environment in which it is possible to evaluate the dose–response relationship of the fibers, verify the reproducibility of the measurements, and investigate potential dependencies on external parameters such as dose rate, beam energy, and exposure time (see Chapter 3 Section 2).

Addressing optical fiber response in a reference photon field represents a necessary prerequisite before moving to the more challenging conditions of a complex mixed neutron–photon field. The experiments realized at the PETRA facility (Chapter 3) therefore constituted a fundamental first step in building a robust dosimetric methodology and provided the reference data needed to proceed. This allows the feasibility of a case study specifically targeting the TC to be designed.

Before introducing the PHITS simulations performed for this thesis, it is useful to briefly recall the main results already available from experimental and computational characterizations of the TRIGA thermal column, fundamental starting point of the present work.

As reported in [28][27], the thermal neutron flux in the central irradiation cavity at the most inner position reaches about 2.0×10^{10} $\mathrm{cm}^{-2}\mathrm{s}^{-1}$, with an epithermal-to-thermal ratio below 0.05, confirming the predominance of thermalized neutrons.

Complementary MCNP simulations, previously performed, reproduced these results and provided detailed spatial maps of the neutron and photon fields along the whole column. Such distributions are reported in Figure 2.4 and Figure 2.5, showing that the neutron flux decreases by roughly one order of magnitude along the longitudinal axis of the column, while the photon field remains comparatively more uniform.

These datasets constitute the reference input spectra used in the present work to reproduce, with PHITS, the local radiation environment at specific irradiation positions, thus avoiding the need for a full-core transport simulation.

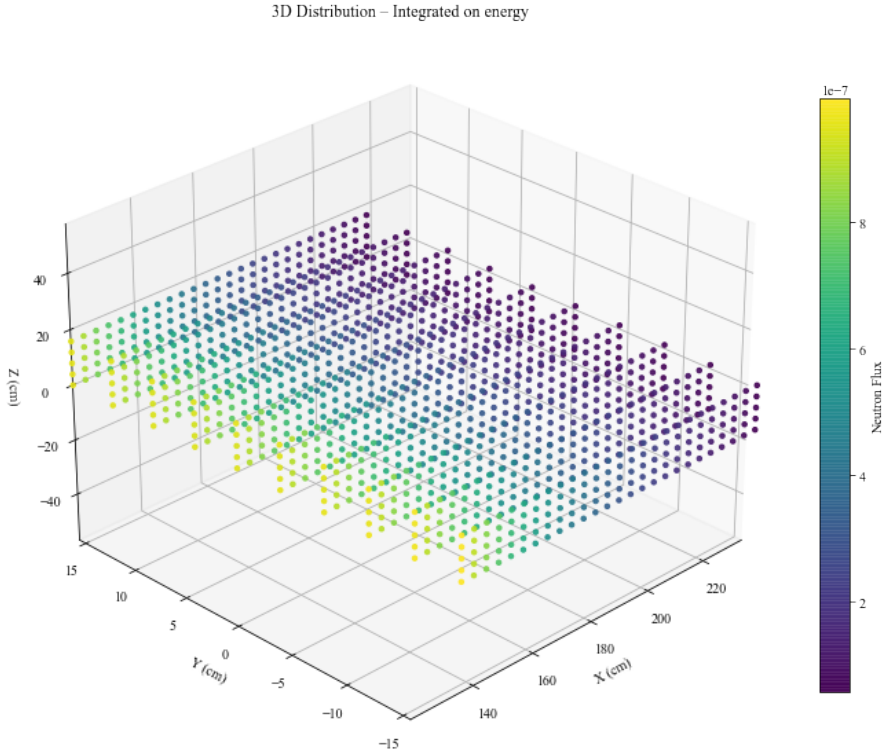

Figure 2.4: Simulated neutron tridimensional flux distributions in the TRIGA thermal column obtained from MCNP calculations.

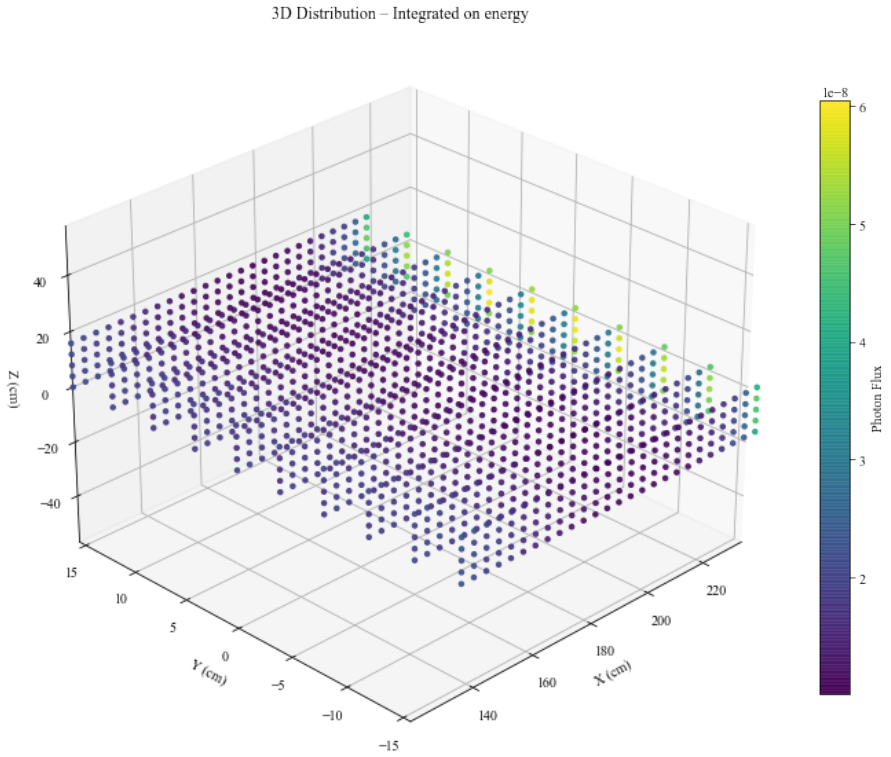

Figure 2.5: Simulated photon tridimensional flux distributions in the TRIGA thermal column obtained from MCNP calculations.

2.2 Dosimetry Monte Carlo simulations

In order to investigate the feasibility of using optical fibers as dosimeters in the mixed radiation field of the TRIGA reactor TC, simulations were performed using the Monte Carlo code PHITS (Particle and Heavy Ion Transport code System)[45][46]. These simulations represent a complementary work to anticipate the expected response of optical fibers when exposed to neutron–photon mixed fields, supporting the design of the experimental measurements and providing integrated information for their interpretation.

The principle behind this approach lies in the intrinsic complexity of dosimetry in BNCT-related neutron fields. As anticipated above, the absorbed dose originates from multiple radiation components, including thermal and epithermal neutrons, recoil protons, capture reactions, and photon backgrounds. Disentangling these contributions is experimentally challenging, since conventional detectors provide convoluted responses that cannot easily be decomposed into their single components.

Monte Carlo simulations overcome this limitation by enabling a particle-by-particle tracking of radiation transport and interactions in the reactor environment. Through PHITS it is possible to calculate the spatial and energy distributions of each component of the radiation field, as well as to estimate the dose contributions associated with the different interaction channels.

In particular, the simulations carried out in this work were designed with two main objectives:

- to characterize the radiation field inside the TC of the TRIGA reactor in Pavia, with emphasis on the relative contributions of neutrons and photons to the absorbed dose (this work had been previously performed in Pavia using MCNP);
- to evaluate the interaction of this mixed field with silica-based optical fibers, in order to assess their potential response and limitations as dosimeters in such an environment.

The results obtained serve a dual purpose. On one hand, they provide predictive data that can be compared with and validated by future experimental measurements. On the other, they highlight specific features of the optical fiber response that may be advantageous for disentangling dose components in BNCT applications.

The following sections describe the simulation setup in detail, including the material modeling of the optical fibers used in the experiments. Results regarding flux distributions, dose components, and expected fiber responses are then presented and discussed.

2.2.1 Particle and Heavy Ion Transport code System

Particle and Heavy Ion Transport code System (PHITS) is a general-purpose Monte Carlo particle transport simulation code, developed through the collaboration of Japan Atomic Energy Agency (JAEA) together with several research institutes worldwide [45]. PHITS is widely employed in applications ranging from reactor physics and radiotherapy to space radiation protection and accelerator design, due to its versatility in handling particle transport over wide energy ranges. This is achieved through the use of multiple nuclear reaction models combined with extensive evaluated nuclear data libraries.

The structure of a PHITS input file is text-based and organized into sections that can be filled using two formats: one based on specific keywords, set as numeric values or strings, and another allowing multiple numerical entries separated by spaces. This flexible structure makes PHITS adaptable to a wide variety of problems while still maintaining consistency across projects. The output is also provided in text format, typically accompanied by additional files, often graphical representations, that summarize calculation results. The code consistently adopts a right-handed Cartesian coordinate system to describe the geometry of the simulated setup.

For the purposes of this thesis, only a subset of PHITS sections is directly relevant [45]:

- [`Title`]: where the title of the project is set.
- [`Parameters`]: defines general calculation parameters.
- [`Source`]: describes the radiation source characteristics.
- [`Material`]: specifies the materials used.
- [`Mat Name Color`]: assigns physical properties to the materials used in the geometry.
- [`Cell`]: to define cells, i.e. spatial regions bounded by surfaces.
- [`Surface`]: specifies the geometry-defining surfaces.
- [`Volume`]: necessary to set the volume of the regions.
- [`Importance`]: to define regions importances.
- [`T-track`]: scores particle fluence in specified regions.
- [`T-deposit`]: scores deposited energy in specified regions.

Among the many particle species that PHITS is capable of transporting, the most relevant for this work are neutrons (referred to by the keyword *neutron*) and photons (referred to as *photon*), as these are the dominant components of the radiation field in the TRIGA TC.

The simulation output is structured into several categories of information that can be distinguished into [45]:

- Basic information, such as the title, the version and the calculation summary;
- Input echo, reproducing the input file for verification;
- Information on memory usage and batches;
- Information on transport particles, including the number and type of transported particles;
- Detailed information: variance reduction, number of scattered particles for each region, information for each material;
- Information on PHITS developers and references.

Scores are referred to as *tally* in PHITS. Tally results are reported together with their statistical uncertainties, typically stored in separate files whose names contain the suffix *err*. These uncertainties are essential for assessing the reliability of the simulation outcome, from the point of

view of statistical convergence. When dealing with complex mixed fields such as those in BNCT, issues may concern on the less intense components of the field.

PHITS also allows users to select different calculation modes, each optimized for specific applications or output requirements. A summary of these modalities is reported in Fig. 2.6, which illustrates the flexibility of the code in adapting to various simulation objectives.

Parameter	Value	Explanation
icntl	(D = 0)	Basic control option.
	= 0	Normal PHITS calculation.
	= 1	Output cross section and kerma factor (please see /phits/sample/icntl1 in detail).
	= 3	Output only input echo for checking memory usage, libraries, and file links.
	= 5	Calculation assuming all regions are void (no reaction, no ionization) for geometry check, and volume and area calculations.
	= 6	Source check. Source positions can be tallied by [t-product].
	= 7	Execute [t-gshow] for graphical output.
	= 8	Geometry output of xyz mesh tally with gshow option for graphical output.
	= 9	Execute [t-rshow] for graphical output.
	= 10	Geometry output of reg mesh tally with rshow option for graphical output.
	= 11	Execute [t-3dshow] for graphical output.
	= 12	Re-calculate using dumpall file. Dumpall file is specified by file(15).
	= 13	Use of function to sum up tally results (Sumtally function).
	= 14	Use of automatic calculation of region volume.
	= 15	Execute [t-wwbg] to obtain [ww bias] parameters.
	= 16	Use of script of analysis function.
	= 17	Execute [anatally] to obtain results of analysis function.

Figure 2.6: Available calculation modes [45].

The choice of PHITS for this thesis is motivated by its proven reliability in modeling neutron and photon transport in reactor environments, as well as its ability to handle complex geometrical configurations. These capabilities are particularly relevant when reproducing the radiation field at the irradiation position, where mixed neutron–photon spectra and steep spatial gradients are present. In this work, PHITS was employed to simulate this local environment using the neutron and photon spectra previously obtained from MCNP calculations, rather than to model the full thermal column geometry.

A specific challenge of this work in the dosimetry point of view lies in the very small dimensions of the optical fibers. This introduces issues of statistical convergence and requires an optimization of the tally configuration, in particular the size and discretization of the scoring regions, to balance spatial resolution with statistical uncertainty. In practice, the core, cladding, and coating were defined as separate tally cells with volumes large enough to ensure sufficient particle statistics while still preserving the microscopic structure of the fiber. Moreover, it is fundamental for BNCT to be able to distinguish the neutron and photon contributions to the total dose, as their biological effectiveness is different. For this reason separate simulations with photons and neutrons as projectiles were developed.

The simulations presented in the following sections were therefore designed to predict the expected behavior of optical fibers in relevant irradiation positions in the TC, and to evaluate their feasibility as experimental dosimeters for BNCT applications.

2.2.2 Simulation setup

The simulations were implemented in PHITS using input files designed to reproduce the field of the two components in the studied position of the TC of the TRIGA reactor in Pavia. Instead of using the full geometrical model of the reactor, the adopted approach relied on neutron and photon spectra obtained from previous simulations at reference positions in the TC by MCNP. This consisted in recording a track-by-track neutron and photon source across the surfaces of a box enclosing the irradiation position, and run the simulations starting by this source. This method ensures higher statistical convergence, avoiding the time-consuming radiation transport in the whole reactor, while keeping a reliable representation of the radiation field in the volumes of interest, hence in the fiber geometry. To further improve calculation time, dosimetry calculations were further simplified by using the spectra present in the positions chosen. The positions where the fibers were simulated were chosen referring to the ones described in [28], also reported in Figure 2.7.

The coordinate system adopted in PHITS was defined consistently with that of the reference MCNP model, with the x-axis corresponding to the longitudinal direction of the thermal column.

In the simulations, the spectra was chosen as if the optical fiber was placed in the position of coordinates $(x, y, z) = (126.95, -2.0, -8.0)$ cm in the MCNP model. A symmetric configuration with respect to the y-axis was also considered. For comparison, the same calculations were repeated at 226.95 cm along the x-axis from the reactor core (referring to positions 1 and 3 reported in [28]). Both neutron and photon source spectra were tested in these irradiation points.

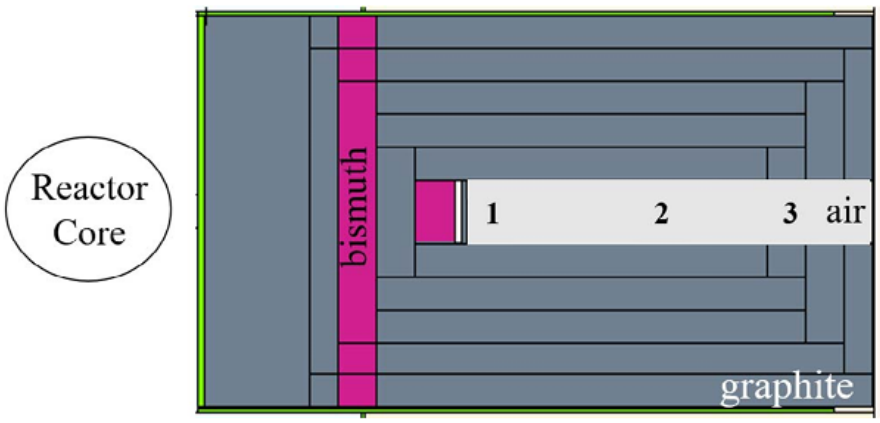

Figure 2.7: Longitudinal view of the reactor model of the TRIGA Mark II thermal column realized with MCNP and adapted from [28]. The neutron and photon spectra were chosen considering in position 1 (130.95 cm from the center of the core) and 3 (208.95 cm from the center of the core). Grey: graphite; magenta: bismuth; green: Boral (borated aluminum); white: air.

The input files were organized into distinct sections, each addressing a specific aspect of the simulation. The tested fibers are the one employed in experiments: P-doped, Ce-doped and M-OH. For brevity, only the complete input file of one representative simulation is reported here as an example, the one with the P-doped fiber sample at position, referred to the MCNP model, $(x, y, z) = (126.95, -2.0, -8.0)$ cm, using photons as projectiles with the correspondent

spectrum.

In the **Parameters** block (Fig. 2.8), general simulation controls were defined. The number of primary particles was set to 10^6, divided into 2000 batches, in order to achieve sufficiently low statistical uncertainties in the tallies. According to the recommendations of the International Commission on Radiation Units and Measurements (ICRU Report 60 [47]), an overall uncertainty within 5% (at one standard deviation) is generally considered acceptable for dosimetric applications; the adopted simulation settings ensured compliance with this accuracy requirement.

Electron–photon transport was activated with a cut-off of 1 keV for electrons, allowing for an accurate description of secondary electron production and transport in the fiber. This threshold corresponds to the lowest transport energy available in PHITS [45]. According to NIST ESTAR data, 1 keV electrons in fused silica have a continuous slowing down approximation (CSDA) range of about 4×10^{-2} µm, several orders of magnitude smaller than the fiber core diameter. Hence, electrons below this energy are effectively absorbed locally, and the chosen cut-off can be considered sufficiently low to ensure accurate local dose deposition within the silica materials [48] [49].

```
[ P a r a m e t e r s ]
 icntl    =      0
 maxcas   =      10e+6   # number of particles per one batch
 maxbch   =      2000    # number of batches
   negs   =      1       # photon positron and electron transportation activated
emin (12) =     0.001    # threshold energy for transportation of electrons
 file(6)  = P_doped_pos_1_1_photon.out          # general output file name
```

Figure 2.8: General simulation parameters used in PHITS. The number of source particles was set to 10^6 in 2000 batches, with electron–photon transport enabled down to 1 keV.

The **Source** (Figure 2.9) block defines the characteristics of the particle source, including its spatial distribution, emission directions, and energy spectrum. In this case, the source is a spherical surface emitting photons so that an isotropic flux is reproduced in its inner volume, with an energy distribution corresponding to the previously simulated spectrum through at the selected irradiation position. The photon (and neutron) energy spectrum, obtained from the MNCP results, is introduced as a continuous distribution, discretized into bins with associated probabilities, derived from the transport results in the TC. The resulting radiation field at different studied positions in the model is obtained through the transport of these particles through the materials.

Figures 2.10, 2.11, 2.12 and 2.13 report the neutron and photon flux spectra obtained from the MCNP model of the TRIGA Mark II reactor in function of energy. The spectra correspond to four positions inside the thermal column, located near positions 1 and 3 detailed in Figure 2.7 at ± 2 cm along the horizontal direction with respect to the longitudinal one. Each spectrum represents the differential particle flux in units of $\mathrm{cm}^{-2}\mathrm{s}^{-1}$, integrated over the energy bin width, and is normalized to the nominal reactor power of 250 kW. These datasets were used as input to reproduce the mixed neutron–photon field in the PHITS simulations.

```
[ S o u r c e ]
   s-type =   9            # spherical shell source
     proj =   photon       # kind of incident nucleus
       r1 =   10.000       # inside radius [cm]
       r2 =   10.000       # outside radius [cm]
       x0 =   0.0000       # center position of x-axis [cm]
       y0 =   0.0000       # center position of y-axis [cm]
       z0 =   0.0000       # center position of z-axis [cm]
      dir =   -all         # Inverse direction against dir=1.0
   e-type =     1          # Continuous energy distribution
       ne =     2
4.000000E-01    1.00852E-08
1.000000E+00    2.22716E-09
1.000000E+01    6.03005E-09
```

Figure 2.9: Definition of the photon source in PHITS. The source is modeled as a spherical surface reproducing an isotropic flux in its inner volume, with an energy distribution corresponding to the simulated photon spectrum at the selected position.

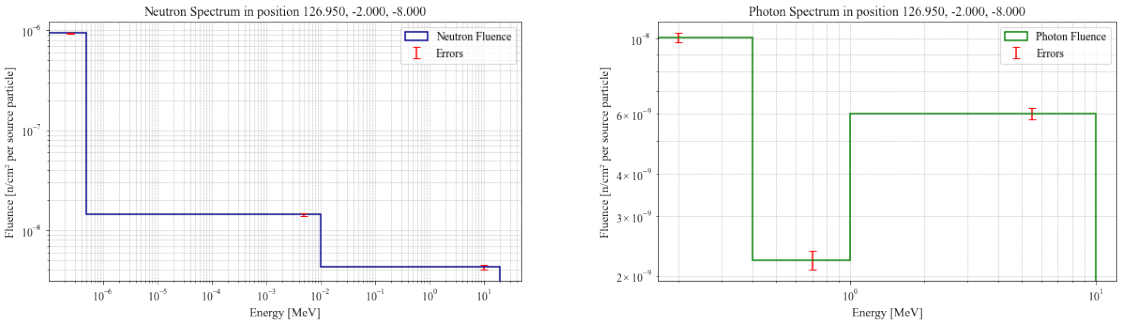

(a) (b)

Figure 2.10: Neutron (a) and photon (b) spectra at the position (226.950, -2.000, -8.000).

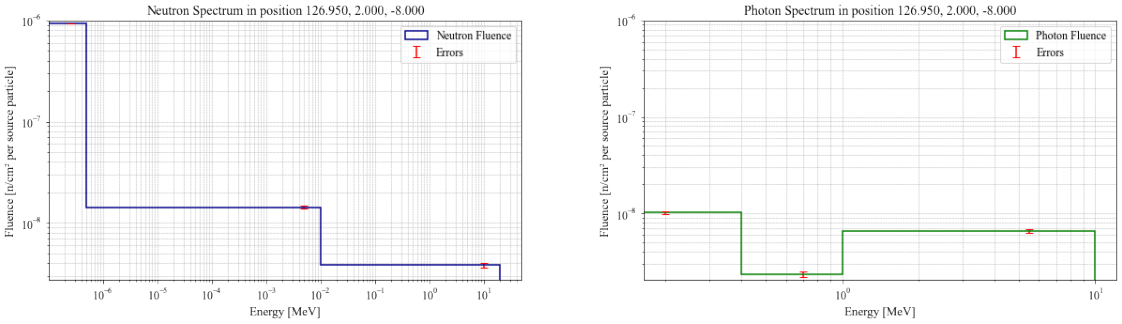

(a) (b)

Figure 2.11: Neutron (a) and photon (b) spectra at the position (226.950, 2.000, -8.000).

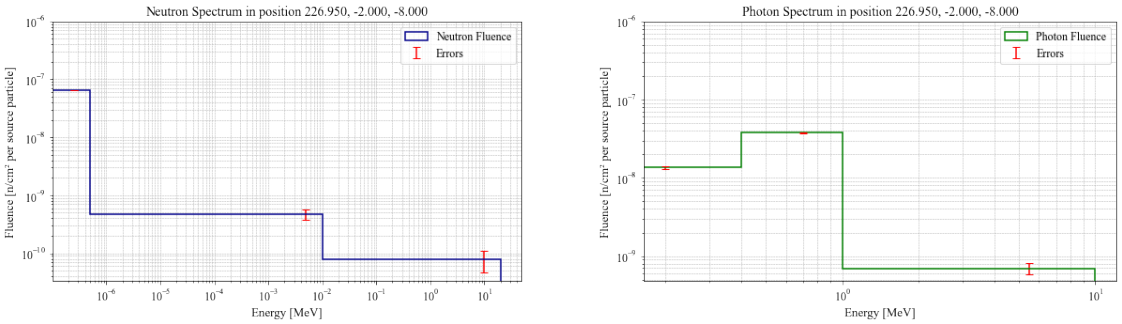

(a) (b)

Figure 2.12: Neutron (a) and photon (b) spectra at the position (126.950, -2.000, -8.000).

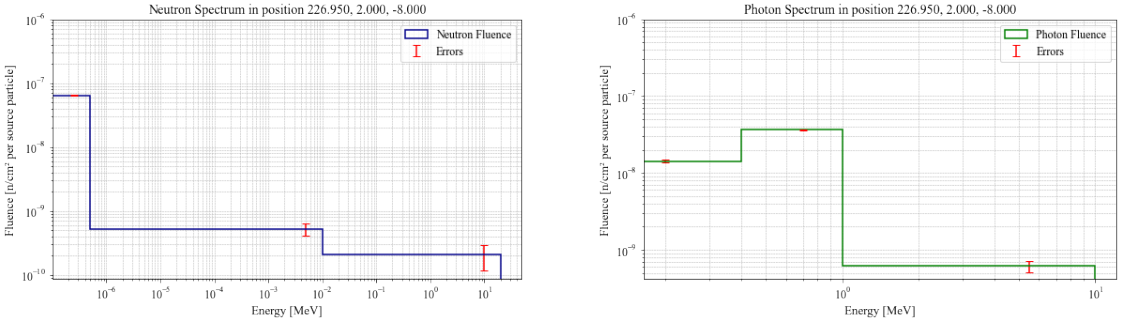

(a) (b)

Figure 2.13: Neutron (a) and photon (b) spectra at the position (126.950, 2.000, -8.000).

The **Material** (Table 2.1) section specifies the compositions and densities of all the used materials. Air, pure silica (SiO_2), polyamide, and acrylate were defined as background or structural materials, while the fiber core was modeled as silica doped with 3 % P_2O_5, representing the P-doped case (the dopant concentration was chosen referring to [50]). The explicit inclusion of dopants is essential, as it allows PHITS to take into account changes in interaction cross sections and energy deposition mechanisms. The elemental compositions of the polymeric materials were taken from previous works as [51] and [52].

Fiber	Silica (Si) [g/cm^3]	Oxygen (O) [g/cm^3]	Dopant [g/cm^3]
P-doped	0.4534	0.5335	0.0130 (P)
Ce-doped	0.4671	0.5321	0.0007 (Ce)
M-OH	0.4675	0.5325	0.0001 (H)

Table 2.1: Concentrations of elements in the core for the three different simulated samples.

The **Cell** and **Surface** (Figure 2.18) sections describe the fiber geometry. The optical fiber model consisted of three concentric cylindrical regions: an inner core (radius 5 μm), a cladding layer

(radius 62.5 µm), and an outer acrylate coating (radius 117 µm). This structure reproduces the typical dimensions of a single optical fiber layer (see Chapter 1). Although the investigated fibers present slight differences in their geometrical dimensions (see for example Table 3.2), the same fiber model was adopted in the simulation. This assumption is justified by the fact that, in the TRIGA TC, the neutron and photon fluence (as shown in the following Table 2.2, 2.3, 2.4, 2.5, 2.6 and 2.7) does not vary significantly across the fiber cross-section. Therefore, small variations in core or coating diameters are not expected to appreciably affect the local energy deposition or the resulting dosimetric response. The fiber was placed in an air cavity, reproducing the irradiation environment inside the TRIGA thermal column, to complete the geometry. A schematic representation of the implemented model is shown in Figure 2.14, 2.15 and 2.16.

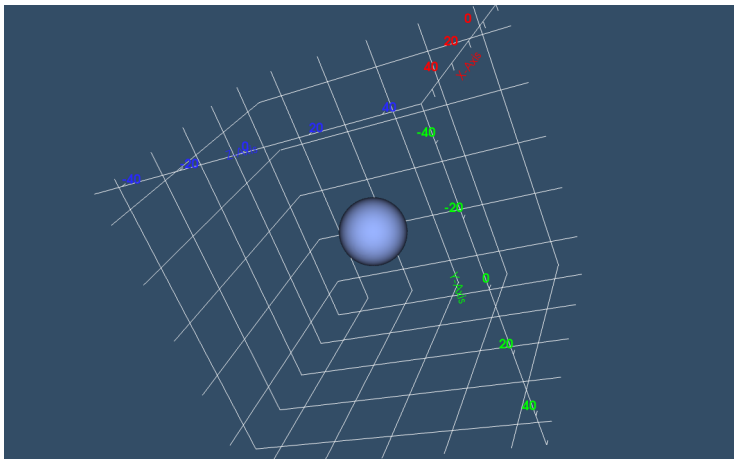

Figure 2.14: PHITS 3D geometry of the outside of the spherical source.

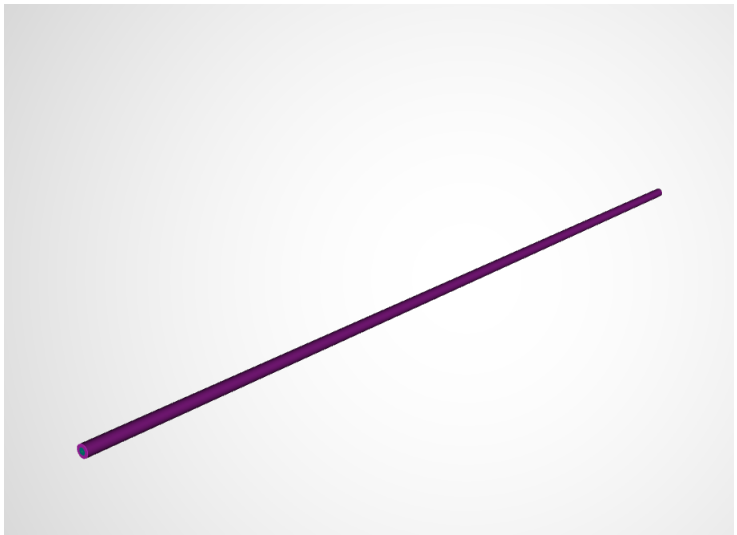

Figure 2.15: View of the PHITS 3D geometry of the optical fiber.

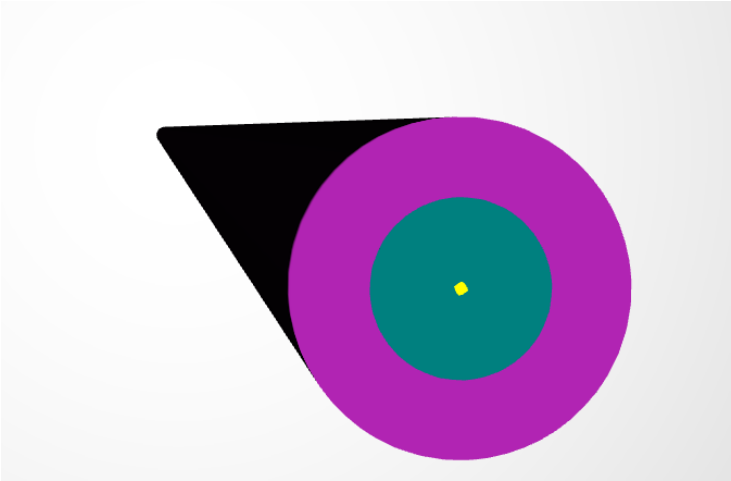

Figure 2.16: PHITS 3D geometry of the optical fiber section. It is possible to distinguish the three different layers: the core in yellow, the cladding in cyan-blue and the coating in magenta.

Similar geometrical approaches have been adopted in previous Monte Carlo studies of optical fiber dosimeters. In [53] the relationship between fluence and dose was simulated in a monolayer fiber model exposed to proton and gamma fields, while in [54] the authors modeled the fiber response to continuous and pulsed X-ray irradiations, reproducing the experimental conditions of the PETRA facility. The material compositions for the polymeric coatings were defined according to the datasets presented in [52]. It is important to emphasize that, unlike the aforementioned studies, which focused on photon or proton irradiation, neutron transport was considered. The present work therefore extends the modeling of optical fiber dosimeters to mixed neutron–photon fields, explicitly including neutron transport in the thermal and epithermal ranges characteristic of the TRIGA thermal column, thereby addressing a gap in the existing literature.

```
[ C e l l ]
1       7 -1            -1 #2 #3 $ coating
2       4 -2.65         -2 #3    $ cladding
3       5 -2.65         -3       $ core P-doped

89      1 -1.225E-3     -90 #1 #2 #3
90      -1              90


[ S u r f a c e ]
1 RCC  -1 0 0   2 0 0   0.0117  $ coating
2 RCC  -1 0 0   2 0 0   0.00625 $ cladding
3 RCC  -1 0 0   2 0 0   0.0005  $ core

90 SO  11
```

Figure 2.17: Definition of cells and surfaces describing the fiber geometry in PHITS. The model consists of three concentric cylindrical regions: coating, cladding, and P-doped core.

The **Importance** block (Figure) was implemented to apply variance reduction, through the definition of importance values for each region, in order to optimize the statistical sampling of particles

within the geometry. Higher importance factors were assigned to the core and cladding regions, where the scoring volumes are located, to increase the number of particle histories contributing to the tallies. In contrast, a lower importance was attributed to the outer regions (coating and air), reducing unnecessary computational processing. This approach improves the simulation efficiency without affecting the physical accuracy of the results.

```
[ I m p o r t a n c e ]
particle= all
reg     imp
1       3   $coating
2       6   $cladding
3       6   $core
89      1
```

Figure 2.18: Part of the PHITS input file showing the `[Importance]` block, where variance reduction is applied through the definition of importance values for each region.

Finally, the **Tally** sections defines the scoring of physical quantities. Several `T-track` (Figure 2.19) tallies were used to calculate particle fluence.

```
[T - t r a c k ]
    title = Fluence
     mesh = reg
     reg  = 1 2 3

     part = all
   e-type =    1            # e-mesh is given by the below data
       ne =    1            # number of e-mesh points
            0.0  10000

     unit =    1            # unit is [1/cm^2/source]
     axis =   reg           # axis of output
     file =  Fluence_P_doped_pos_1_1_photon.out # file name of output for the above axis
```

Figure 2.19: Example of a `[T-track]` tally block used to score particle fluence. Here the fluence is recorded per region, with results expressed in units of 1/cm^2/source.

To complement the tally results for integrated quantities, two-dimensional mesh tallies were implemented to visualize the spatial distribution of fluence and energy deposition within the fiber cross section. Figures 2.20 and 2.21 respectively show the fluence and dose distributions obtained in the xz plane crossing the fiber model in the case of neutrons. The `T-track` mesh provides a map of particle fluence [cm^{-2} per source particle], which exhibits a nearly uniform distribution in the air region and a sharp attenuation within the dense silica layers. Conversely, the `T-dep` mesh illustrates the local energy deposition [MeV g^{-1} per source particle], clearly concentrated within the fiber core where most of the photon interactions occur. This spatial analysis confirms that the microscopic geometry of the fiber strongly influences the local dose gradient and supports the need for accurate transport modeling at the micrometric scale.

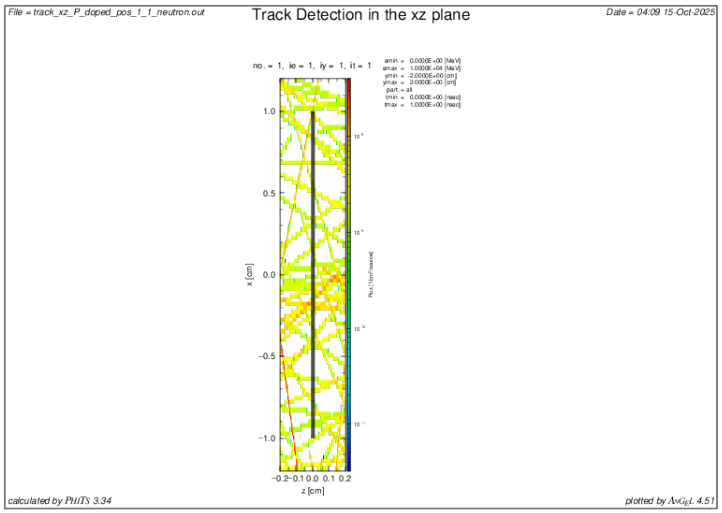

Figure 2.20: Two-dimensional mesh tally (`T-track`) showing the neutron fluence distribution in the xz plane at the considered position. The color scale represents the fluence [cm^{-2} per source particle].

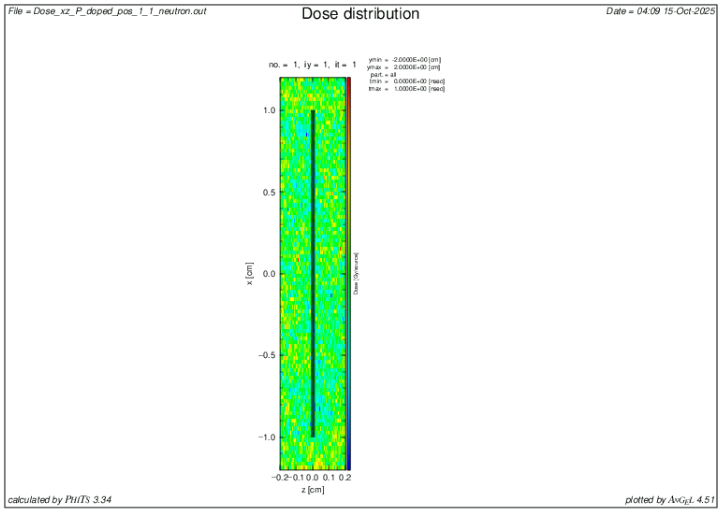

Figure 2.21: Two-dimensional mesh tally (`T-dep`) showing the spatial distribution of neutron energy deposition in the xz plane at the considered position. The color scale represents the deposited energy [MeV g^{-1} per source particle].

In addition, `T-deposit` (Figure 2.22) tallies were implemented to estimate the absorbed dose, both as spatial maps (to visualize possible gradients across the fiber cross-section) and as mean values in the core, cladding, and coating. This redundancy provided internal consistency checks

and ensured the reliability of the results.

```
[ T - D e p o s i t  ]
   title = Dose

    mesh = reg
    reg  = 1 2 3

    part = all
    unit =    0           # unit is [Gy/source]
    axis =   reg          # axis of output
    file =  Dose_P_doped_pos_1_1_photon.out # file name of output for the above axis
```

Figure 2.22: Example of a `[T-deposit]` tally block used to score the absorbed dose. Here the dose is calculated per region (core, cladding, coating) and expressed in units of Gy/source.

The tree representative fiber types considered in this study are, as previously mentioned, P-doped, Ce-doped, and medium-OH pure silica core (M-OH), as they exhibit mechanisms of radiation response relevant to dosimetric applications. The P-doped fibers are characterized by a high concentration of defect precursors leading to strong RIA, and are thus representative of transmission-based dosimetry systems. Ce-doped fibers, conversely, emit intense RIL and enable real-time optical detection of dose, while M-OH fibers are used as transport fibers in both the performed experiments.

The described geometry model was replicated for all fiber considered in this work for the four selected positions in the CT. By following this scheme, a set of simulations was performed to compare the dose absorbed in different fibers placed in the mixed field of the TC.

The difference in the code between the three fibers tested resides in the **Material** section and is reported in the case of M-OH fiber in Fig. **??** and for the Ce-doped in Fig. **??**.

2.2.3 Simulation Results

To analyze the Monte Carlo results, we first discuss one representative irradiation point for both neutrons and photons for all the sample fibers and then extend the comparison to the other positions.

The selected position has coordinates (126.950, - 2.000, - 8.000), placed next to position 1 in 2.7 and corresponds to the neutron and photon spectra presented in Figure 2.10. The reference fiber for this discussion is the P-doped sample. It was modeled as a cylindrical segment of 3 cm in length, composed of three concentric regions: the P-doped silica core (radius 5 µm), the pure-silica cladding (radius 62.5 µm), and the acrylate coating (radius 117 µm). The output files include: (i) absorbed dose in the different fiber regions; (ii) the spatial distribution of the deposited energy, represented as a two-dimensional map in the longitudinal (xz) plane crossing the fiber axis, together with the corresponding statistical error map; (iii) fluence; (iv) track-length map on the xz plane and its error map.

The results of the simulations are summarized in Table 2.2 for neutrons and in Table 2.3 for photons. They provide a quantitative comparison between the neutrons and photons contribution to the total dose and fluence in the three different regions of the P-doped geometry.

Region	Volume [cm^3]	Fluence [1/cm^2/source]	Fluence RE %	Dose [Gy/source]	Dose RE %
Coating	$6.1467 \cdot 10^{-4}$	$3.1806 \cdot 10^{-3}$	0.12	$3.2531 \cdot 10^{-15}$	0.70
Cladding	$2.4384 \cdot 10^{-4}$	$3.1769 \cdot 10^{-3}$	0.17	$6.8659 \cdot 10^{-16}$	1.67
Core	$1.6000 \cdot 10^{-6}$	$3.1374 \cdot 10^{-3}$	0.58	$7.1320 \cdot 10^{-16}$	6.01

Table 2.2: Results obtained for the fluence and dose, with the respective relative errors (RE), in the three regions of the fiber geometry (coating, cladding, core) for **neutron** irradiation in the case of the **P-doped** fiber.

For neutron irradiation, the fluence values are nearly uniform across the layers, indicating that the low-energy neutron field inside the TC is spatially homogeneous at the micrometric scale. Instead, the corresponding absorbed dose exhibits more pronounced variations, with the dose value decreasing going from the coating towards the core. This reflects the different material compositions and geometrical locations of the regions. The most of the energy deposition takes place in the hydrogen-rich coating through neutron moderation and recoil interactions, while the core is characterized by a lower energy transfer. While in fast or epithermal neutron fields the main hydrogen-related contribution to the absorbed dose originates from elastic n-H scattering producing recoil protons, in a thermal spectrum the predominant process is the radiative capture reaction ^{1}H(n,γ)^{2}H, which emits 2.2 MeV photons. These photons constitute a non-negligible source of background dose in BNCT but, given the small thickness of the optical fiber, their interaction probability within the silica matrix can be considered negligible for dosimetric purposes.

For what concerns the relative uncertainties they are below or close to the value of 5%, required to guarantee statistical reliability. The larger error observed in the core region arises from the significantly smaller scoring volume, which reduces the number of sampled particle interactions.

Region	Volume [cm^3]	Fluence [1/cm^2/source]	Fluence RE %	Dose [Gy/source]	Dose RE %
Coating	$6.1467 \cdot 10^{-4}$	$3.1875 \cdot 10^{-3}$	0.10	$2.6698 \cdot 10^{-15}$	1.67
Cladding	$2.4384 \cdot 10^{-4}$	$3.1852 \cdot 10^{-3}$	0.13	$2.9841 \cdot 10^{-15}$	1.53
Core	$1.6000 \cdot 10^{-6}$	$3.1338 \cdot 10^{-3}$	0.47	$3.3838 \cdot 10^{-15}$	5.22

Table 2.3: Results obtained for the fluence and dose, with the respective relative errors (RE), in the three regions of the fiber geometry (coating, cladding, core) for **photon** irradiation in the case of the **P-doped** fiber.

For the photon case, it is possible to see how both fluence and dose distributions appear more uniform across the three regions. Photon transport in this energy range is governed by Compton scattering, which depends weakly on atomic composition. Also in this case coating and cladding show nearly identical fluence and comparable dose values. The core records a lower dose, consistent with its smaller volume.

The relative errors, also in this case, are below or close to the required 5%, ensuring statistical validity of the results.

These considerations are visually summarized in Table 2.23 and 2.24. In addition, these results are consistent with what has been observed in similar studies, such as in [52]. In this work, even if the radiation field was different, it was observed, through PHITS simulations, the different deposition in the different components of optical fibers (core, cladding and coating) irradiated in the mixed neutron-photon field of the n_TOF NEAR station at CERN. The outcomes highlighted for photons that the absorbed dose remains approximately constant within the three fiber layers, while for neutrons it changes depending on the layer composition and it is dominant in hydrogen-containing materials, accordingly to what showed in the present work.

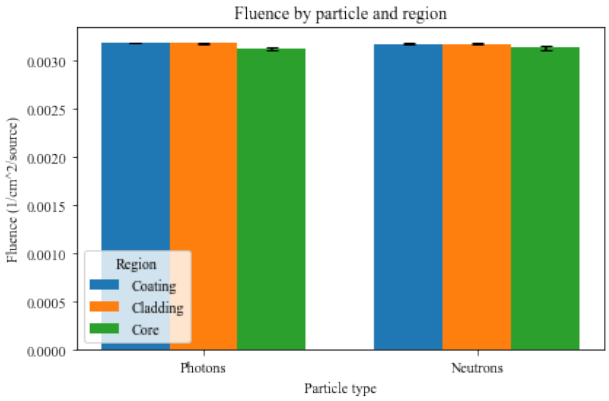

Figure 2.23: Comparison of **fluence** for photons and neutrons across the three fiber components (coating, cladding, core) of a **P-doped** fiber. The error bars correspond to the statistical errors.

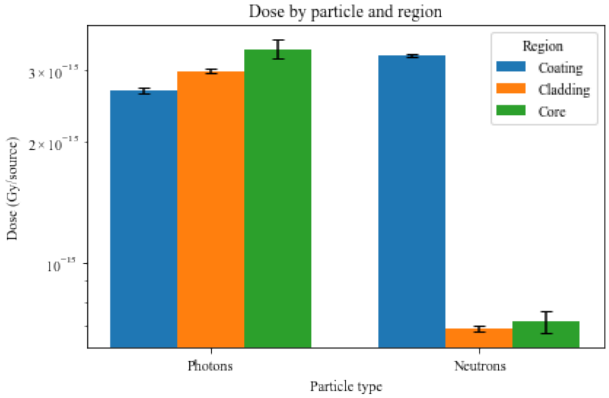

Figure 2.24: Comparison of mean **dose** for photons and neutrons in the three regions of **P-doped**. The error bars correspond to the statistical errors. Y-axis in logarithmic scale.

The results concerning the M-OH fiber, which is the transport fiber used in all the experiments and also a sample for some of them, at the same position inside the TC are collected in the case of neutrons in Table 2.4 and for photons in Table 2.5.

Region	Volume [cm^3]	Fluence [1/cm^2/source]	Fluence RE %	Dose [Gy/source]	Dose RE %s
Coating	$6.1467 \cdot 10^{-4}$	$3.1824 \cdot 10^{-3}$	0.09	$3.2600 \cdot 10^{-15}$	0.53
Cladding	$2.4384 \cdot 10^{-4}$	$3.1793 \cdot 10^{-3}$	0.13	$6.8638 \cdot 10^{-16}$	1.28
Core	$1.6000 \cdot 10^{-6}$	$3.1287 \cdot 10^{-3}$	0.45	$6.9509 \cdot 10^{-16}$	4.49

Table 2.4: Results obtained for the fluence and dose, with the respective relative errors (RE), in the three regions of the fiber geometry (coating, cladding, core) for **neutron** irradiation in the case of the **M-OH** fiber.

Region	Volume [cm^3]	Fluence [1/cm^2/source]	Fluence RE %	Dose [Gy/source]	Dose RE %
Coating	$6.1467 \cdot 10^{-4}$	$3.1891 \cdot 10^{-3}$	0.06	$2.6557 \cdot 10^{-15}$	1.04
Cladding	$2.4384 \cdot 10^{-4}$	$3.1888 \cdot 10^{-3}$	0.08	$3.0340 \cdot 10^{-15}$	0.97
Core	$1.6000 \cdot 10^{-6}$	$3.1410 \cdot 10^{-3}$	0.29	$3.3705 \cdot 10^{-15}$	3.35

Table 2.5: Results obtained for the fluence and dose, with the respective relative errors (RE), in the three regions of the fiber geometry (coating, cladding, core) for **photon** irradiation in the case of the **M-OH** fiber.

As for the P-doped fiber, the simulated fluence is essentially uniform across regions for both neutrons and photons, with deviations well within the uncertainties. A similar behaviour is observed for the dose. Under neutron irradiation, the energy deposition is dominated by n-H elastic scattering in the hydrogen-rich polymer coating, which contains several atomic percent of hydrogen and therefore acts as the main site of neutron energy transfer through recoil protons. In contrast, the silica core shows neutron dose values compatible within their uncertainties, indicating that the detailed core composition does not significantly influence the neutron response. This behaviour is consistent also in the M-OH case, where the very low concentration of hydroxyl impurities, typically of the order of ppm, is insufficient to appreciably modify the interaction probability. Under photon irradiation, the fibers exhibit similar behaviour, with modest variations among regions and a slightly lower dose in the core.

These trends are summarized in Figs. 2.25 and 2.26.

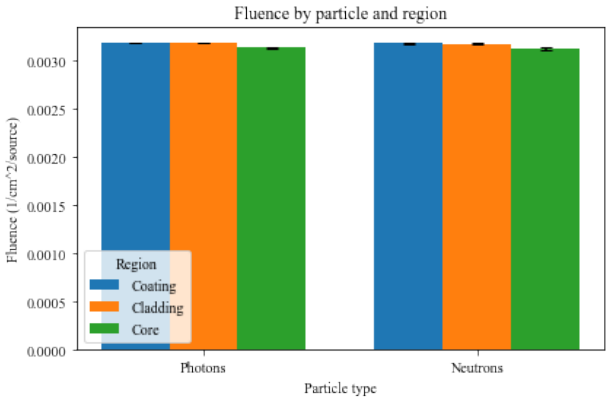

Figure 2.25: Comparison of mean **fluence** for photons and neutrons across the three fiber regions (coating, cladding, core) of a **M-OH** fiber. The error bars correspond to the statistical errors.

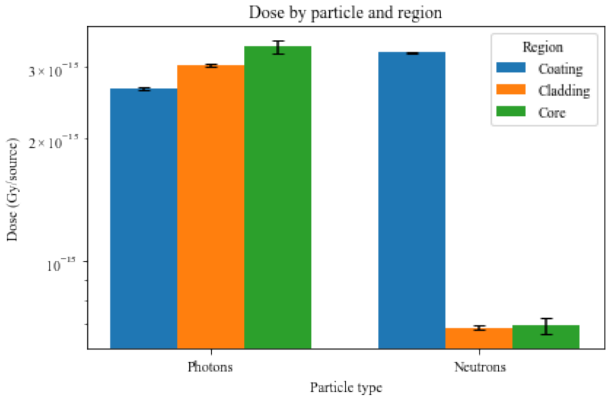

Figure 2.26: Comparison of mean **dose** for photons and neutrons in the three regions of **M-OH**. The error bars correspond to the statistical errors. Y-axis in logarithmic scale.

Finally, the Ce-doped fiber at the same position shows the results gathered in Table 2.6 (neutrons) and Table 2.7 (photons). The data are compared in Figure 2.27 and Figure 2.28.

Region	Volume [cm^3]	Fluence [1/cm^2/source]	Fluence RE %	Dose [Gy/source]	Dose RE %s
Coating	$6.1467 \cdot 10^{-4}$	$3.1806 \cdot 10^{-3}$	0.08	$3.2597 \cdot 10^{-15}$	0.47
Cladding	$2.4384 \cdot 10^{-4}$	$3.1785 \cdot 10^{-3}$	0.11	$6.8888 \cdot 10^{-16}$	1.12
Core	$1.6000 \cdot 10^{-6}$	$3.1242 \cdot 10^{-3}$	0.38	$6.7690 \cdot 10^{-16}$	4.55

Table 2.6: Results obtained for the fluence and dose, with the respective relative errors (RE), in the three regions of the fiber geometry (coating, cladding, core) for **neutron** irradiation in the case of the **Ce-doped** fiber.

Region	Volume [cm^3]	Fluence [$1/cm^2$/source]	Fluence RE %	Dose [Gy/source]	Dose RE %
Coating	$6.1467 \cdot 10^{-4}$	$3.1891 \cdot 10^{-3}$	0.05	$2.6547 \cdot 10^{-15}$	1.04
Cladding	$2.4384 \cdot 10^{-4}$	$3.1888 \cdot 10^{-3}$	0.08	$3.0331 \cdot 10^{-15}$	0.97
Core	$1.6000 \cdot 10^{-6}$	$3.1410 \cdot 10^{-3}$	0.29	$3.3955 \cdot 10^{-15}$	3.38

Table 2.7: Results obtained for the fluence and dose, with the respective relative errors (RE), in the three regions of the fiber geometry (coating, cladding, core) for **photon** irradiation in the case of the **Ce-doped** fiber.

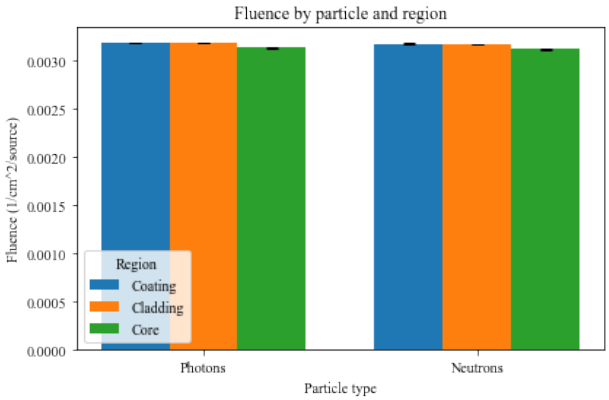

Figure 2.27: Comparison of mean **fluence** for photons and neutrons across the three fiber regions (coating, cladding, core) of a **Ce-doped** fiber. The error bars correspond to the statistical errors.

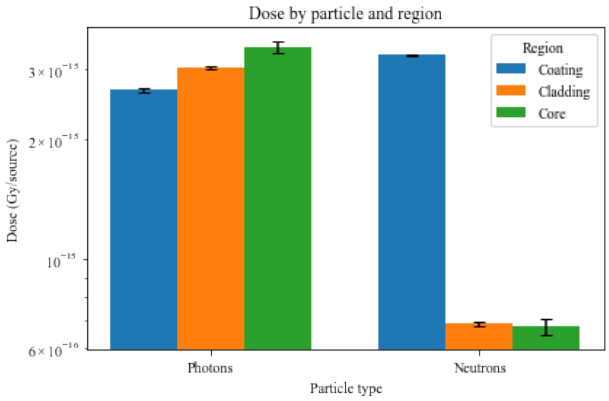

Figure 2.28: Comparison of mean **dose** for photons and neutrons in the three regions of **Ce-doped**. The error bars correspond to the statistical errors. Y-axis in logarithmic scale.

The same considerations previously done for the other two optical fibers apply to the Ce-doped fiber. Hence, within uncertainties, the detailed core composition (P-doped, M-OH, Ce-doped) does not appreciably affect dosimetry, while significant differences are observed between neutron

dose components in the coating, made of organic H-rich material, and core and cladding, mostly made of silica and whose composition differ by small concentrations at the ppm scale only. These results are in agreement with previous Monte Carlo studies in which the irradiation of optical fiber geometries in different neutron and gamma mixed field is simulated.

For this specific type of fiber simulations were performed also eliminating the coating layer, according to the fact that, as subsequently shown in Chapter 3, for RIL experiments usually the sample is used stripped of its coating. The results obtained in case of neutron and photon irradiations are reported respectively in Table 2.8 and 2.9.

Region	Volume [cm^3]	Fluence [1/cm^2/source]	Fluence RE %	Dose [Gy/source]	Dose RE %
Cladding	$2.4384 \cdot 10^{-4}$	$3.1781 \cdot 10^{-3}$	0.13	$6.8793 \cdot 10^{-16}$	1.26
Core	$1.6000 \cdot 10^{-6}$	$3.1247 \cdot 10^{-3}$	0.44	$6.9159 \cdot 10^{-16}$	4.42

Table 2.8: Results obtained for the fluence and dose, with the respective relative errors (RE), in the two regions of the fiber geometry (cladding and core) for **neutron** irradiation in the case of the **Ce-doped** fiber.

Region	Volume [cm^3]	Fluence [1/cm^2/source]	Fluence RE %	Dose [Gy/source]	Dose RE %
Cladding	$2.4384 \cdot 10^{-4}$	$3.1876 \cdot 10^{-3}$	0.08	$2.5198 \cdot 10^{-15}$	1.17
Core	$1.6000 \cdot 10^{-6}$	$3.1404 \cdot 10^{-3}$	0.29	$3.0030 \cdot 10^{-15}$	3.68

Table 2.9: Results obtained for the fluence and dose, with the respective relative errors (RE), in the two regions of the fiber geometry (cladding and core) for **photon** irradiation in the case of the **Ce-doped** fiber.

Comparing the Ce-doped fiber without the polymer coating (Table 2.8 and 2.9) with the corresponding coated case (Table 2.6 and 2.7), we observe that in a thermal neutron spectrum the removal of the coating produces negligible changes in the fluence and dose within the silica regions (core and cladding), well within the statistical uncertainties. This is consistent with the fact that, at thermal energies, the dominant hydrogen-related process is ^{1}H(n,γ)^{2}H and the emitted 2.2 MeV photons have a low interaction probability over micrometric path lengths in silica. For photons, moderate variations (typically $\sim$10-20%) appear in core and cladding when the coating is removed, which can be ascribed to changes in electron build-up and, more generally, to the lack of strict CPE at micrometric scale across the fiber interfaces. Importantly, the order of magnitude and the relative hierarchy of the dose contributions remain unchanged. Since our results are based on deposited-energy tallies, no CPE assumption is required and the observed trends directly reflect the transport of secondary particles in the actual geometry.

While for BNCT, experiments at the TRIGA facility, with the simulations presented above, will provide the proof that optical fiber dosimetry can be an online monitor in mixed neutron–photon fields, additional experimental tests are needed to assess fiber performance under controlled photon irradiation for other medical applications, such as FLASH radiotherapy. For this reason, the

next chapter presents the PETRA X-ray facility and the experimental campaigns performed to benchmark the fiber response, before extending the study to FLASH radiotherapy conditions.

Chapter 3

X-ray Irradiation Experiments at PETRA platform

Following the simulation studies at the TRIGA reactor, the experimental characterization of optical fibers was conducted at the PETRA X-ray platform. These photon irradiation experiments served as a benchmark to reproduce dose rates comparable to those expected in the thermal column, obtained from previous studies (see Figures 2.10, 2.11, 2.12 and 2.13), and to explore the potential extension of fiber dosimetry to FLASH radiotherapy.

In addition, an original contribution, based on this research activity, has been submitted for publication to *physica status solidi (a)* in September 2025 [55]. This work concerns M-OH fibers and the dedicated pulsed-beam setup developed to investigate their response. The focus of this latter work is on pulsed radiation fields, such as the ones we have in FLASH therapy, and while it does not directly reproduce the thermal column environment, it offers complementary insights into the behaviour of optical fibers under extreme dose-rate conditions for medical applications.

3.1 PETRA X-ray irradiation platform

The PETRA X-ray irradiation platform includes three commercial X-ray tubes, which allows tests on optical fibers [56] [57] and materials [58] [59], across a wide temperature range, from - 120 °C to + 400 °C, in laboratory standard atmospheric conditions. The available equipment encompasses [60]. Of the three irradiators, the two used in the experiments of the present work are the LabHX and the MOPERiX facilities. The main specifics, common to both, are reported in Table 3.1 and two pictures are respectively reported in Figure 3.1 and 3.2.

Characteristic	Details
Maximum Voltage	225 kV (160 kV)
Maximum Current	30 mA (45 mA)
Target Material	Tungsten (W)
Anode Angle	30°
Tube Filtration	2 mm of Beryllium (Be)
Maximum Tube-Sample Distance	$\sim$ 1.5 m

Table 3.1: Main characteristics of the X-ray facilities at Hubert Curien Laboratory, Saint-Etienne, France [60].

Figure 3.1: Picture of the LabHX facility at Hubert Curien Laboratory.

These features make the PETRA facility particularly suitable for dosimetry studies. The X-ray fields are generated by an electron beam impinging on a metallic target, producing photons mainly through bremsstrahlung radiation and, to a lower extent, by characteristic X-ray emission. By adjusting the acceleration voltage of the tube, the maximum photon energy and the spectral distribution can be tuned, while variations of the tube current directly control the photon flux and therefore the dose rate. Moreover, the dose rate can be easily varied by several orders of magnitude not only through the current setting but also by changing the sample position with respect to the source, thanks to the large accessible range of distances in the irradiation cell.

Figure 3.2: Picture of the MOPERiX facility at Hubert Curien Laboratory.

In this work, the X-ray fields of PETRA were used as a reference environment to test optical fiber dosimeters, providing a well-defined and tunable photon field prior to their investigation in mixed neutron–photon environments such as the one at the TRIGA reactor. The selection of beam parameters (voltage, current, and exposure time) thus enables exploration of the fiber response under different total doses, dose rates, and spectral conditions, laying the experimental groundwork for subsequent analysis.

The experiments serve a dual purpose: on one hand, they allow us to calibrate and benchmark the response of the fibers against well-characterized reference conditions; on the other hand, they can provide insights into the feasibility and limitations of fiber-based dosimetry in reactor irradiation scenarios.

In particular, two dosimetric techniques previously introduced in Chapter 1 were investigated: RIL, suitable for real-time dose-rate monitoring, and RIA, which provides a real-time cumulative measure of the absorbed dose. The complementary nature of these approaches makes it possible to assess different potential applications inside the TRIGA TC. From the Monte Carlo simulations performed with the TC fields (see Chapter 2), the photon and neutron dose rates in the central irradiation positions were estimated to be of the order of a few tens of $\mathrm{mGy \cdot s^{-1}}$, corresponding to cumulative doses ranging from a few gray up to several hundred gray for irradiation times between a few minutes and many hours, which are typical durations for BNCT treatments. These values can be directly compared with the sensitivity ranges obtained experimentally at PETRA: the RIA-based P-doped fiber shows a linear and stable response up to several hundred Gy,

making it suitable for integrated dose mapping over extended irradiation periods, while the RIL-based fibers provide real-time dose-rate measurements in the mGy·s^{-1} range, which matches the instantaneous dose-rate conditions predicted in the TC. Therefore, combining RIA and RIL detection allows both cumulative and real-time dosimetry within the same radiation environment, addressing the different operational needs expected in the TRIGA facility.

The following sections present the results of these experimental campaigns, highlighting both methodological aspects and their relevance for future deployment of optical fiber dosimeters in BNCT and, more broadly, in non-conventional radiotherapy contexts.

3.2 RIL Measurement

The methods and results presented in this section are part of the work published and currently under revision for the article "Radiation-Induced Luminescence of a Medium-OH Pure Silica Core Multimode Optical Fiber in Steady-State and Pulsed X-ray Irradiations: Potential and Limitations for Dosimetry", by L. Breccia *et al.*, submitted to *Physica Status Solidi (a)* in September 2025 [55].

3.2.1 Materials and Methods

The experimental campaign was devoted to the characterization of the RIL response of the Ce-doped and M-OH optical fibers under continuous X-ray exposure. The former are known to exhibit strong RIL around 500 nm under radiation exposure. For this reason they are among the candidates for radiation RIL-based monitoring [7] [61]. In this campaign this fiber was considered as reference. M-OH is a multimode optical fiber with pure silica core, fluorine-doped cladding and polymide coating, manufactured by Exail [62]. The term "medium" refers to the intermediate concentration of hydroxyl groups, compared to the existing high and low-OH optical fibers. M-OH fibers have been employed as transport fibers in RIL experiments [57], because of their low RIA in the visible range. Information about both the samples is reported in Table 3.2.

Sample	Core Diameter	Cladding Diameter	Coating Diameter
M-OH	112 μm	125 μm	150 μm
Ce-doped	110 μm (50 μm doped with Ce)	126 μm	242 μm

Table 3.2: Geometrical characteristics of the investigated optical fibers.

Irradiation experiments were performed with the X-ray tube operated at 100 kV (standard value, see for example [61] and [63]). Eight different dose rates were tested by adjusting the tube current: 0.3, 0.6, 2.3, 6.0, 29.9, 59.9, 89.9 and 179.7 mGy(SiO_2)/s. The dose rate was experimentally determined using a calibrated ionization chamber placed at the irradiation position. The chamber readings, originally expressed as absorbed dose in water, were converted into the corresponding absorbed dose in silica (SiO_2) by applying a conversion factor of 2.5 [55]. For the short Ce-doped sample (2 cm in length), a single readout centered on the sample was sufficient to characterize the delivered dose. In contrast, for the longer M-OH spooled fibers, four measurements were

performed at different positions along the coil and averaged to account for possible field inhomogeneities. The maximum variation among these positions was below 1.6%, confirming the uniformity of the irradiation field across the entire fiber length.

RIL was detected with a photomultiplier tube (PMT) connected to the irradiated fiber through a M-OH transport fiber. The transport fiber (as schematically representated in Figure 3.3) was shielded with ∼3 mm of lead to minimize parasitic contributions, such as luminescence induced in the transport line.

PMT signals were recorded as counts per second (cps) with a gate time of 1 s. Background signals were acquired in dark conditions and subtracted from the measurements.

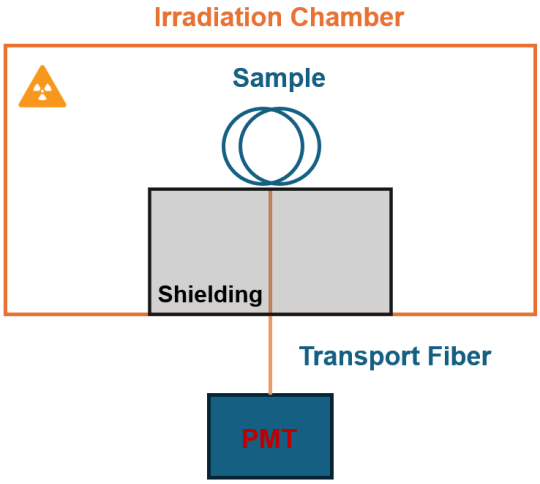

Figure 3.3: Schematic of the setup used in the first campaign.

Two samples were tested:

- a 2 cm Ce-doped fiber, stripped of its coating;
- a 391.5 cm M-OH fiber (simply referred to as M-OH 4m), spooled with an internal radius of 2.5 cm (Figure 3.4).

The choice of employing a monolayer spool was made to ensure a sufficiently homogeneous irradiation of 4 m of optical fiber in both the vertical and horizontal directions.

Additional measurements were performed on a shortened M-OH fiber of 290.5 cm (M-OH 3m) in order to evaluate the length dependence for the M-OH fiber.

Finally, a systematic study was carried out with M-OH fiber lengths ranging between 59 and 190.5 cm, irradiated at a fixed dose rate of 89.5 mGy(SiO_2)/s, to investigate the linearity of sensitivity with fiber length.

3.2.2 Results and Discussion

Figure 3.5 reports the RIL kinetics for both samples during a sequence of irradiation steps at increasing dose rates (each step corresponds to a dose rate value). In both cases, the luminescence

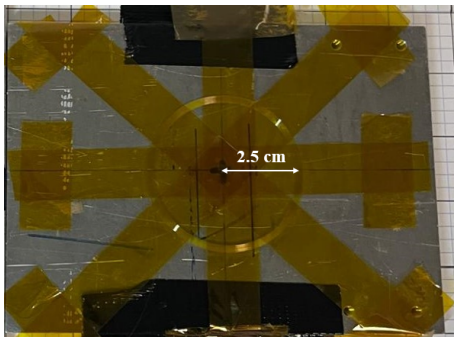

Figure 3.4: Photograph of the M-OH fiber (4 m) arranged in a spool with 2.5 cm internal radius.

increases with dose rate when the beam is switched ON (plateau of the step) and decreases when the beam is switched OFF. This well-known response is used for the construction of RIL-based optical fiber dosimeters for dose rate measurement. However, a significant difference emerges in the relaxation kinetics of the two fibers: the M-OH fiber rapidly returns to the background level, while the Ce-doped fiber exhibits a slower signal decay when the irradiation turns OFF, resulting in a pronounced afterglow. The faster recovery of the M-OH fiber could represent a promising feature for dosimetry in scenarios where fast stabilization or afterglow is required.

However, it is important to note that, in this experiment, the two samples have very different length (2 cm for the Ce-doped and almost 4 m for the M-OH). Therefore, the absolute RIL values cannot be directly compared. The experiment focuses on a comparison between the two fibers for what concerns transient behaviors and the measurement of parasitic effects such as afterglow.

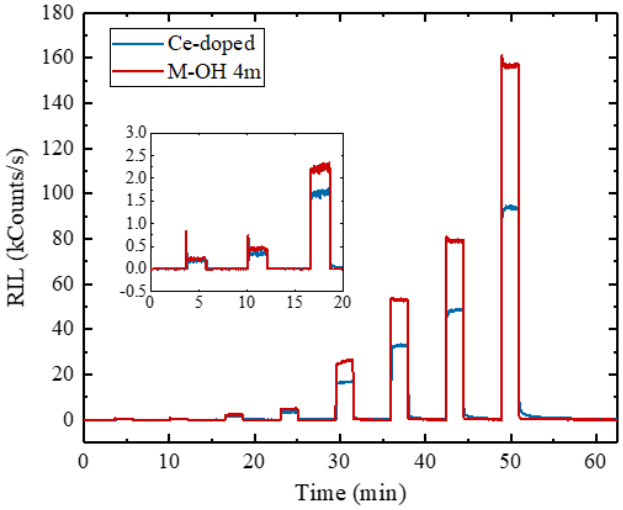

Figure 3.5: RIL kinetics for the Ce-doped fiber (blue) and the 4 m M-OH fiber (red) as a function of irradiation times. The Ce-doped sample shows a marked afterglow once the beam is switched off, while the M-OH fiber more rapidly returns to the background level. The inset highlights the behaviour at the three lowest dose-rate conditions. Acknowledgments Breccia et al. [55].

The RIL as a function of dose rate is shown in Figure 3.6. As expected, M-OH samples of both lengths exhibit a linear RIL dependence on the dose rate across the entire explored range (0.3–179.7 mGy(SiO_2)/s). This linearity is a desired prerequisite for this promising RIL-based dosimeter [8]. The higher absolute signal recorded from the M-OH samples compared to the 2 cm Ce-doped fiber reflects the different sample lengths and does not correspond to a higher intrinsic sensitivity.

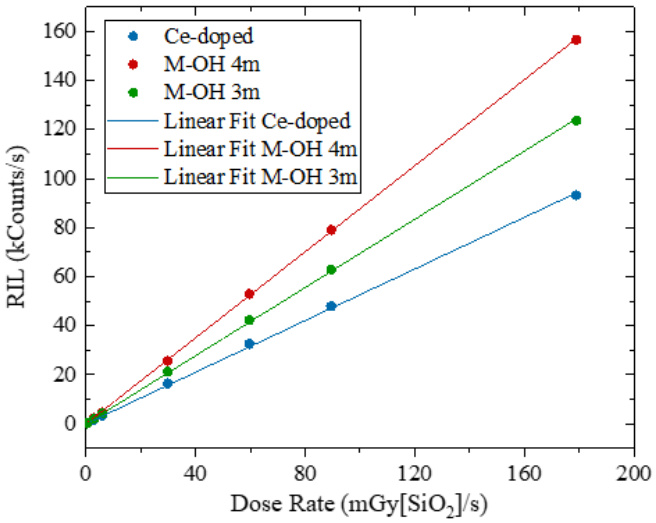

Figure 3.6: RIL signal as a function of dose rate for the Ce-doped (2 cm) and the M-OH fibers of 3 m and 4 m length. Both M-OH samples show a clear linear dependence across the entire investigated range, confirming their suitability for quantitative dosimetry. The parameters of the fit for the red line are: slope = 876.95 kCounts/mGy[SiO_2] and R^2 = 0.999. For the green one: slope = 694.78 kCounts/mGy[SiO_2] and R^2 = 0.999. Finally for the blue: slope = 526.19 kCounts/mGy[SiO_2] and R^2 = 0.999. The higher absolute signal of the M-OH fibers is mainly due to their longer length.

Figure 3.7 shows the sensitivity of the M-OH fiber, expressed in counts per second per unit dose rate, as a function of fiber length. The results show a linear trend (slope = 2.29 cps·mGy^{-1}·cm^{-1}, R^2 = 0.998), allowing the sensitivity of the fiber to be tuned by simply adjusting the fiber length. For comparison, the 2 cm Ce-doped sample (represented by a blue dot in the picture) exhibits a sensitivity of 526.2 cps/mGy, which, when normalized by length, remains significantly higher than that of the M-OH fiber due to the intrinsic efficiency of Cerium doping. Extrapolation of the linear trend suggests that M-OH fibers longer than ∼230 cm can reach signal levels comparable to those of short Ce-doped probes.

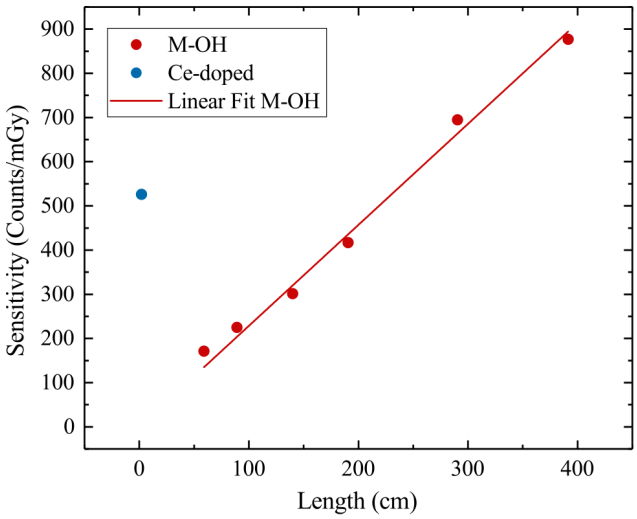

Figure 3.7: Sensitivity of the M-OH fiber as a function of fiber length at a fixed dose rate of 89.5 mGy(SiO_2)/s. The blue dot represents the 2 cm Ce-doped sample, which exhibits much higher intrinsic efficiency per unit length.

These results highlight the flexibility of M-OH fibers: by properly choosing the length, the sensitivity can be tuned across a wide dynamic range while preserving linearity. Moreover, their reduced afterglow compared to Ce-doped fibers represents a clear advantage for applications requiring rapid recovery and minimal memory effects. Although the present measurements already demonstrate tunable sensitivity, the upper limit of the usable dynamic range has not yet been reached. Future experiments involving longer fiber lengths need to be carried out to identify the onset of radiation-induced attenuation effects that may impact the transmitted signal and limit the overall linearity.

The encouraging performance of the M-OH and Ce-doped fibers confirms the suitability of RIL-based systems for real-time dose-rate monitoring in photon fields. Beyond the specific experimental conditions tested here, RIL dosimeters represent a promising solution for applications in mixed radiation fields, such as neutron–photon environments encountered in research reactors or accelerator facilities. In these conditions, the rapid and purely optical response of RIL sensors makes them well suited for operation in harsh or mixed radiation fields, where the use of conventional electronic detectors may be challenging.

3.3 RIA Measurement

3.3.1 Materials and Methods

The fiber investigated in this campaign is a single-mode phosphosilicate (P-doped) optical fiber. The fiber has an acrylate coating and is characterized by a high sensitivity to radiation due to the

presence of phosphorus-related point defects, in particular the P_1 center, which exhibits an absorption band peaked around 1570 nm. This band is thermally stable and spectrally well aligned with the probing wavelength of standard OTDR systems (1550 nm), making P-doped silica fibers intrinsically suitable for distributed radiation dosimetry [50]. Fluorine is also introduced in the cladding to tailor light guiding properties, while residual chlorine impurities from the fabrication process remain at low levels ($\sim$0.2%).

For these irradiations, the X-ray tube current was set to 12 mA, corresponding to a dose rate of 1 Gy(SiO_2)/s at the irradiation position. The sample was irradiated up to a total absorbed dose of 375 Gy. The fiber, 20 m in length, was arranged in a monolayer coil with a 2.5 cm of internal radius to ensure uniform exposure. The irradiation setup is reported schematically in Figure 3.8, while photographs of the irradiator and of the spooled fiber are shown in Figures 3.10 and 3.9, respectively. This specific combination of dose and dose rate was selected to reproduce, under controlled X-ray conditions, the magnitude of cumulative doses and instantaneous dose rates similar to the expected ones in the TRIGA TC. Although the radiation fields differ in nature, this configuration allows assessing the feasibility of RIA-based measurements for reactor environments, verifying the fiber stability and linearity over the dose levels relevant for potential in-core dosimetry experiments.

Distributed measurements were acquired with a VIAVI/JDSU OTDR operating at 1550 nm. The selected configuration employed a pulse width of 5 ns and an integration time of 4 s.

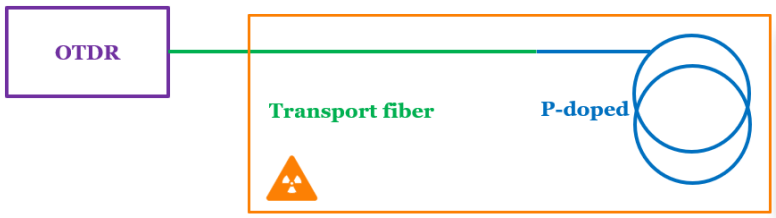

Figure 3.8: Schematic layout of the RIA experimental setup. A single-mode P-doped fiber was spooled in a monolayer geometry and interrogated with the OTDR during irradiation. A radiation-hard transport fiber was used to connect the exposed section to the instrument, ensuring that the measured attenuation variations originated solely from the irradiated sample.

Figure 3.9: Photograph of the 20 m P-doped silica fiber arranged in a monolayer coil of 2.5 cm radius for irradiation.

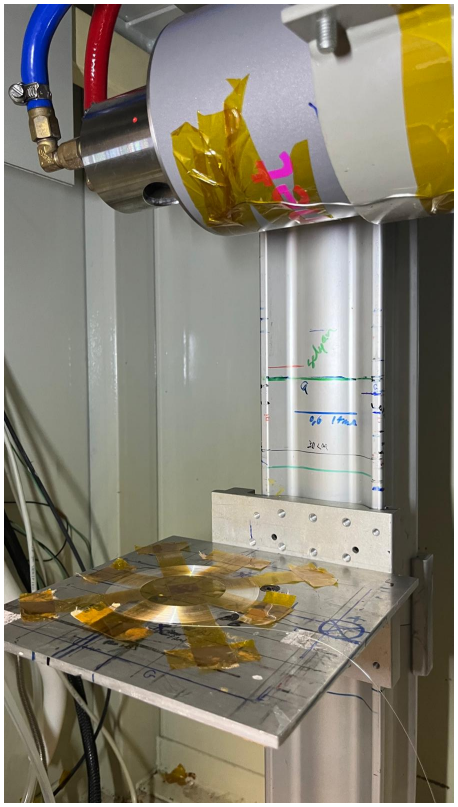

Figure 3.10: The MOPERiX X-ray irradiator at PETRA used for the RIA campaign. The fiber coil was placed in the irradiation field produced by the target. The coil on the square plate is the sample and the hole in the cylinder connected to the blue and red tubes is from where X-rays are emitted.

Data Analysis

The characterization of the RIA was carried out using an Optical Time Domain Reflectometer (OTDR). This technique allows to measure the optical power backscattered along the fiber as a function of distance, thus providing spatially-resolved information on the local transmission losses. In practice, the OTDR launches a sequence of short optical pulses into the fiber and records the intensity of the Rayleigh backscattered light as a function of the time-of-flight of the return signal. By converting time into distance, the resulting trace represents the response of the fiber along its entire length, meter by meter.

The initial portion of the trace corresponds to the transport or pigtail section, which is not directly exposed to radiation. Following this region, a distinct section appears, corresponding to the irradiated fiber sample. Within this portion, the recorded signal progressively decreases with increasing dose, due to the generation of radiation-induced defects that absorb and scatter light. The slope of this descending region is therefore directly related to the RIA, which quantifies the additional optical losses caused by irradiation.

The RIA is defined as the excess attenuation of the transmitted signal per unit length, as defined in Chapter 1. An increasing RIA corresponds to a larger induced absorption, and consequently to a steeper slope of the OTDR trace.

The final segment contains reflections from splices or connectors, which appear as sharp step-like peaks. These discontinuities are excluded from the slope fitting procedure, as they do not carry information on the RIA itself.

By comparing OTDR traces acquired at successive irradiation times, the progressive increase in slope provides a direct visualization of the RIA build-up as a function of dose.

A reference signal was firstly acquired before the irradiation start. Afterwards the irradiator was switched on for 375 s to obtain a total dose of 375 Gy. The data registered as a function of the fiber length were plotted. For clarity, only a limited number of representative profiles, corresponding to the unirradiated reference, an intermediate dose, and the maximum accumulated dose, are reported in Figure 3.11, which represents the complete OTDR profile along the whole scan length set to 100 m. Graphically, we choose a specific region in terms of length of the profile obtained, in order to have a signal not disturbed by the noise. Figure 3.12 represents a zoom on the region of the signal in function of length (15 - 19 m) interesting for the RIA analysis.

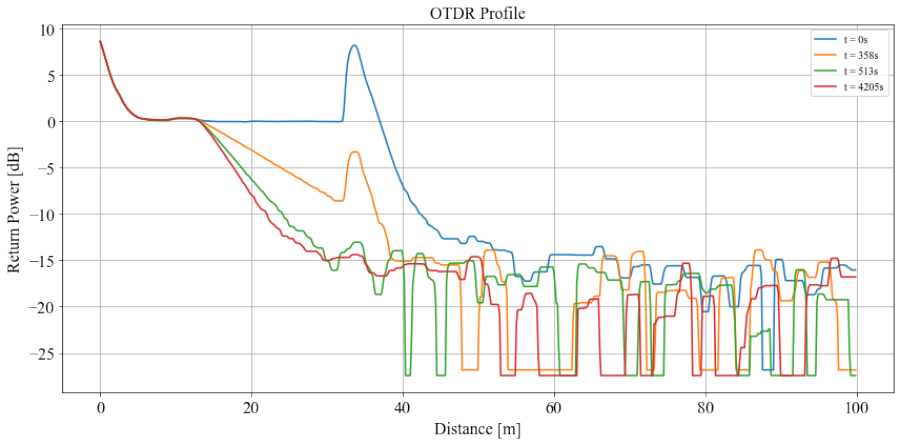

Figure 3.11: Representative OTDR backscatter profiles acquired during irradiation in function of time. The slope of the exposed section steepens progressively due to RIA. Step-like features correspond to splices and connectors and are excluded from the slope fitting.

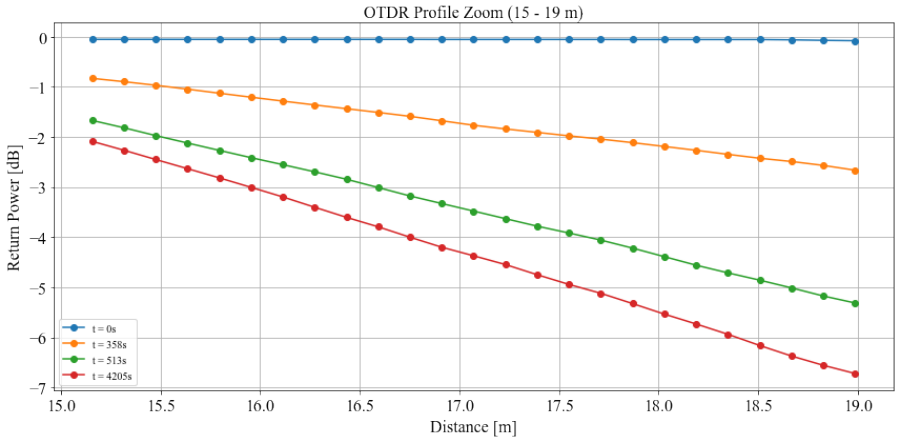

Figure 3.12: Zoom on the analyzed fiber span (15 - 19 m). Colored curves show successive acquisitions; dots mark the samples used for local linear fits to extract the attenuation coefficient $\alpha(z)$. It is possible to notice that the slope of the signal increases with time.

As already described, before irradiation a reference trace is acquired to determine the intrinsic losses of the pristine fiber, which include contributions from Rayleigh scattering and residual manufacturing defects. During irradiation, additional losses arise from the generation of radiation-induced point defects acting as absorption centers within the silica matrix. The total attenuation coefficient α_{tot} can therefore be written as the sum of two components:

$$\alpha_{tot}(\lambda, t) = \alpha_{int}(\lambda) + \alpha_{RIA}(\lambda, t), \tag{3.1}$$

where α_{int} is the intrinsic attenuation of the non-irradiated fiber, and α_{RIA} represents the additional attenuation induced by irradiation. This relation follows the conventional definition adopted in the literature for RIA, where it is expressed as the increase of the linear attenuation coefficient under irradiation with respect to the pristine value [64].

Experimentally, the slope of the logarithmic OTDR trace in the irradiated region provides a direct estimate of α_{tot}. The intrinsic coefficient α_{int} is determined from the pre-irradiation reference trace, and the radiation-induced term is obtained by subtraction:

$$\alpha_{RIA}(\lambda, t) = \alpha_{tot}(\lambda, t) - \alpha_{int}(\lambda). \tag{3.2}$$

This difference corresponds to the excess optical loss caused by the creation of radiation-induced defect centers. This approach allows the evaluation of the RIA evolution as a function of dose and distance along the fiber, following the methodology commonly adopted for distributed radiation measurements in optical fibers (see for example [12]).

This allows RIA as a function of time to be estimated starting form an OTDR track. The result of this data analysis is shown in Figure 3.13. The uncertaintes were estimated from the standard deviation of fit residuals and are shown as error bars.

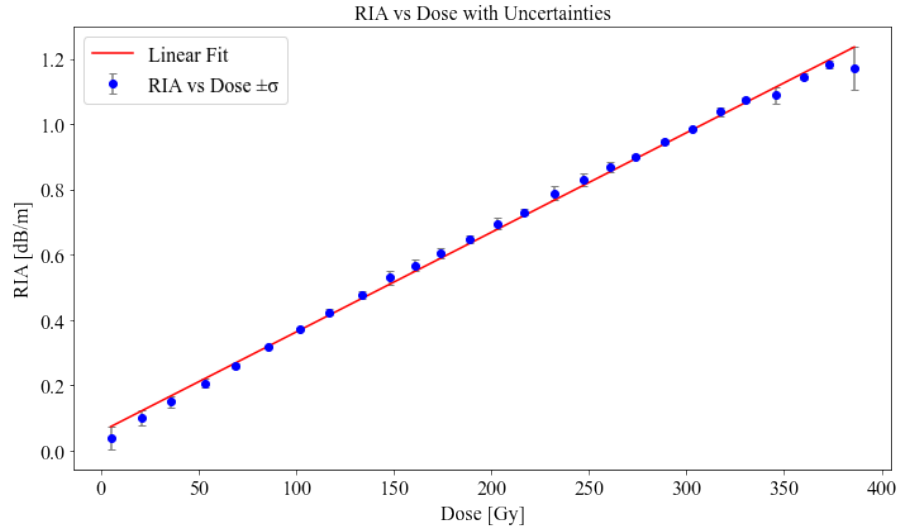

Figure 3.13: RIA as a function of the absorbed dose with linear fit with error bars ($\pm\sigma$ from fit residuals). The slope is 0.003135 dB·m^{-1}·Gy^{-1} (≈ 3.135 dB·km^{-1}·Gy^{-1}). RIA versus dose with error bars ($\pm\sigma$ from fit residuals). The linear model adequately describes the response in the analyzed dose range.

The obtained RIA exhibits a linear dependence on the absorbed dose within the investigated range, with a slope of (3.1 ± 0.1) dB·km^{-1}·Gy^{-1}, consistent with a proportional increase of induced absorption with dose. This behaviour confirms that the attenuation process is dominated by the formation of radiation-induced point defects whose concentration increases linearly with

deposited energy. The quality of the linear regression is confirmed by a coefficient of determination of R^2 = 0.998, indicating an excellent agreement between data and model. The slope value extracted from the fit is in good agreement with the results reported in the literature for P-doped fibers, which typically range between 3 and 4 dB·km^{-1}·Gy^{-1} under similar irradiation conditions [50].

3.3.2 Discussion and Conclusions

The OTDR measurements allows RIA measurement for dosimetry. The method allowed the determination of local attenuation coefficients, enabling quantification of the radiation response along the exposed fiber span. This spatially resolved capability represents a key advantage of OTDR-based dosimetry, as it provides information on the dose distribution along the fiber rather than a single integrated value. Such distributed measurement allows the detection of local inhomogeneities in the radiation field or the identification of regions subjected to different exposure conditions, which is particularly relevant for complex fields such as the one at the TRIGA TC.

The RIA versus dose curve (Figure 3.13) shows a linear trend with the parameters previously introduced, up to the maximum investigated dose of approximately $\sim$400 Gy. The sensitivity coefficient was found to be 0.0031 dB·m^{-1}·Gy^{-1}, with residual deviations within a few percent beyond 100 Gy. This value is in agreement with previous studies on this optical fiber [50]. OTDR investigation can provide a reliable estimation of absorbed dose. Beyond its sensitivity to radiation-induced attenuation, this technique offers specific advantages that make it particularly attractive for applications in complex irradiation facilities such as the TRIGA TC.

First, OTDR is a single-end measurement: both light injection and signal collection are performed from the same side of the fiber. This feature allows dosimetric monitoring in areas that are difficult to access or that cannot be instrumented on both ends, such as the inner regions of the TC, using only one optical port and a single interrogation unit located outside the biological shielding. Moreover, the method enables the acquisition of spatially resolved information along the fiber length, providing a distributed dose profile rather than a single integrated value, while also allowing almost real-time readout during irradiation.

Such characteristics could, in principle, make OTDR-based fibers suitable for permanent integration within the TC as part of a monitoring system capable of tracking the dose distribution during experimental campaigns. However, several practical challenges can be anticipated. The high radiation field may progressively degrade the fiber and connectors, thermal variations could influence both the optical response and the calibration stability and the long-term operation would require radiation-hardened feedthroughs and stable optical alignment over repeated reactor cycles. Nevertheless, the possibility of obtaining spatially resolved, single-end dose information in real time represents a significant advantage for experimental dosimetry in mixed neutron–photon environments.

The effective spatial resolution is limited by the OTDR pulse width and SNR, which in this configuration allows reliable extraction of attenuation over windows of a few meters. This sets the minimum detectable irradiated length for this technique. The broad appearance of the splice signature is consistent with the effective spatial resolution of approximately 1 m in this configuration.

Error bars derived from the standard deviation of the linear regression slopes, obtained from the residuals of each fit, remain below ± 0.05 dB·m^{-1} across the investigated dose range. This corresponds to a relative uncertainty below 5% on the RIA values, indicating good reproducibility of the measurements and reliable sensitivity estimation.

The results show that OTDR-based monitoring can provide both real-time and distributed dosimetric information with a simple setup.

3.4 A setup for pulsed X-ray irradiations for FLASH Radiotherapy applications

In recent years, an innovative radiotherapy technique, known as FLASH (FLASH RT) has attracted growing interest. It was observed that irradiation delivered at ultra-high dose rate (UHDR, $>$40 Gy/s) leads to a remarkable sparing of normal tissues while maintaining tumor control comparable to conventional dose rate ($\sim$0.1 Gy/s) radiotherapy [65]. This property has the potential to substantially expand the therapeutic window of RT.

A key feature of FLASH RT is the dependence of normal tissue sparing on both the dose and the temporal structure of irradiation. Quantitative analyses have demonstrated that the FLASH effect becomes more pronounced for single-fraction doses above 5-10 Gy, provided that the entire fraction is delivered within a time window shorter than 200 ms [66].

Although the underlying mechanisms are not yet fully cleared, several hypotheses have been advanced. Among the most widely discussed is the oxygen depletion hypothesis, according to which UHDR irradiation transiently reduces tissue oxygenation, decreasing the production of DNA-damaging reactive oxygen species. Other proposed mechanisms include modifications of the immune response and altered redox signaling. Regardless of the precise biological basis, extensive preclinical evidence supports the FLASH effect. Studies in mice, mini-pigs, cats and dogs have consistently shown reduced acute and late toxicity in organs such as brain, skin and intestine, while tumor control remained unaffected. Furthermore, the first patient was treated with electron FLASH RT in 2019, marking a milestone in its clinical translation [67].

The vast majority of preclinical and early clinical FLASH studies have employed high-energy electron (HEE, 4-20 MeV) beams, which are well suited for superficial targets. Such beams can be generated by either dedicated compact accelerators or by modified clinical linear accelerators operating in UHDR mode [65]. However, their limited penetration depth restricts applications to shallow lesions or intraoperative settings.

To overcome this limitation, very-high energy electron (VHEE, 50-250 MeV) beams have been proposed. VHEEs can reach deep-seated tumors while offering sharp lateral penumbrae, potentially enabling treatments with conformity comparable to intensity-modulated photon therapy. In addition, the compactness and cost-effectiveness of VHEE accelerators make them attractive candidates for future clinical adoption [68].

Unlike conventional RT, where sophisticated treatment planning systems (TPS) are routinely employed, FLASH RT has so far been delivered with simplified irradiation geometries, often single

broad beams. Nevertheless, the transition to more complex anatomical sites will require accurate three-dimensional planning and beam modeling.

Monte Carlo (MC) methods represent the gold standard for dose calculation in UHDR electron beams, due to their ability to account for tissue heterogeneities and beam transport physics with high accuracy. However, FLASH treatment planning must address challenges that go beyond dose distribution alone:

- Incorporation of temporal delivery parameters, such as pulse repetition frequency, dose per pulse and intra-pulse dose rate.
- Definition of FLASH predictors, such as quantitative metrics to estimate the probability of inducing the FLASH effect, based on dose, delivery time and dose-rate thresholds.
- Standardization of dose and beam parameter reporting across different experimental platforms, to ensure reproducibility and comparability of clinical outcomes.

The integration of quantitative analyses of normal tissue sparing with advanced treatment planning tools provides the basis for the clinical translation of FLASH RT. The initial applications are likely to involve superficial lesions and intraoperative radiotherapy, where large single fractions are already standard practice. Looking further ahead, the development of compact VHEE systems and the implementation of beam delivery techniques optimized for UHDR conditions may enable FLASH RT to treat deep-seated tumors, potentially rivaling or surpassing the conformity of current photon and proton modalities.

FLASH RT represents one of the most promising innovations in radiation oncology. The combined effort of biological research, technological development and treatment planning optimization will be crucial to realize its clinical potential and establish it as a standard modality in the fight against cancer.

3.5 Introduction to pulsed irradiation tests

Studies of RIL in optical fibers have long been performed under continuous irradiation [64]. Such tests make it possible to pin down essential features of the response: how the signal scales with dose, how it changes with fiber length, and steady-state phenomena such as afterglow and the Bright Burn Effect (BBE). Yet, continuous exposure does not mirror the timing of modern accelerator beams, which are often delivered in pulses, nor does it reflect the conditions typical of FLASH radiotherapy.

In FLASH radiotherapy, very high doses are delivered in ultra-short time windows, commonly as trains of high-intensity pulses at ultra-high dose rate (UHDR) [69][70]. Under these conditions, a dosimeter must resolve single pulses, recover quickly from one pulse to the next, and keep parasitic contributions as low as possible. Measurements performed only in continuous mode are not sufficient to test these requirements, which motivates dedicated pulsed-irradiation studies.

Recent work has shown that optical fibers can track pulsed accelerator beams, while also mapping out the limitations that appear at UHDR [71].

In this context, we developed a dedicated setup to perform pulsed X-ray irradiations and acquire the RIL signal in real time. The system, designed and implemented as part of [55], was used to probe the temporal behavior of M-OH pure-silica fibers under pulsed conditions, with the goal of assessing their suitability for FLASH-oriented applications. The pulsed tests yield information on how the RIL signal evolves between consecutive pulses, on the size of the afterglow, and on possible parasitic effects. Making a clear connection between this temporal response and the needs of FLASH dosimetry is a necessary step toward real-time, pulse-resolved monitoring for advanced radiotherapy.

3.5.1 Materials and Methods

A dedicated setup was developed in order to create conditions for pulsed irradiation by using the LabHC X-ray continuous beam. The system, schematically shown in Figure 3.14, is based on a rotating aluminum disk with an open window of 0.242 rad, positioned between the X-ray source and the optical fiber holder. The fiber sample was aligned along the disk diameter and placed 3 cm below it, so that each disk rotation alternately exposed or shielded the fiber from the beam. Depending on the angular position of the aperture, the sample could be fully shielded (beam OFF) or fully exposed (beam ON). To ensure mechanical stability, the disk was designed with alternating sectors of one and two aluminum layers. As a result, three distinct conditions were periodically produced during rotation: full transmission through the open window, partial attenuation through a single aluminum layer and strong attenuation through two aluminum layers. As verified with a calibrated ionization chamber at the sample position, the shielded sectors reduce the dose rate by a factor of $\sim$2.1 for one aluminum layer and by $\sim$41 for two aluminum layers, with respect to the open window configuration and the corresponding RIL amplitudes decrease proportionally.

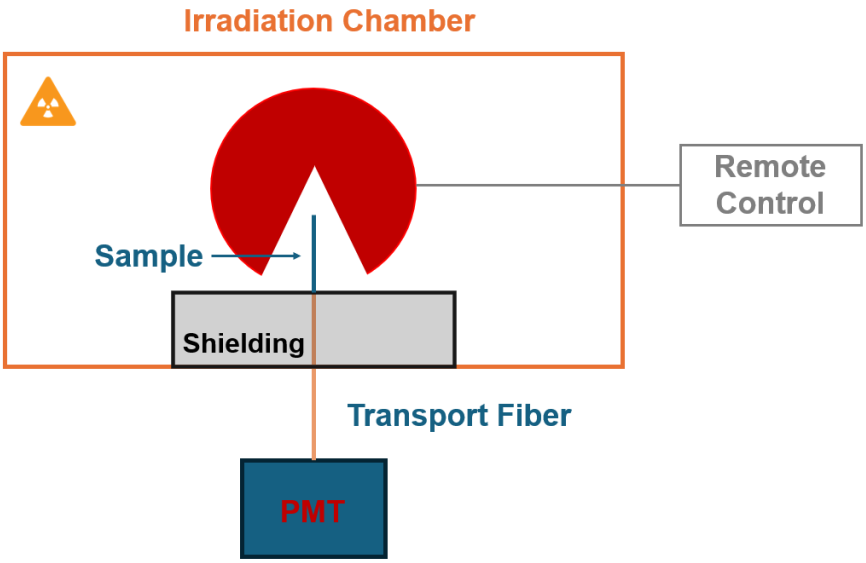

Figure 3.14: Schematic of the setup used in the pulsed tests, view from above.

The transport fiber (M-OH) guiding the RIL signal to the photomultiplier tube (PMT) was shielded with $\sim$3 mm of lead to minimize spurious contributions. Figure 3.15 shows the experimental

setup.

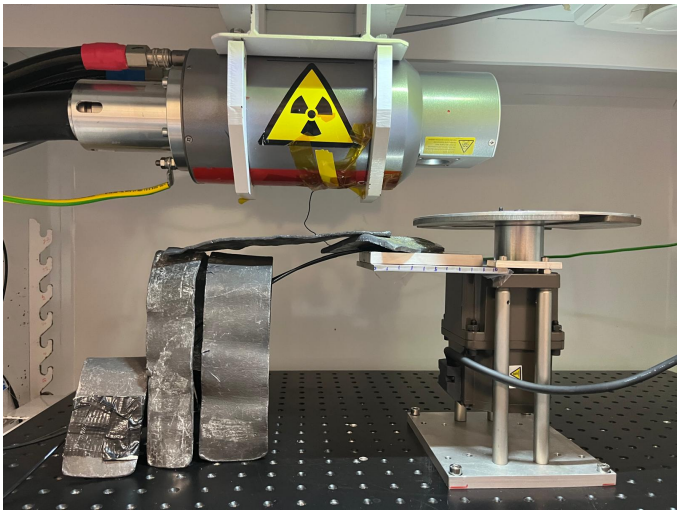

Figure 3.15: Rotating disk setup for pulsed RIL measurements, showing the source, the aluminum disk and the lead shielding of the transport fiber.

The data were acquired with a time resolution of 1 ms for the rotation at 56 rad/min, corresponding to ON/OFF times of ∼259 ms and 6.47 s, respectively, and 500 μs for the one at 112 rad/min, which halved these durations. The beam ON and beam OFF times per rotation could be estimated from the window opening angle and the rotation speed. This made it possible to probe different inter-pulse intervals and evaluate whether afterglow from one pulse overlapped with the subsequent one.

The pulsed irradiation campaign was performed by varying the X-ray tube current to deliver dose rates of 0.04, 0.07, 0.35, 0.71, 3.54, 7.08, 10.63, and 21.29 Gy(SiO_2)/s to the samples. Two types of optical fibers were investigated, as in the continuous RIL experiment discussed in Chapter 3: a Ce-doped reference fiber (2 cm long) and an M-OH pure silica fiber (7 cm long), both tested under identical conditions.

3.5.2 Results and Discussion

Both fibers were able to follow the modulation introduced by the rotating disk. Figure 3.16 shows the RIL temporal traces recorded at a rotation speed of 56 rad/min for an irradiation at 10.63 Gy(SiO_2)/s, comparing the responses of the 2 cm Ce-doped reference fiber and the 7 cm M-OH fiber. The periodic modulation of the RIL signal reflects the alternation of the open and shielded sectors of the rotating disk: high peaks correspond to the fully exposed beam, intermediate levels to the partially shielded regions (single aluminum layer, attenuated dose), and minima to the double-layer sectors where the beam is completely blocked (beam OFF).

In the attenuated regions, the RIL amplitude decreased by a factor of ∼2.1 with one aluminium layer and by ∼41 with two layers. The RIL signal scaled consistently with the delivered dose rate, confirming the linear behaviour of both fiber types under pulsed conditions.

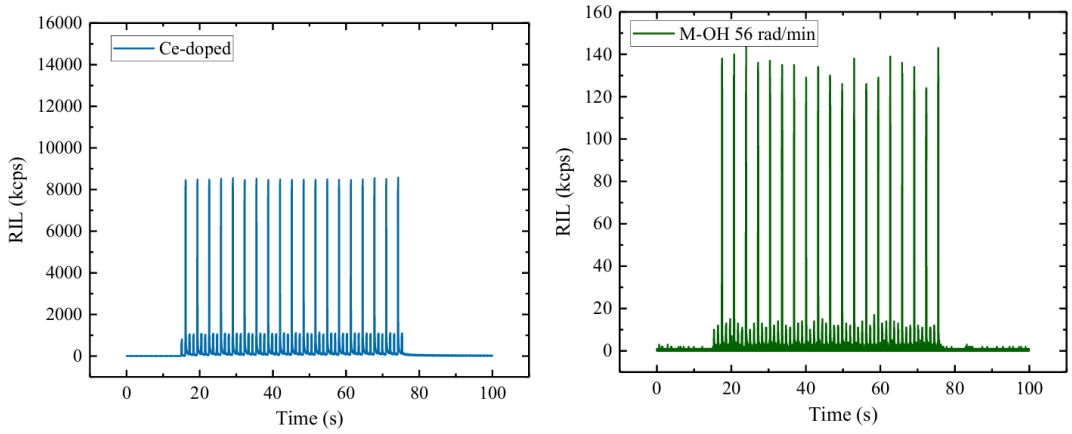

Figure 3.16: RIL as a function of time for a disk rotation frequency of 56 rad/min and 60 s irradiation. Data refer to selected results of the 7 cm M-OH fiber and the 2 cm Ce-doped reference, at a dose rate of 10.63 Gy(SiO_2)/s.

A crucial difference emerged when analyzing the traces acquired at the higher rotation speed of 112 rad/min (Figure 3.17). The M-OH fiber exhibited a very fast recovery to baseline ($t_{rec} \approx 34$ ms), defined as the time required for the RIL signal to decrease to within 5% of its pre-pulse level, allowing each pulse to be clearly distinguished from the next. In contrast, the Ce-doped fiber showed a persistent afterglow, with residual luminescence tails extending into the OFF period and partially overlapping with subsequent pulses.

These observations were consistent across all dose rates and rotation speeds tested. The fast recovery of the M-OH fiber could represent a clear advantage for applications in which pulses are delivered at short intervals, such as in FLASH radiotherapy.

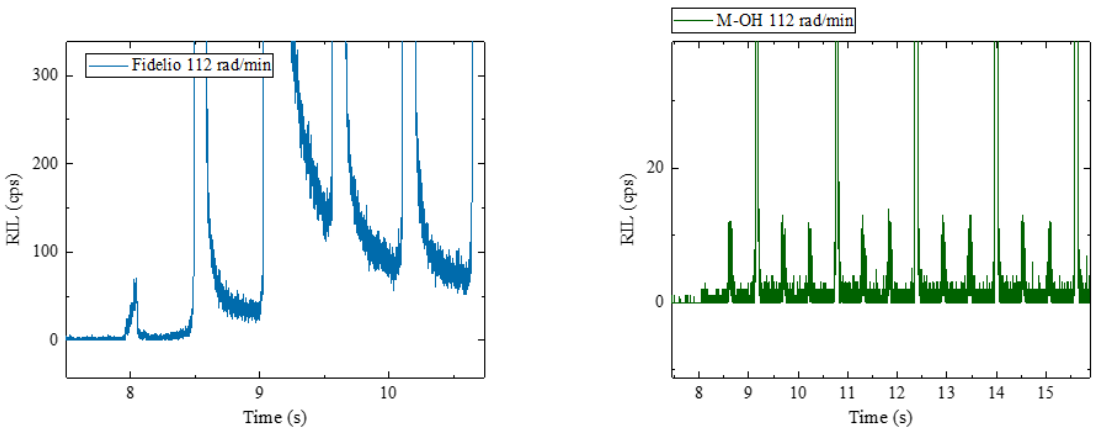

Figure 3.17: Zoom on the first pulses recorded at 112 rad/min. Comparison between the Ce-doped fiber (left) and the M-OH fiber (right).

The pulsed tests highlight the complementary behaviour of the two fiber types. Ce-doped fibers

provide high intrinsic sensitivity but suffer from significant memory effects that complicate pulse discrimination. Conversely, M-OH fibers show lower per unit length sensitivity but combine linearity, tunability of response with fiber length, and negligible afterglow.

For FLASH RT, where accurate monitoring of ultra-high dose rate pulses is essential, the M-OH fiber emerges as a promising candidate. Its rapid decay prevents overlap between closely spaced signals, ensuring reliable reconstruction of the dose delivered per pulse. In addition, the minimal contribution from parasitic effects strengthens its suitability as both a transport element in hybrid systems and as a potential standalone dosimeter.

The pulsed irradiation experiments confirmed the strong potential of M-OH PSC OF in particular, but of optical fibers in general, for FLASH-related dosimetry. They exhibited:

- a linear dose-rate response under pulsed conditions,
- fast recovery dynamics ($t_{rec} \sim 34$ ms)
- limited afterglow and negligible BBE

Although Ce-doped fibers remain highly efficient light emitters, their persistent afterglow reduces their usefulness in UHDR pulsed regimes. The M-OH fibers therefore represent a more robust option for time-resolved dosimetry, particularly in the perspective of FLASH radiotherapy, where pulse-resolved and real-time monitoring is a prerequisite for safe and effective clinical implementation.

The experimental evidence obtained at PETRA, both in continuous and pulsed photon regimes, complements the TRIGA studies by demonstrating the versatility of silica-based optical fibers across distinct non-conventional radiotherapy modalities.

Chapter 4

Feasibility of RIL and RIA Experiments at the TRIGA Reactor

From a practical standpoint, assessing the feasibility of performing the proposed experimental techniques within the TRIGA thermal column requires careful consideration. In this environment, the mixed neutron–photon field differs substantially from the pure photon conditions reproduced at PETRA. Neutrons, in particular, can induce additional damage mechanisms in silica, leading to the formation of specific defect populations that may alter both the kinetics and the spectral characteristics of RIA [72].

From the perspective of RIA experimental design, it is therefore essential to estimate the fiber length required to detect the expected attenuation under the mixed-field conditions of the TRIGA column. Using the simulation results reported in Chapter 2 and assuming a source emission rate in the range of 10^{10}–10^{12} source/s for neutrons and 10^{9}–10^{11} source/s for photons [28], a dose rate of approximately $\sim$1.4 mGy/s can be expected at the analyzed position.

For P-doped fibers, the radiation-induced losses at 1550 nm increase linearly with absorbed dose up to about 500 Gy, with a typical sensitivity coefficient (S) of 4 dB/(km·Gy) [73]. This parameter quantifies the incremental optical attenuation per unit dose and per unit fiber length. Knowing the instrument dynamic range (DR), the total dose (D_T) expected during an irradiation of duration , and the fiber sensitivity S, the required fiber length L for a measurable OTDR signal can be estimated as:

$$L = \frac{DR}{D_T \cdot S}. \tag{4.1}$$

Considering an average BNCT irradiation time of approximately one hour (t = 3600 s) and a dose rate of $\sim$1.4 mGy/s, the corresponding total dose is $D_T \approx 5.04$ Gy. Assuming a dynamic range of 5 dB (see Figure 3.13), the minimum fiber length is therefore:

$$L = \frac{5 \text{ dB}}{5.04 \text{ Gy} \times 4 \, \frac{\text{dB}}{\text{km·Gy}}} \approx 0.24 \text{ km} = 240 \text{ m}. \tag{4.2}$$

Thus, a total fiber length of about 240 m would be required to obtain a measurable RIA signal in the OTDR trace under the expected dose rate of the TRIGA thermal column.

To verify the mechanical feasibility of this configuration, it is useful to estimate the dimensions of a single-layer spool capable of hosting this fiber length and to compare them with the internal cavity of the thermal column. Assuming an initial inner radius of r_0 = 2.5 cm and a radial increment between successive turns equal to the fiber outer diameter (t = 234 μm, as in the simulated model), the total wound length after N turns can be expressed as:

$$L(N) = \sum_{k=0}^{N-1} 2\pi(r_0 + k\,t) = 2\pi\left(Nr_0 + \frac{t}{2}N(N-1)\right), \tag{4.3}$$

where:

- $L(N)$ is the total fiber length after N turns [cm],
- r_0 is the radius of the first turn (centerline) [cm],
- t is the radial step between turns, equal to the fiber outer diameter [cm],
- N is the total number of turns,
- k is the turn index.

Solving Eq. 4.3 for $L(N)$ = 240 m yields approximately N = 475 turns, corresponding to an external coil diameter of $\approx$ 27.2 cm. Considering that the thermal column cavity measures 20.5 cm $\times$ 40 cm $\times$ 103.5 cm (see Chapter 2), this dimension is fully compatible with the available space when the spool is positioned horizontally on the bottom surface, parallel to the reactor floor.

Nevertheless, this configuration must account for the spatial variation of the mixed field across the coil diameter, which could result in non-uniform dose deposition among the fiber turns. A possible mitigation strategy involves performing double-ended RIA measurements, by connecting a white-light source and a spectrometer to the two fiber ends and analyzing the transmitted spectrum. This approach, already implemented in the LUMINA experiment aboard the International Space Station [74], would also enable the use of a multi-layer coil configuration to optimize space utilization and detection sensitivity. Alternatively, operating at shorter wavelengths (in the visible range) could enhance the sensitivity coefficient, thereby reducing the required fiber length for a given measurable attenuation [63], although this approach remains less explored.

Furthermore, it is important to estimate the minimum irradiation time required to acquire the first detectable point of the measurement, which is the time necessary for the induced attenuation to exceed the detection threshold of the instrument. For the OTDR system employed, the minimum detectable loss corresponds to approximately 0.01 dB. Dividing this value by the total fiber length estimated above (0.24 km) yields an equivalent distributed loss of 0.04 dB/km. By further dividing this quantity by the fiber sensitivity coefficient ($S = 4$ dB/(km $\cdot$ Gy)), the minimum visible dose increment can be determined as:

$$D_{\text{min}} = \frac{0.04 \text{ dB/km}}{4 \text{ dB}/(\text{km} \cdot \text{Gy})} = 0.01 \text{ Gy}.$$

This means that, under the expected dose rate of $\sim$1.4 mGy/s, the system would require approximately 7 s to accumulate the minimum measurable RIA signal. Therefore, over an irradiation time of 1 hour, the number of measurable data points would be largely sufficient to perform a reliable dosimetric analysis of the fiber response. Also for a typical radiobiology experiment lasting 10 minutes (plus power-rise time) the number of measurable data guarantee a sufficient statistics.

As discussed in Chapter 1, unlike RIA measurements, which are relative, RIL measurements are absolute. It is therefore crucial to determine the expected signal counts at the considered dose rate to ensure a detectable signal above the noise level. From the results presented in Chapter 3, and in particular from the slope of the blue curve for the Ce-doped fiber in Figure 3.6, the estimated photon count rate at $\sim$1.4 mGy/s is approximately 730 kcounts/s. Comparing this value with the signal noise variation observed in the same experiment ($\sim$4 kcounts/s) confirms the detectability of the RIL signal under these conditions. Overall, these analyses confirm the feasibility of the proposed experiment in the TRIGA thermal column, while keeping in mind that the presented calculations and laboratory measurements were carried out under controlled conditions, and that the reported dose rate represents an equivalent value.

Several additional parameters could influence the final RIL signal. For instance, the splice between the sensing and transport fibers (M–OH), the connection to the detection system, and particularly the presence of external light may degrade the measurement. To mitigate the latter issue, shielded transport fibers and properly sealed optical passages can be employed. Moreover, the photomultiplier tube (PMT) can be placed in a darkened area of the reactor hall, where radiation levels are sufficiently low to ensure its long-term stability. Such arrangements have already been successfully implemented in similar setups using custom M–OH transport fibers, demonstrating that adequate optical shielding and detector positioning can be achieved in practice [75].

Clearly, all these aspects must ultimately be evaluated *in situ* to quantify the relative impact of the different factors. For instance, light shielding for RIL measurements could lead to a partial reduction of the detected signal, since dark conditions are more challenging to achieve in the reactor environment than in the controlled laboratory conditions of the LabHX facility in Saint-Étienne. Another key distinction lies in the length of the transport fibers, expected to be considerably longer than those implemented in the laboratory setup, thereby introducing higher transmission losses and affecting the overall signal-to-noise ratio.

Conclusions

The work presented in this thesis explored the feasibility of using optical fibers for dosimetry in mixed neutron-photon environments, with specific reference to the TRIGA Mark II reactor in Pavia. The experimental part of the work was also contributory for studies of medical physics, such as FLASH therapy, where many dosimetry challenges remain still open.

Two complementary approaches were adopted: performing Monte Carlo simulations with the PHITS code to model the radiation field within the thermal column of the reactor and conducting experimental investigations of radiation-induced effects in optical fibers under controlled X-ray irradiation at the PETRA platform in Saint-Etienne.

The PHITS simulations provided quantitative information on the spatial distribution of neutron and photon fluence, as well as on the corresponding dose components in the different fibers layers (coating, cladding and core). The results confirmed that the neutron contribution dominates for the absorbed dose by roughly one order of magnitude, with energy deposition mainly governed by n-H elastic scattering in the hydrogen-rich coating. This paves the way for future development of optical fiber based dosimetry, able to discriminate the different dose components due to neutrons and photons, where other types of detectors fail in separating the two contributions. The fluence and dose trends in the three layers of the fiber were calculated. These findings were used to establish reference dose rates for subsequent feasibility studies.

On the basis of the obtained results, the feasibility of the implementation of fiber-based dosimetry in the TRIGA thermal column was assessed. A 240 m monolayer spool of P-doped optical fiber configuration for RIA measurements was designed and found to fit within the available space of the column cavity. Furthermore, considering a typical BNCT irradiation time of one hour and the time required to acquire one point estimated to be 7 s, it was possible to determine the feasibility of RIA OTDR-based dosimetry. Moreover, the proposed setup can be adapted for double-ended or multi-layer configurations to further improve sensitivity and spatial resolution in future developments. The RIL based detection possibility is ensured by the fact that the expected number of counts is significantly higher than the expected noise level.

The experimental activity in Saint-Etienne focused on the optical response of P-doped fibers for Radiation Induced Attenuation (RIA) measurements, Ce-doped and M-OH fibers for Radiation Induced Luminescence (RIL) measurements, all simulated with Monte Carlo simulations, under continuous and pulsed X-ray irradiation. The results confirmed the stability and linearity of both RIA and RIL signals.

A novel outcome of this work was the identification of the M-OH fiber as an active sensing element, particularly under pulsed radiation conditions, in addition to its conventional role as transport fiber. This finding is especially relevant in the context of FLASH radiotherapy, where accurate monitoring of ultra-high dose rate pulses is essential. The M-OH fiber emerges as a promising candidate, because of the minimal parasitic effects (afterglow and Bright Burn Effect) and fast signal decay after irradiation end, which prevents the overlap between closely spaced signals, ensuring reliable reconstruction of the dose delivered per pulse. Given the innovative nature of these findings and their potential applications, we have further investigated them in an article submitted for publication in *physica status solidi (a)* [55].

In conclusion, this work demonstrated that optical fibers based sensors (specifically P-doped for RIA, Ce-doped for RIL and M–OH used both as transport fiber and sensing element) could serve as effective dosimetric sensors in mixed neutron–photon fields. The combined use of simulations and experimental investigations allowed to obtain a coherent picture of the system response and of its limitations, providing solid basis for defining the experimental conditions of future measurements in the thermal column of the TRIGA reactor. Moreover, for FLASH radiotherapy, the promising results obtained with the M-OH fiber open the possibility of developing fiber-based systems capable of real-time monitoring of ultra-high dose rate beams, a key step toward accurate dosimetry in this emerging modality.

Further developments will include the experimental validation of the proposed configuration under real reactor conditions and the extension and optimization of this methodology to high-dose and pulsed environments relevant to FLASH radiotherapy research.

Bibliography

[1] Frank Herbert Attix. *Introduction to Radiological Physics and Radiation Dosimetry*. Wiley-VCH, 1986. ISBN: 978-0-471-01146-0.

[2] ICRU. *Fundamental Quantities and Units for Ionizing Radiation*. Tech. rep. Report 85. Bethesda, MD, USA: International Commission on Radiation Units and Measurements, 2011.

[3] Peter Mayles, Alastair F. Nahum, and Jean-Claude Rosenwald, eds. *Handbook of Radiotherapy Physics: Theory and Practice*. Boca Raton, FL, USA: CRC Press, 2007. ISBN: 978-0-3671-9207-5.

[4] P. Marmier and E. Sheldon. *Physics of Nuclei and Particles*. Vol. 1. 3 vols. Academic Press, 1969.

[5] Ashraf Almahwasi. *Does Hadron Therapy Offer Enough Effectiveness in Treating Cancer to be Worth the Cost?* ResearchGate preprint. Dec. 2016. DOI: 10.13140/RG.2.2.35789.64482.

[6] Wazir Muhammad, Amjad Hussain, and Muhammad Maqbool. "Basic Concepts in Radiation Dosimetry". In: *An Introduction to Medical Physics*. Springer, 2017, pp. 9–41.

[7] Fiammetta Fricano. "Real-time dosimetry: feasibility and optimization of radioluminescent optical fiber sensors". Unpublished doctoral dissertation. PhD thesis. University Jean Monnet Saint-Étienne, Member of the University of Lyon, Hubert Curien Laboratory, 2025.

[8] F. Ravotti. "Dosimetry Techniques and Radiation Test Facilities for Total Ionizing Dose Testing". In: *IEEE Transactions on Nuclear Science* 65.8 (Aug. 2018), pp. 1440–1464. DOI: 10.1109/TNS.2018.2829864.

[9] Reuven Chen and Stephen W.S. McKeever. *Theory of Thermoluminescence and Related Phenomena*. Vol. 5. World Scientific Series in Nuclear Science and Technology. World Scientific, 1997. DOI: 10.1142/2781.

[10] Max Born and Emil Wolf. *Principles of Optics: Electromagnetic Theory of Propagation, Interference and Diffraction of Light*. 7th. Cambridge University Press, 1999. ISBN: 9780521642224.

[11] S. Girard et al. "Radiation Effects on Silica-Based Optical Fibers: Recent Advances and Future Challenges". In: *IEEE Transactions on Nuclear Science* 55.6 (2011), pp. 3752–3772. DOI: 10.1109/TNS.2012.2235464.

[12] S. Girard et al. “Overview of Radiation Effects on Silica-Based Optical Fibers and Fiber Sensors”. In: *IEEE Transactions on Nuclear Science* 72.4 (2025), pp. 982–1020. DOI: 10.1109/TNS.2024.3511455.

[13] Samuel Usherovich et al. “Optical fibre array detector to monitor irradiations for medical radioisotope production”. In: *Journal of Physics: Conference Series* 2374.1 (Nov. 2022), p. 012182. DOI: 10.1088/1742-6596/2374/1/012182. URL: https://dx.doi.org/10.1088/1742-6596/2374/1/012182.

[14] Crystal Penner et al. “A Multi-Point Optical Fibre Sensor for Proton Therapy”. In: *Electronics* 13.6 (Mar. 2024), p. 1118. DOI: 10.3390/electronics13061118.

[15] Jeffrey A Coderre et al. “Boron neutron capture therapy: cellular targeting of high linear energy transfer radiation”. In: *Technology in cancer research & treatment* 2.5 (2003).

[16] Barbara Marcaccio. “Dagli esperimenti radiobiologici al treatment planning per i pazienti: uno studio dosimetrico in BNCT”. Tesi di Laurea Magistrale. Università degli Studi di Pavia, Dipartimento di Fisica, 2020. URL: https://hdl.handle.net/20.500.14239/13397.

[17] Leena Kankaanranta et al. “Boron neutron capture therapy in the treatment of locally recurred head-and-neck cancer: final analysis of a phase I/II trial”. In: *International Journal of Radiation Oncology* Biology* Physics* 82.1 (2012), e67–e75.

[18] R. F. Barth et al. “Current status of boron neutron capture therapy of high grade gliomas and recurrent head and neck cancer”. In: *Radiation Oncology* 7 (2012), p. 146. DOI: 10.1186/1748-717X-7-146. URL: https://doi.org/10.1186/1748-717X-7-146.

[19] A. Wittig et al. “Neutron activation of patients following boron neutron capture therapy of brain tumors at the high flux reactor (HFR) Petten (EORTC Trials 11961 and 11011)”. In: *Strahlentherapie und Onkologie* 181.12 (Dec. 2005), pp. 774–782. ISSN: 0179-7158. DOI: 10.1007/s00066-005-1433-4.

[20] *Advances in Boron Neutron Capture Therapy*. TECDOC Series. Vienna: INTERNATIONAL ATOMIC ENERGY AGENCY, 2023.

[21] Issam El Naqa, Piotr Pater, and Jan Seuntjens. “Monte Carlo role in radiobiological modelling of radiotherapy outcomes”. In: *Physics in Medicine & Biology* 57.11 (May 2012), R75. DOI: 10.1088/0031-9155/57/11/R75.

[22] D. Alloni et al. “Neutron Flux Characterization of the Pavia TRIGA MARK II Research Reactor for Radiobiological and Microdosimetric Applications”. In: *Progress in Nuclear Energy* 83 (2015), pp. 153–161. DOI: 10.1093/rpd/ncv291.

[23] D. Morselli et al. “Production and characterization of ^{111}Ag radioisotope for medical use in a TRIGA Mark II nuclear research reactor”. In: *Applied Radiation and Isotopes* 197 (2023), p. 110798. DOI: 10.1016/j.apradiso.2023.110798.

[24] Università degli Studi di Pavia. *Laboratorio Energia Nucleare Applicata (LENA)*. URL: https://lena.unipv.it/ (visited on 09/29/2025).

[25] Matteo Ferrari et al. “Experimental study of consistency degradation of different greases in mixed neutron and gamma radiation”. In: *Heliyon* 5.9 (2019).

[26] Matteo Ferrari et al. “Characterization of a polyphenyl ether oil irradiated at high doses in a TRIGA Mark II nuclear reactor”. In: *Nuclear Instruments and Methods in Physics Research Section B: Beam Interactions with Materials and Atoms* 497 (2021), pp. 1–9.

[27] Matteo Ferrari. “Caratterizzazione della Componente di Dose Gamma nella Facility di Irraggiamento per BNCT e Dosimetria per Esperimenti in Vitro Presso il Reattore TRIGA di Pavia”. Supervisor: S. Altieri. Master’s thesis. University of Pavia, 2013. URL: https://hdl.handle.net/20.500.14239/24976.

[28] S. Bortolussi et al. “Neutron flux and gamma dose measurement in the BNCT irradiation facility at the TRIGA reactor of the University of Pavia”. In: *Nuclear Instruments and Methods in Physics Research, Section B: Beam Interactions with Materials and Atoms* 414 (2018), pp. 113–120. DOI: 10.1016/j.nimb.2017.10.023.

[29] A. Zonta et al. “Extra-corporeal liver BNCT for the treatment of diffuse metastases: What was learned and what is still to be learned”. In: *Applied Radiation and Isotopes* 67.7, Supplement (2009), S67–S75. DOI: 10.1016/j.apradiso.2009.03.087.

[30] A. Zonta et al. “Clinical lessons from the first applications of BNCT on unresectable liver metastases”. In: *Journal of Physics: Conference Series* 41.1 (2006), pp. 484–395. DOI: 10.1088/1742-6596/41/1/054.

[31] Denise B. Pelowitz et al. *MCNP – A General Monte Carlo N-Particle Transport Code, Version 6.3*. LA-UR-23-10009. Los Alamos National Laboratory. Los Alamos, NM, 2023.

[32] V. Dattoli Viegas et al. “Detailed dosimetry calculation for in-vitro experiments and its impact on clinical BNCT radiobiology”. In: *Physica Medica* 89 (2021), pp. 135–144. DOI: 10.1016/j.ejmp.2021.08.010.

[33] Diego Alberti et al. “A theranostic approach based on the use of a dual boron/Gd agent to improve the efficacy of Boron Neutron Capture Therapy in the lung cancer treatment”. In: *Nanomedicine: Nanotechnology, Biology and Medicine* 11.3 (2015), pp. 741–750.

[34] A. Wittig et al. “Boron neutron capture therapy for an explanted organ: The logistical challenges”. In: *Applied Radiation and Isotopes* 67.7, Supplement (2009), S302–S305. DOI: https://doi.org/10.1016/j.apradiso.2009.03.068.

[35] V. A. Nievaart et al. “Design of a Rotating Facility for Extracorporal Treatment of an Explanted Liver with Disseminated Metastases by Boron Neutron Capture Therapy with an Epithermal Neutron Beam”. In: *Radiation Research* 166.1 (2006), pp. 81–88. DOI: 10.1667/RR3535.1.

[36] G. Hampel et al. “Irradiation facility at the TRIGA Mainz for treatment of liver metastases”. In: *Applied Radiation and Isotopes* 67.7, Supplement (2009), S238–S241. URL: https://doi.org/10.1016/j.apradiso.2009.03.079.

[37] Jorge E. Cardoso et al. “Effect of Boron Neutron Capture Therapy (BNCT) on normal liver regeneration: Towards a novel therapy for liver metastases”. In: *International Journal of Radiation Biology* 83.10 (2007), pp. 699–706. DOI: 10.1080/09553000701570212.

[38] D. W. Nigg et al. “Validation of computational methods for BNCT treatment planning at the Idaho National Engineering Laboratory”. In: *Medical Physics* 23.11 (1996), pp. 1969–1980.

[39] Barbara Marcaccio et al. “Towards an adequate description of the dose-response relationship in BNCT of glioblastoma multiforme”. In: *Medical Physics* 52.4 (2025), pp. 2606–2617. DOI: 10.1002/mp.17693.

[40] Diego Di Francesca et al. “Implementation of optical fiber based dosimetry at CERN”. In: *Optical Fiber Sensors*. Optica Publishing Group. 2018, WC1.

[41] Jérémy Perrot et al. “Radiation vulnerability of optical fiber cables for underground nuclear waste monitoring”. In: *Optical Fiber Technology* 92 (2025), p. 104181.

[42] Sylvain Girard et al. “Recent advances in radiation-hardened fiber-based technologies for space applications”. In: *Journal of Optics* 20.9 (2018), p. 093001.

[43] Sylvain Girard et al. “Overview of radiation induced point defects in silica-based optical fibers”. In: *Reviews in Physics* 4 (2019), p. 100032.

[44] S. Girard et al. “PETRA: an Experimental Platform for X-ray Radiation Testing of Materials and Components”. In: *Proceedings of the 15th Symposium SiO_2, Advanced Dielectrics and Related Devices*. Conference presentation, June 23–26, 2025. Saint-Étienne, France, June 2025.

[45] Japan Atomic Energy Agency (JAEA). *PHITS User’s Manual. Particle and Heavy Ion Transport code System, version 3.35*. Version 3.35. Japan Atomic Energy Agency. Apr. 16, 2024. URL: https://phits.jaea.go.jp/manual/manualE-phits.pdf.

[46] Tatsuhiko Sato et al. “Features of Particle and Heavy Ion Transport code System (PHITS) version 3.02”. In: *Journal of Nuclear Science and Technology* 55.6 (2018), pp. 684–690. DOI: 10.1080/00223131.2017.1419890.

[47] International Commission on Radiation Units and Measurements. *Fundamental Quantities and Units for Ionizing Radiation*. Tech. rep. Report 60. Bethesda, MD: ICRU, 1998.

[48] NIST ESTAR Database. *Stopping Power and Range Tables for Electrons*. https://physics.nist.gov/PhysRefData/Star/Text/ESTAR.html. Accessed May 2025. 2024.

[49] B. Seitz, M. Gerlach, and E. Forster. “Electron range and backscattering in dielectric materials at low energies”. In: *Journal of Applied Physics* 119.23 (2016), p. 235101. DOI: 10.1063/1.4953880.

[50] Diego Di Francesca et al. “Qualification and Calibration of Single Mode Phosphosilicate Optical Fiber for Dosimetry at CERN”. In: *Journal of Lightwave Technology* (2019). Early Access. DOI: 10.1109/JLT.2019.2915510.

[51] M. Cecchetto et al. “Dosimetry in a Mixed Spallation Source with RPLs and FLUKA Simulations”. Submitted for publication to IEEE Transactions on Nuclear Science, Sept. 2025.

[52] M. Avesani et al. “Optical Fibers Irradiation at the $n_TOFNEARStationatCERN$: $aMonteCarloSimulationDosimetryStudy$”. In: *Proceedings of the SiO_2 Conference*. Poster presentation. 2025.

[53] Damien Lambert et al. “Simulation-assisted methodology for the design of fiber-based dosimeters for a variety of radiation environments”. In: *IEEE Transactions on Nuclear Science* 71.8 (2024), pp. 1846–1853.

[54] A Meyer et al. *Simulation and Optimization of Optical Fiber Irradiation with X-rays at Different Energies. Radiation 2023, 3, 58–74*. 2023.

[55] Breccia Letizia et al. "Radiation-Induced Luminescence of a Medium-OH Pure Silica Core Multimode Optical Fiber in Steady-State and Pulsed X-ray Irradiations: Potential and Limitations for Dosimetry". In: *physica status solidi (a)* (2025). under revision.

[56] Selyan Acid et al. "Temperature Impact on a Radioluminescent Silica-based Optical Fiber Dosimeter for Space Applications". In: *IEEE Sensors Journal* (2025).

[57] Cosimo Campanella et al. "Radiation Effects on Pure-Silica Multimode Optical Fibers in the Visible and Near-Infrared Domains: Influence of OH Groups". In: *Applied Sciences* 11.7 (Mar. 2021), p. 2991. DOI: 10.3390/app11072991. URL: https://doi.org/10.3390/app11072991.

[58] A Raj Mandal et al. "Online X-ray radiation induced attenuation of RPL Dosimeters: Dose rate dependence at high doses". In: *IEEE Transactions on Nuclear Science* (2025).

[59] Lorenzo Sostero et al. "Radiation-induced effects on commercial 3D printing materials exposed to high x-ray doses". In: *Journal of Physics: Materials* 8.3 (2025), p. 035003.

[60] Laboratoire Hubert Curien. *PETRA Experimental Platform for Radiative Tests*. Accessed: 27 August 2025. 2025. URL: https://laboratoirehubertcurien.univ-st-etienne.fr/en/platforms/petra-experimental-platform-for-radiative-tests.html (visited on 08/27/2025).

[61] F. Fricano et al. "Reproducibility of Dose Rate Measurements With Radioluminescent Nitrogen-Doped Optical Fibers". In: *IEEE Transactions on Nuclear Science* 70.8 (Aug. 2023), pp. 1925–1932. DOI: 10.1109/TNS.2023.3263381.

[62] Exail. *Exail - High-technology company*. 2025. URL: https://www.exail.com/ (visited on 09/04/2025).

[63] Luca Weninger et al. "Calibration in the visible and infrared domains of multimode phosphosilicate optical fibers for dosimetry applications". In: *IEEE Transactions on Nuclear Science* 70.8 (2023), pp. 1908–1916.

[64] S. Girard et al. "Radiation effects on silica-based optical fibers: Recent advances and future challenges". In: *Journal of Optics* 15.2 (2013), p. 025706. DOI: 10.1088/2040-8978/15/2/025706.

[65] Mahbubur Rahman et al. "FLASH radiotherapy treatment planning and models for electron beams". In: *Radiotherapy and Oncology* 175 (2022), pp. 210–221. DOI: 10.1016/j.radonc.2022.08.009. URL: https://doi.org/10.1016/j.radonc.2022.08.009.

[66] Till Tobias Böhlen et al. "Normal Tissue Sparing by FLASH as a Function of Single-Fraction Dose: A Quantitative Analysis". In: *International Journal of Radiation Oncology, Biology, Physics* (2022). DOI: 10.1016/j.ijrobp.2022.05.038. URL: https://doi.org/10.1016/j.ijrobp.2022.05.038.

[67] Jean Bourhis et al. "Treatment of a first patient with FLASH-radiotherapy". In: *Radiotherapy and Oncology* 139 (2019), pp. 18–22. DOI: 10.1016/j.radonc.2019.06.019. URL: https://doi.org/10.1016/j.radonc.2019.06.019.

[68] Maria Grazia Ronga et al. “Back to the Future: Very High-Energy Electrons (VHEEs) and Their Potential Application in Radiation Therapy”. In: *Cancers* 13.19 (2021), p. 4942. DOI: 10.3390/cancers13194942. URL: https://doi.org/10.3390/cancers13194942.

[69] B. Lin et al. “FLASH Radiotherapy: History and Future”. In: *Frontiers in Oncology* 11 (2021), p. 644400. DOI: 10.3389/fonc.2021.644400. URL: https://doi.org/10.3389/fonc.2021.644400.

[70] M. M. Kim et al. “Development of Ultra-High Dose-Rate (FLASH) Particle Therapy”. In: *IEEE Transactions on Radiation and Plasma Medical Sciences* 6.3 (2022), pp. 252–262. DOI: 10.1109/TRPMS.2021.3091406. URL: https://doi.org/10.1109/TRPMS.2021.3091406.

[71] J. Vidalot et al. “Optical Fiber-Based Monitoring of X-ray Pulse Series from a Linear Accelerator”. In: *Radiation* 2.1 (2021), pp. 17–32. DOI: 10.3390/radiation2010002. URL: https://doi.org/10.3390/radiation2010002.

[72] Adriana Morana et al. “Influence of neutron and gamma-ray irradiations on rad-hard optical fiber”. In: *Optical Materials Express* 5.4 (2015), pp. 898–911.

[73] Adriana Morana et al. “Extreme radiation sensitivity of ultra-low loss pure-silica-core optical fibers at low dose levels and infrared wavelengths”. In: *Sensors* 20.24 (2020), p. 7254.

[74] Martin Roche et al. “Solar particle event detection with the LUMINA optical fiber dosimeter aboard the international space station”. In: *IEEE Transactions on Nuclear Science* 71.8 (2024), pp. 1580–1588.

[75] Luca Weninger. “Potential of radioluminescent silica-based optical fibers for 14 MeV neutron beam monitoring”. In: *Results in Optics* 19 (May 2025). Open access under CC BY 4.0 license. This article is part of the special issue: ‘FOS in ionizing radiation’, p. 100807. ISSN: 2666-9501. DOI: 10.1016/j.rio.2025.100807. URL: https://doi.org/10.1016/j.rio.2025.100807.

Acknowledgements

First and foremost, I would like to express my sincere gratitude to all those who contributed to the realization of this work.

I am sincerely grateful to *Prof. Silvia Bortolussi* and *Prof. Matteo Ferrari* for offering me the wonderful opportunity to complete my thesis internship at the Hubert Curien Laboratory in Saint-Étienne, marking the beginning of what I hope will be a long and fruitful scientific collaboration between this laboratory and the University of Pavia. Furthermore, I thank you and *Dr. Ian Postuma* for the insightful suggestions and valuable advice, essential in this manuscript.

I would also like to express my sincere gratitude and admiration to *Prof. Sylvain Girard*, whose scientific expertise has been essential in shaping this research and in fostering my growth as a young researcher.

I am deeply thankful to all the members of the *MOPERE group and beyond*, Fiammetta, Matilde, Florencia, Adriana, Roberto, Luca, Aditya, Jérémy, Vincenzo, Alberto and Giuseppe, for their kindness, patience, and support. I immediately felt at home when I arrived at the laboratory, thanks to each of you. I truly hope we will have the opportunity to share much more science, and many more moments, together. Thank you, above all, for your friendship.

Thanks to my *fellow travelers* on this journey in Pavia, especially Emilia, Edu, Sara and Sofia. A special mention goes to Sofia who was constantly present throughout the experimental and writing phases of this thesis, even from abroad. Because of you, I always felt listened to and understood.

Finally, a special sense of gratitude to my *family* for the unwavering support and trust, and to all my *friends*, old and new, which managed to be close to me throughout this journey, even from afar.